A THEORETICAL STUDY OF HETEROJUNCTION AND GRADED BAND GAP TYPE SOLAR CELLS

Annual Report on
NASA Grant No.
NSG 1116

April 1977

J. E. Sutherland and J. R. Hauser

North Carolina State University
Electrical Engineering Department
Box 5275, Raleigh, NC 27607

N77-30618

A THEORETICAL STUDY OF HETEROJUNCTION AND GRADED BAND GAP TYPE SOLAR CELLS

Annual Report on
NASA Grant No.
NSG 1116

April 1977

J. E. Sutherland and J. R. Hauser

North Carolina State University
Electrical Engineering Department
Box 5275, Raleigh, NC 27607

ABSTRACT

This report summarizes research done during the past twelve months under NASA Grant NSG-1116, entitled A Theoretical Study of Heterojunction and Graded Band Gap Type Solar Cells. The purpose of this work is to design a computer program for the analysis of variable composition solar cells and apply that program to several proposed solar cell structures using appropriate semiconductor materials. As discussed in this report, the program has been completed and has been used to study devices made of $Al_xGa_{1-x}As$, $Ga_xIn_{1-x}As$ and $GaAs_{1-x}P_x$ with the intention of determining the material compositions and device dimensions that produce high conversion efficiency.

The computer program has been designed to simulate solar cells made of a ternary alloy (such as $Al_xGa_{1-x}As$) of two binary semiconductors with an arbitrary composition profile, and an abrupt or Gaussian doping profile of polarity n-on-p or p-on-n with arbitrary doping levels. An antireflection layer of SiO of any reasonable thickness can be specified and either AM0 or AM2 solar irradiance conditions can be selected. Once the device structure is specified, the program numerically solves a complete set of differential equations and calculates electrostatic potential, quasi-Fermi levels, carrier concentrations and current densities, total current density and efficiency as functions of terminal voltage and position within the cell. These results are then recorded by computer in tabulated or plotted form for interpretation by the user.

The report includes background discussions concerning variable composition solar cell phenomena and the theoretical techniques used to

model device behavior. The results of the computer analysis of various proposed cell structures are then presented. It was found that interface recombination due to lattice mismatch at abrupt AlAs-GaAs heterojunctions produced an insignificant reduction in peak efficiency while recombination at GaP-GaAs heterojunctions produced far more severe losses. However, it was subsequently found that these losses could be largely eliminated by placing the p-n junction slightly below the GaP-GaAs heterojunction (by about 0.04 μM) and by grading the composition change over a small distance (also about 0.04 μM).

According to computer simulation, even a very thin window layer (0.1 μM) of AlAs or GaP should virtually eliminate the surface recombination losses known to limit GaAs homojunction solar cells. In fact, to minimize generation-recombination loss in the window and maximize overall efficiency, the wide bandgap layer should be as thin as technologically feasible (at least down to 0.1 μM). Finally, the problem of optimizing the composition of the substrate in AlAs-on-$Al_xGa_{1-x}As$, AlAs-on-$In_xGa_{1-x}As$ and GaP-on-$GaAs_{1-x}P_x$ structures is explored by simulating cells with various substrate compositions.

These computer studies are intended to provide a more accurate estimate of the potential performance of variable composition solar cells than is possible with simpler, non-computer models. The results of these simulations should serve as a guide for the design of high efficiency experimental solar cells.

TABLE OF CONTENTS

Page

LIST OF TABLES

LIST OF FIGURES

LIST OF FIGURES (continued)

LIST OF FIGURES (continued)

LIST OF FIGURES (continued)

1. INTRODUCTION

1.1 Incentive for Computer Simulation

Recent developments in the world's energy market have underscored the need for development of alternative energy sources to reduce our national dependence on fossil fuels and provide for the inevitable depletion of such limited resources. Although solar energy cannot be expected to satisfy a significant fraction of the world's energy demands for several decades, its unlimited nature will make it progressively more competitive as scarcity forces the cost of existing sources higher.

Given the abundant supply of solar energy and the growing demand for electric power, the ultimate answer to the energy problem would appear to be the solar cell, which directly converts sunlight to electricity. However, the high cost per watt (currently about $15.00) associated with solar cells has limited their use to a few specialized applications [1,60]. Reduction of this price depends on the reduction of cell fabrication costs, and an increase in conversion efficiency, which typically ranges from 12% to 16% depending on cell structure and illumination conditions.

While most solar cells are presently made of a single semiconductor (usually silicon), some of the most efficient cells have been built by allowing the material composition to vary with depth through the device so that various layers can have independently controlled optical and electrical characteristics. Such a cell is diagramed in Figure 1.1, where the cell substrate consists of GaAs, and the surface layer is a linearly graded alloy of $Al_xGa_{1-x}As$. Preliminary calculations predict a conversion efficiency of approximately 17% under air mass zero (AM0)

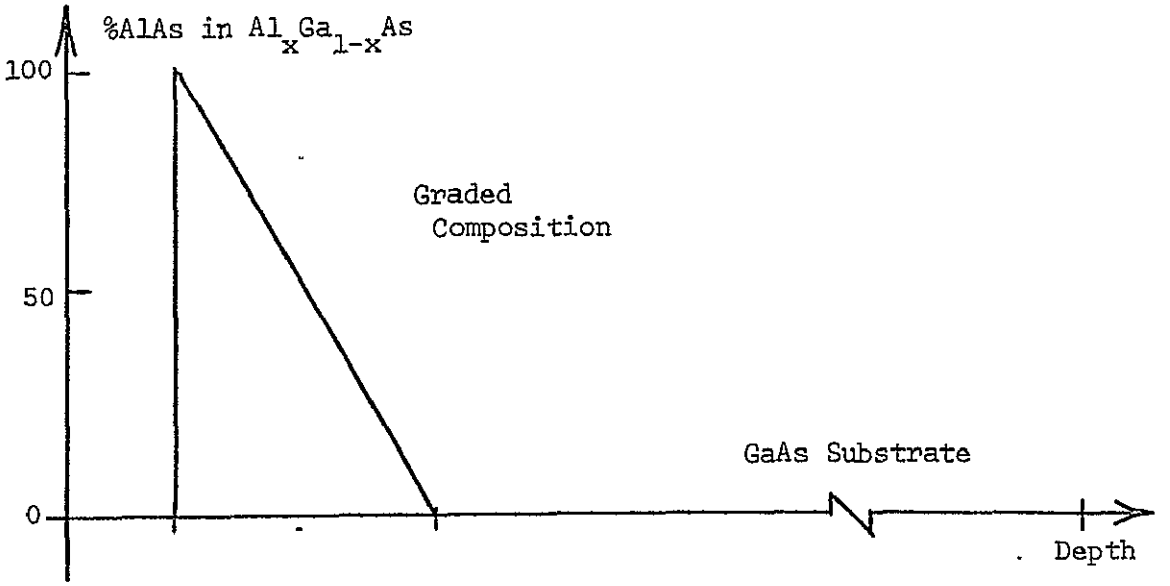

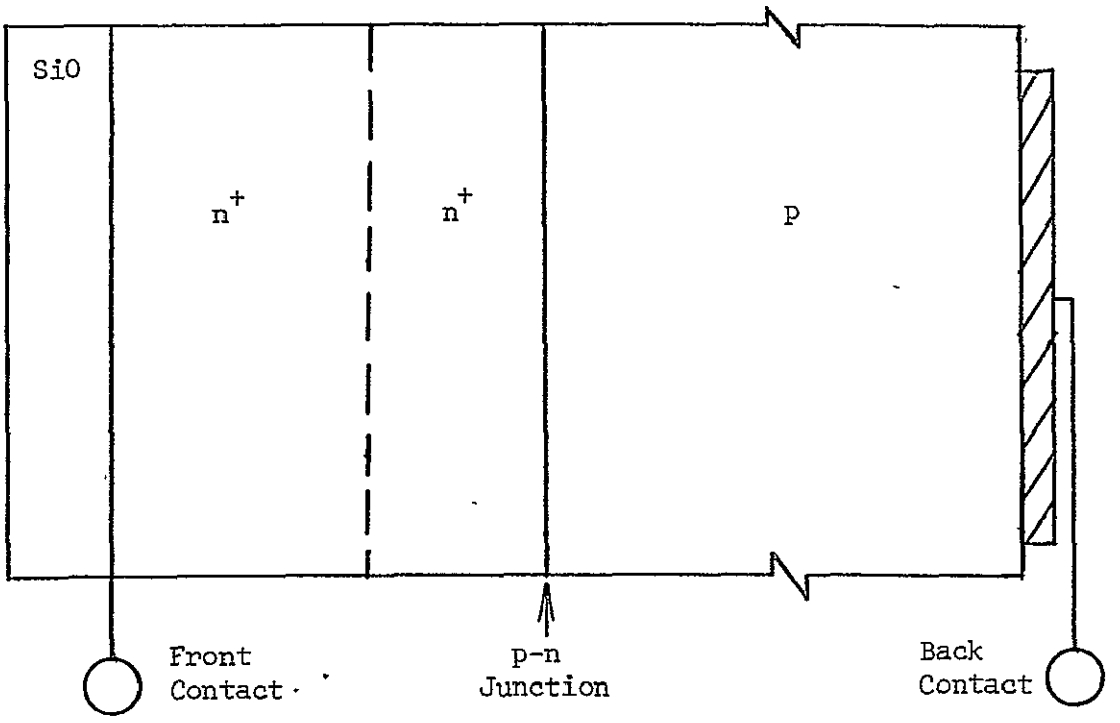

Figure 1.1 General composition profile and structure for a variable composition $Al_xGa_{1-x}As$ solar cell.

conditions for such a device compared with 9% for a good homojunction GaAs cell [49]. Although it is to be expected that variable composition cells will carry higher fabrication costs per unit area, the improvement in efficiency could make them attractive in applications where other costs dominate the complete system price, such as those having concentrator lenses and solar tracking mechanisms. Variable composition $Al_xGa_{1-x}As$ cells potentially have a high conversion efficiency because they can prevent the severe surface recombination losses associated with GaAs homojunction cells while retaining the superior match to the solar spectrum which constitutes the main advantage of GaAs cells over Si cells.

Since the design of variable composition solar cells permits the use of a wide variety of semiconductor alloys and composition profiles, it would be useful to have a computer model that could accurately predict the performance of proposed cell structures before they are actually built. For example, it is not obvious whether material composition should be varied gradually with depth to create a graded layer (as in Figure 1.1) or abruptly to create a heterojunction. Likewise, the determination of the optimum placement of the p-n junction in relation to the other layers is not an easy problem. In an effort to answer these, and other questions, an existing homojunction solar cell computer analysis program has been modified to permit the modeling of variable composition solar cell structures. The computer model serves as an intermediate step between first order approximations of device behavior and the physical construction of a working model. The computer program can include the many detailed second-order phenomena that must

be excluded from first order calculations. In addition, the structure and specifications of a computer model can be manipulated with a flexibility that is impractical during the testing of a physical model. Thus, computer analysis can point out the critical design factors and help determine the most efficient and least expensive structure before it is actually built.

The present work describes the ideas involved in a computer program development and the performance it predicts for various proposed cell structures. Also included is a discussion of the relative importance of various design factors in obtaining maximum efficiency based on computer predictions and the limitations of solid state technology.

1.2 Literature Review

The development of analysis techniques for variable composition solar cells can be traced back to attempts by several workers to explain early silicon homojunction solar cell behavior. In 1955, Prince [20] approximated the J-V characteristic of such cells by shifting the well known Shockley diode curve by the amount of short circuit current that could be collected from optically generated carriers. An estimate of internal resistance losses was also included in the model. In 1956, work by Loferski [21] gave the first indication that silicon did not provide the optimum optical match to the solar spectrum under AM0 conditions. In fact, in the same year, Jenny et al. [57] reported an experimental GaAs solar cell efficiency of 6.5% which was comparable to the values obtained from Si and CdS solar cells at that time. However, due to the dominance of silicon technology in fabricating other

solid state devices, most solar cell experimentation continued to consist of variations on basic silicon structures.

The first theoretical examinations of graded bandgap materials in solar cells came in 1957 when Tauc [3] estimated the photovoltage due to bandgap variation. In 1960, Wolf [4] analyzed the behavior of a graded gap region in combination with a p-n junction, and later, in 1962, Emtage [5] predicted that such a configuration could produce conversion efficiencies as high as 35%. At about the same time, Anderson [55] developed a basic model for heterojunctions which considered current flow by the injection of carriers over band edge barriers; and later, in 1964, the abrupt heterojunction solar cell was theoretically analyzed by Perlman and Feucht [56].

The suggestion by Kroemer in 1963 [9] that the use of heterojunctions (interfaces between dissimilar materials) could improve the performance of injection lasers was followed by escalated laser research using position-dependent ternary III-V alloys for light and carrier confinement. The resulting need for experimental data concerning the material properties and band structures of III-V alloys was satisfied by many workers, notably Cohen and Bergstresser [7] in 1966 and by Thompson and Woolley [8] in 1967. Such data would prove vital to later research on variable composition solar cells.

By the late 1960's, various band diagram models for semiconductor heterojunctions had been proposed and in 1971 Marfaing and Chevallier [10] published a theoretical analysis of photovoltaic effects in variable composition devices that allowed for position dependent bandgap, carrier mobilities, effective masses, lifetimes and doping.

Their theory was accompanied by their experimental studies of $Cd_xHg_{1-x}Te$ graded composition crystals. In 1973, Womac and Rediker [11] explained heterojunction laser behavior by using a model that spread the composition variations over a few hundred angstroms, resulting in improved understanding of carrier behavior in all variable composition devices. At about the same time, Hovel and Woodall [12] achieved a solar cell conversion efficiency of 14.7% under AMO conditions by placing an $Al_xGa_{1-x}As$ window layer over a GaAs substrate. This represented a substantial improvement over the 9.3% efficiency reported in 1972 by Tsaur et al. [22] for GaAs cells without a wide gap window layer and operating under similar conditions.

The computer techniques used in the present research stem from work by several predecessors. In 1970, Graham and Hauser [13] developed a computer analysis program for p-n junction diodes by building on techniques used by earlier workers, notably Bellman and Kalaiba [14,15,16], DeMari [17] and Lee [18]. Four years later, Dunbar and Hauser [19] modified the program so that it could simulate silicon homojunction solar cells. The essential purpose of these computer studies was the analysis of solar cell behavior without resorting to first order approximations such as those necessary for the solution of non-computer models. The present work represents an extension of this idea into the more complex field of variable composition solar cell analysis.

1.3 Computer Analysis Techniques

The computer program used to model solar cell behavior is based on the familiar set of nonlinear differential equations normally applied to p-n junction diodes. These consist of the transport and continuity equations for electrons and holes, along with Poisson's equation. The influence of light on the diode equations appears as an independently calculated optical generation rate, G_e, inserted in the continuity equations. The material parameters, such as mobility, lifetime and bandgap, are provided as functions of composition and/or doping (or position if the composition and doping profiles are given). An attempt has been made to model all parameters as accurately as possible by a combination of theoretical expressions and numerical data. Boundary conditions concerning surface recombination velocity and terminal voltage are then applied to the complete set of equations.

In order to solve this system of nonlinear differential equations, the program uses a technique known as quasi-linearization used previously for diode analysis and later used in homojunction solar cell simulation [13,19]. Briefly, this technique replaces the non-linear equations with linear approximations derived from truncation of the expansion of nonlinear terms. The linear equations are then solved iteratively to converge on the solution to the original nonlinear equations. The results consist of the printout and plotting of electrostatic potential, and current and carrier densities for electrons and holes as functions of position within the solar cell. The most significant results of these analyses are discussed in later chapters of this report.

1.4 Organization of the Report

The following chapters deal with general background discussion, specific computer techniques, and significant analysis results obtained from computer simulations. Chapter 2 begins with an explanation of homojunction solar cell operation and leads into ideas which explain variable composition solar cell behavior. Chapter 3 presents the basic homojunction device equations and develops the modified set of equations used to study variable composition cells. The detailed methods used to incorporate material parameter data into the program are illustrated in Chapter 4 because the assumptions inherent in those methods can be crucial to proper interpretation of the analysis results. Chapter 5 describes the semiconductor materials that were modeled along with the reasons for their selection. In Chapter 6, the most significant of the results obtained from the computer simulation of these structures are presented and interpreted in light of the analysis techniques and the limitations of semiconductor technology. Finally, Chapter 7 summarizes the important ideas associated with this work and recommends areas of future research.

2. PRINCIPLES OF SOLAR CELL OPERATION

2.1 Homojunction Solar Cell Behavior

Figure 2.1 shows a typical n-on-p silicon solar cell having an SiO antireflection layer at the front. Solar photons pass into the n^+ layer with a transmission efficiency enhanced by the SiO layer. As they pass through the silicon crystal, those photons having energy greater than the bandgap of silicon excite electrons across the gap generating excess electron-hole pairs. The built-in field set up by the doping gradient around the p-n junction separates these excess holes and electrons creating a potential across the device terminals that can be used to force a current through an external load. However, since none of these processes is 100% efficient, most of the solar energy striking the cell surface (typically more than 80%) fails to be converted to electrical energy delivered to the external load [19].

First of all, since the solar spectrum contains a range of photon energies (see Figure 2.2), no antireflection layer can insure transmission of all photons into the cell. For the same reason, some photon energies will be smaller than the bandgap, and pass through the cell without generating a significant number of electron-hole pairs. Other photons, having energies greater than the bandgap, will generate carriers but the energy in excess of that necessary to bridge the gap will eventually serve to heat up the crystal. Since these optical losses depend mainly on the semiconductor bandgap, their manipulation is severely limited if the cell consists entirely of a single semiconductor and therefore a constant bandgap. As will be discussed in later sections, the introduction of position-dependent composition

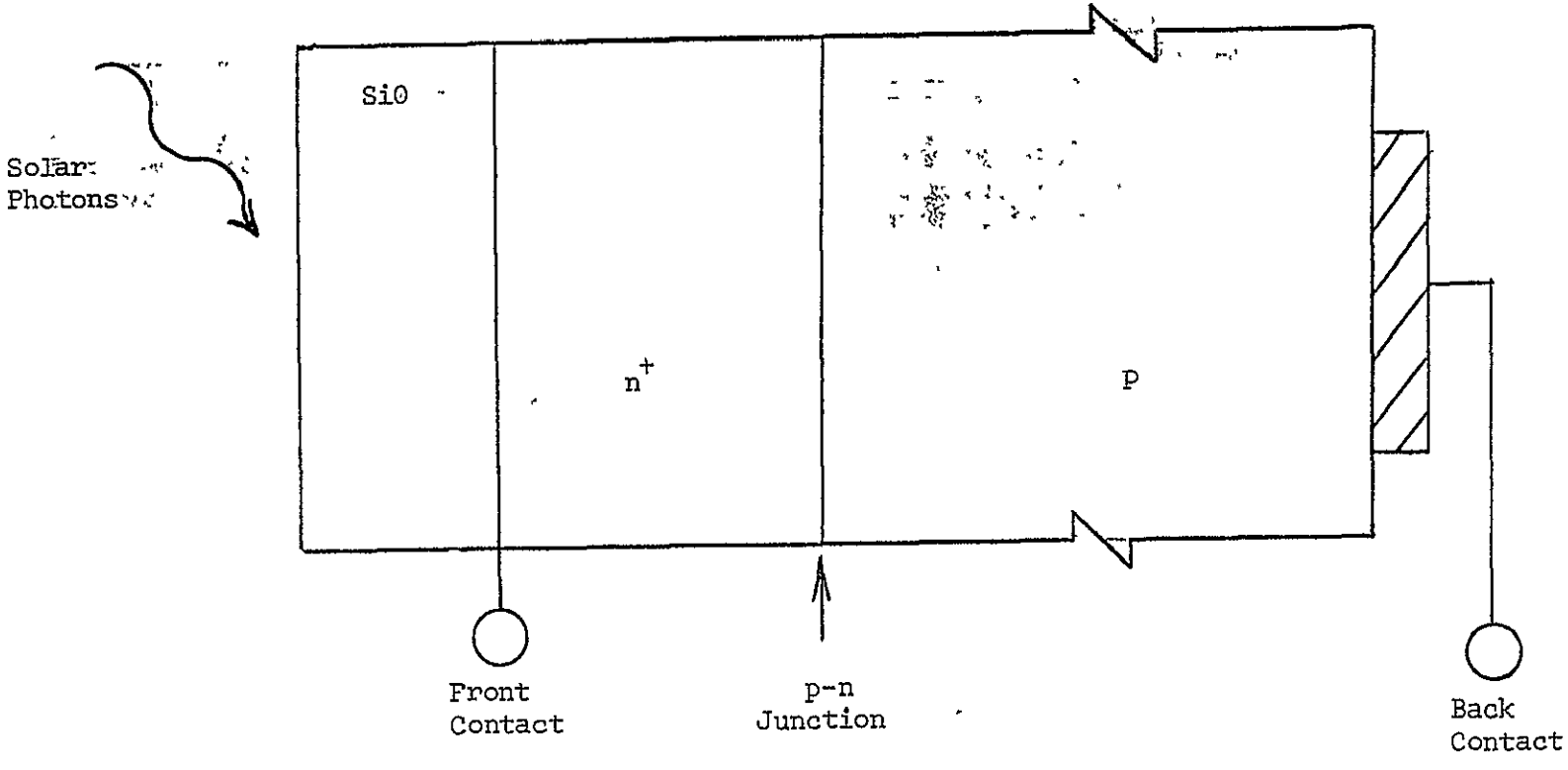

Figure 2.1 Typical n-on-p silicon solar cell.

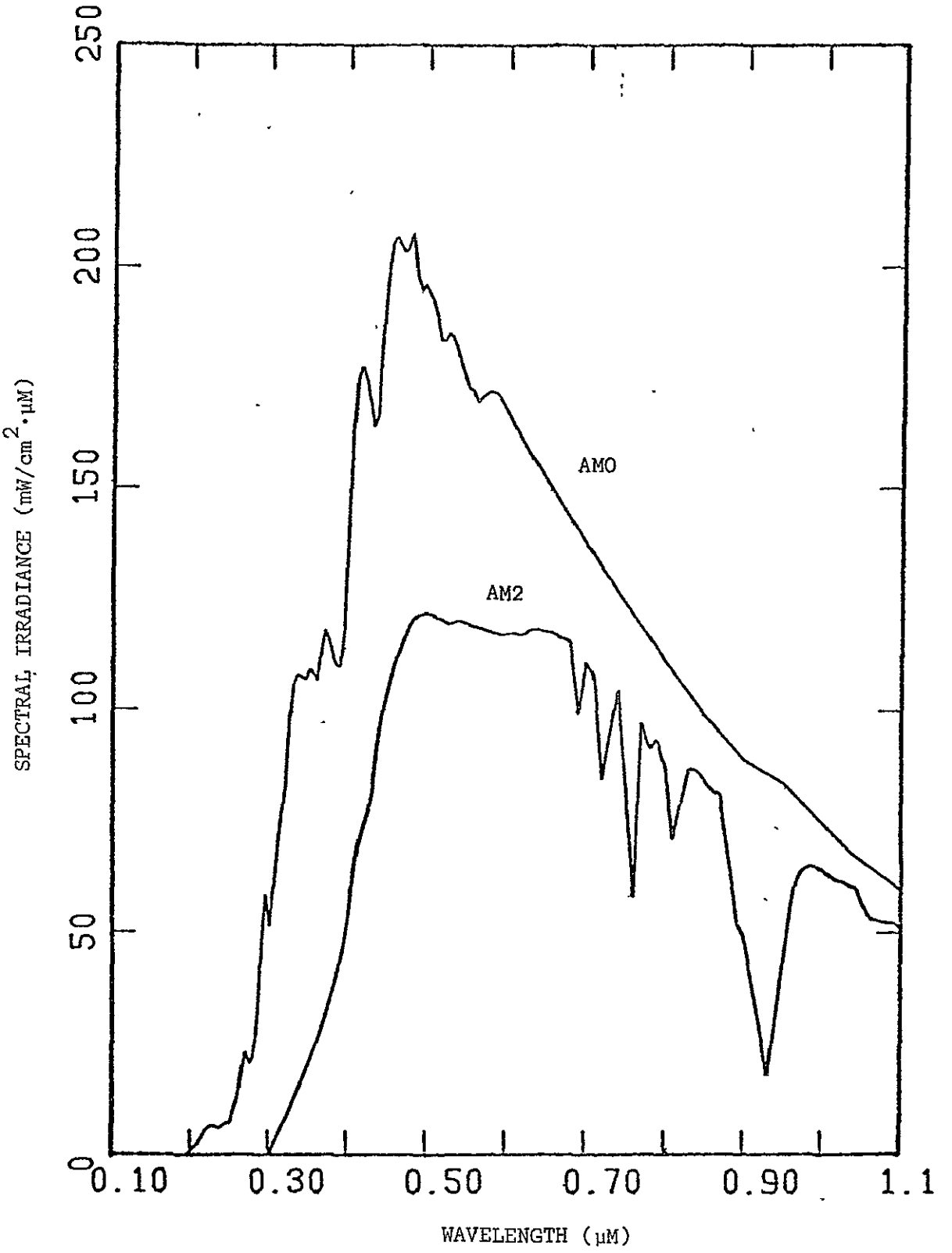

Figure 2.2 Spectral power density for AMO and AM2 conditions [6,50].

provides an additional degree of freedom in minimizing these optical losses which often amount to over 50% of the incident solar energy.

The second set of loss mechanisms is due to a failure to collect all the excess carriers that are generated within the device. The energy captured by generated carriers can be lost as electrons and holes recombine in the junction depletion region, in the bulk, or at imperfections at the front surface. In a homojunction cell, the collection of excess minority carriers is due to the built-in electric field created by the doping gradient around the p-n junction. The efficiency with which the field sweeps these carriers across the junction depends on the distance between the junction and their point of generation and upon their diffusion length, which is in general a function of position.

From the well known transport equations for carrier behavior in diodes, the built-in field in the quasi-neutral regions (away from the p-n junction depletion region) at equilibrium is approximately:

$$E = -\frac{kT}{q}\frac{d(\ell n\, N_D)}{dx} \qquad (n^+ \text{ material, } N_D >> n_i)$$

$$E = \frac{kT}{q}\frac{d(\ell n\, N_A)}{dx} \qquad (p^+ \text{ material, } N_A >> n_i)$$

Thus, doping gradients in the bulk can be used to help sweep minority carriers to the p-n junction depletion region where the built-in field is even greater. Although it would be desirable to have the region of maximum optical generation rate in or near the region of maximum field (around the p-n junction), the achievement of such a situation in a homojunction cell requires a very thin surface layer. But, a thin

surface layer not only presents a high series sheet resistance, but also places the front surface (with its short carrier lifetime) near the junction region as well. In fact, as long as a single material is used throughout the cell, it is impossible to separate the region of maximum generation rate from the region of maximum recombination simply because the generation rate of a homojunction cell (see Figure 2.3) decreases monotonically with depth beneath the front surface. As will be shown later, the introduction of position-dependent composition allows the placement of peak generation well below the front surface.

The final group of loss mechanisms results from the electrical behavior of carriers after they are collected. First of all, as minority carriers cross the p-n junction they become majority carriers and unless short circuit conditions exist, they reduce the built-in junction potential and forward bias the diode. The resulting forward current constitutes a loss that is determined by the dark J-V characteristics of the cell. Such an effect can be modeled to first order by the circuit shown in Figure 2.4a where the diode element characterizes solar cell behavior in the dark, and the current density source equals the short circuit current delivered by the cell under specified illumination conditions. This relationship can be written as

$$J_d = J_{sc} - J_s \left[\exp(qV_T/mkT)-1\right] \tag{2.1}$$

The open circuit voltage, V_{oc}, occurs where the current generated by solar illumination exactly offsets the current lost as forward bias current in the diode.

$$V_{oc} = \frac{mkT}{q} \ell n\left(\frac{J_{sc}}{J_s}\right) \tag{2.2}$$

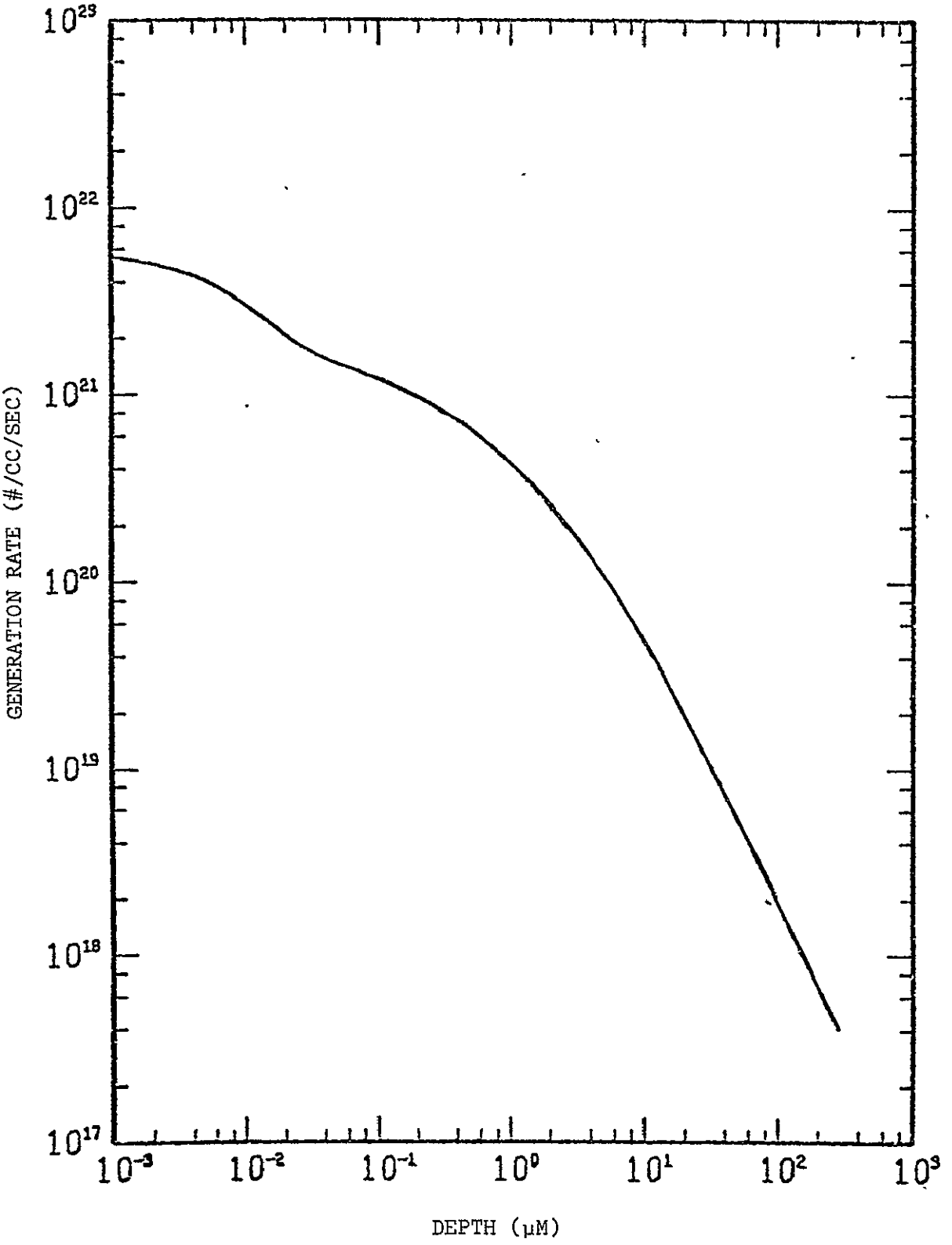

Figure 2.3 Generation rate vs. depth for a silicon homojunction solar cell under AMO conditions with an 0.08 μM anti-reflection layer.

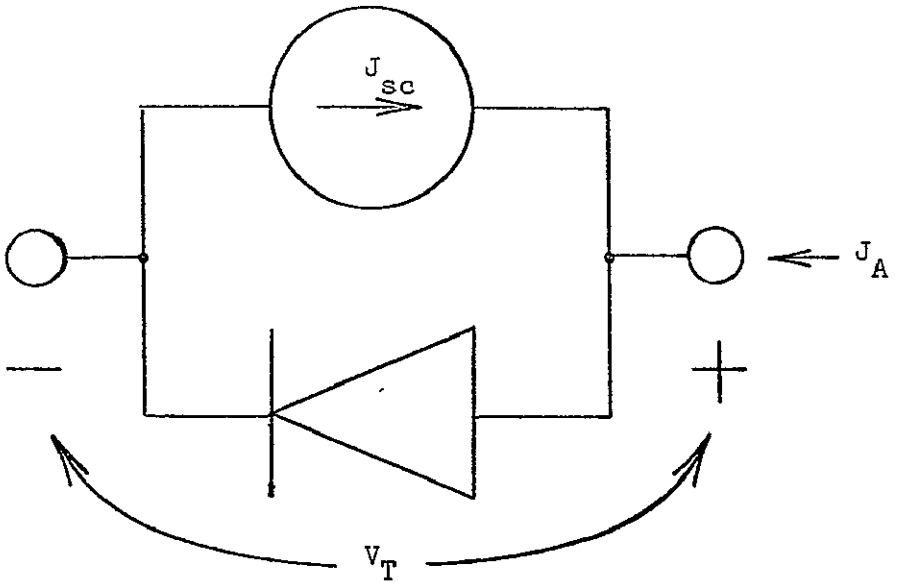

a)

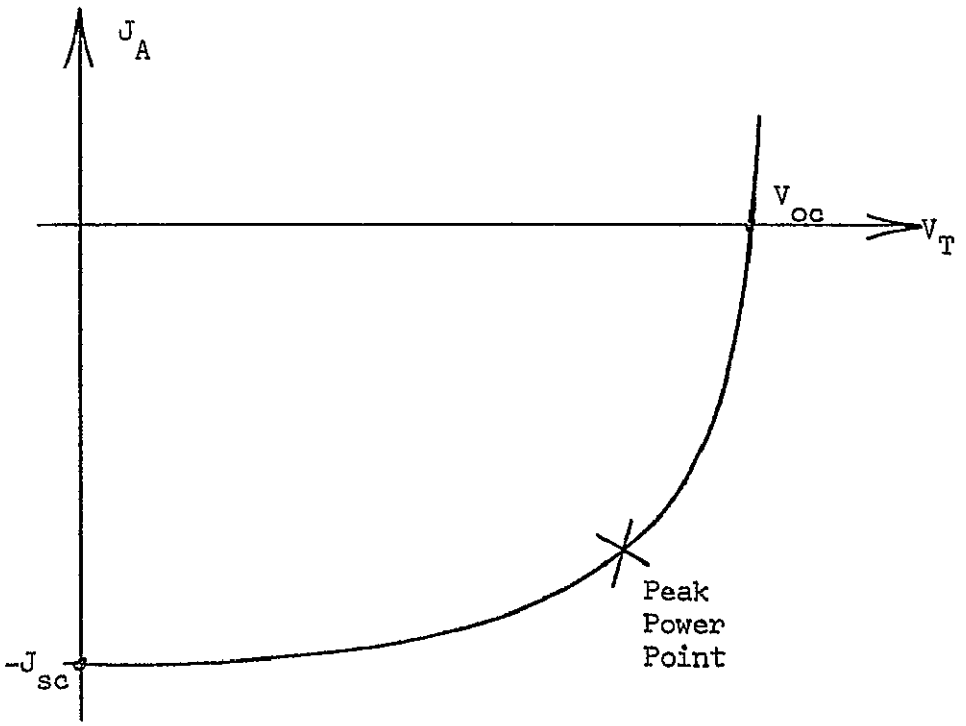

b)

Figure 2.4 a) First order equivalent circuit model and b) corresponding J-V characteristics for a solar cell.

Because of the nonlinear diode characteristics, the maximum power obtainable from any solar cell is determined not only by the short circuit current and open circuit voltage, but also by the sharpness of the "knee" of the J-V curve as measured by the curve factor:

$$C_f = \frac{P_{peak}}{I_{sc} V_{oc}} \tag{2.3}$$

The curve factor is a complex function of the dark characteristics of the solar cell diode.

This simple model leads to an expression for maximum power density (excluding series resistance losses)

$$P_{peak} = (J_{sc} C_f) \left(\frac{mkT}{q} \ell n \frac{J_{sc}}{J_s}\right) \tag{2.4}$$

If the reverse saturation current density, J_s, is due predominantly to diffusion in the p-type base (an n^+-on-p structure will be assumed for discussion purposes) then the factor, m, in the diode equation approaches 1, and J_s can be approximated as

$$J_s = \frac{q\sqrt{D_n}\, n_i^2}{\sqrt{\tau}\, N_p} \tag{2.5}$$

where D_n is the electron diffusion coefficient, n_i is intrinsic carrier density, τ is excess carrier lifetime in the base, and N_p is the doping density in the base. If J_s is controlled mainly by depletion region recombination, then m approaches 2 and J_s can be expressed approximately by

$$J_s = \frac{q\, W_d n_i}{\tau_{po} + \tau_{no}} \tag{2.6}$$

where W_d is the width of the depletion region.

A particular solar cell may have characteristics that lie somewhere between these two situations but in any case it is apparent that the task of maximizing peak power output is full of tradeoffs. For example, from Equation (2.4), it appears that in order to maximize peak power density, J_s should be minimized, possibly by minimizing n_i and D_n (if Equation (2.5) applies). But, this would reduce J_{sc} since a smaller D_n means a lower carrier collection efficiency, and a smaller n_i would generally be achieved by choosing a material with a larger bandgap, in turn making the crystal transparent to a larger share of the solar spectrum. Similarly, although Equation (2.4) apparently indicates that P_{peak} is directly proportional to m, C_f decreases with increasing m, so that the overall influence of m on peak power is not obvious from Equation (2.4). In short, the influence of several design factors on solar cell performance cannot be easily predicted. By computer simulation using accurate modeling techniques and reliable data, the dominant factors controlling solar cell behavior can be clarified.

A final loss factor is associated with the layout of contacts on the front surface. As can be seen from Figure 2.5, their design involves a compromise between minimizing series sheet resistance loss due to lateral current flow, and maximizing the surface exposure to light. The computer program does not account for these resistive and optical losses because they can be reasonably estimated for any cell once a contact geometry is specified, and because the aim of this research is to determine the relative influence of various material parameters that control the internal operation of the cell. It should be noted, however, that internal bulk resistance loss is accounted for inherently in the

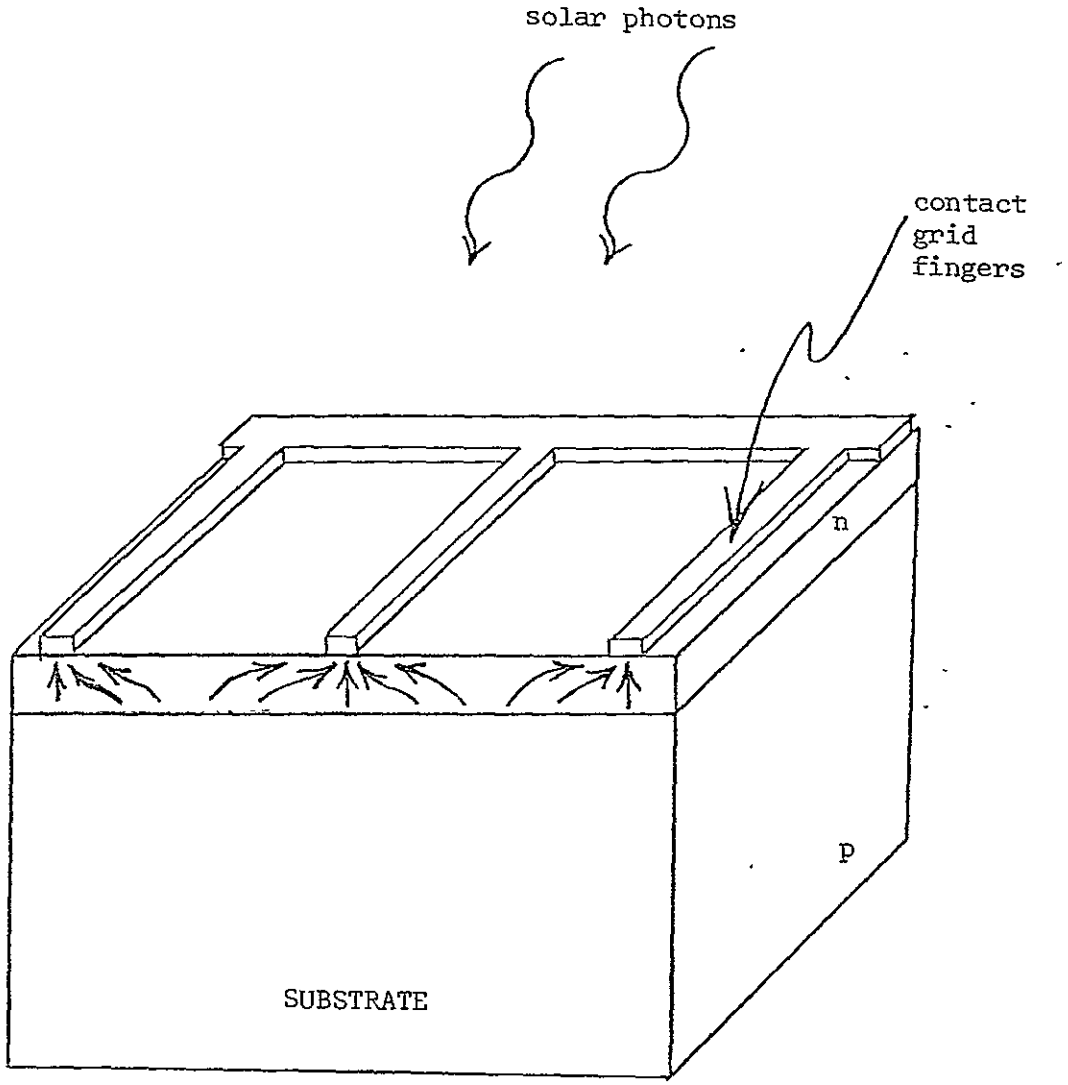

Figure 2.5 Lateral current flow produced by typical finger contact grid.

Table 2.1 Summary of solar cell loss mechanisms.

Optical Losses

1. Surface reflection

   a) From metal coverage
   b) From exposed semiconductor

2. Photon energy in excess of bandgap (i.e. in excess of that necessary to generate electron-hole pairs)

3. Failure to absorb all photons because:

   a) Photon energy less than the bandgap
   b) Cell too thin to absorb essentially all photons of some wavelengths

Collection Losses

1. Surface recombination (front and back)

2. Bulk recombination

Electrical losses:

1. Internal diode bias current

2. Leakage current at imperfect cell edges

3. Series resistance voltage drops due to:

   a) Bulk resistance
   b) Contact resistance seen by lateral current flow to contact fingers

program by the device equations discussed in Chapter 3. Table 2.1 summarizes the important loss mechanisms that dominate solar cell behavior.

2.2 Variable Composition Solar Cell Concepts

2.2.1 Introduction

The phenomena that are responsible for variable composition solar cell behavior are essentially the same as those found in homojunction solar cells. The major distinctions between the two stem mainly from the wide variety of variable composition structures which are available and from the increased complexity of the relationships between energy conversion and loss processes that control performance. However, this complexity brings with it an additional degree of freedom in controlling losses and maximizing conversion efficiency.

For discussion purposes, cells made of AlAs alloyed with GaAs in varying proportions will be examined in this section. As shown in Figure 2.6 the alloy proportions can vary gradually to form a graded layer, can be changed abruptly to form a heterojunction or any number of other variations. The composition at the front surface, and in the bulk can be arbitrarily specified, and the p-n junction may or may not be placed within a graded region.

The relative merits of these, and other options will be discussed conceptually in the following sections and the computer simulation results to be presented in later chapters provide a basis for evaluation of these concepts.

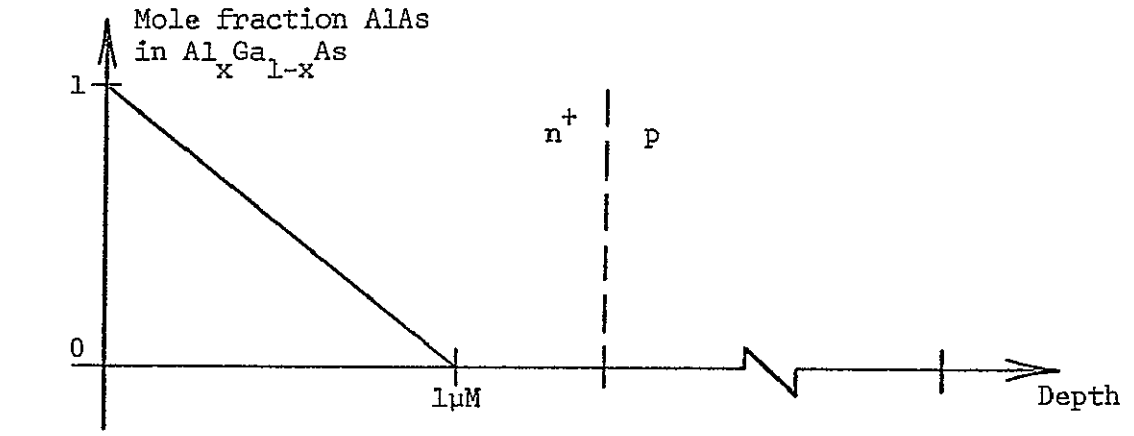

a)

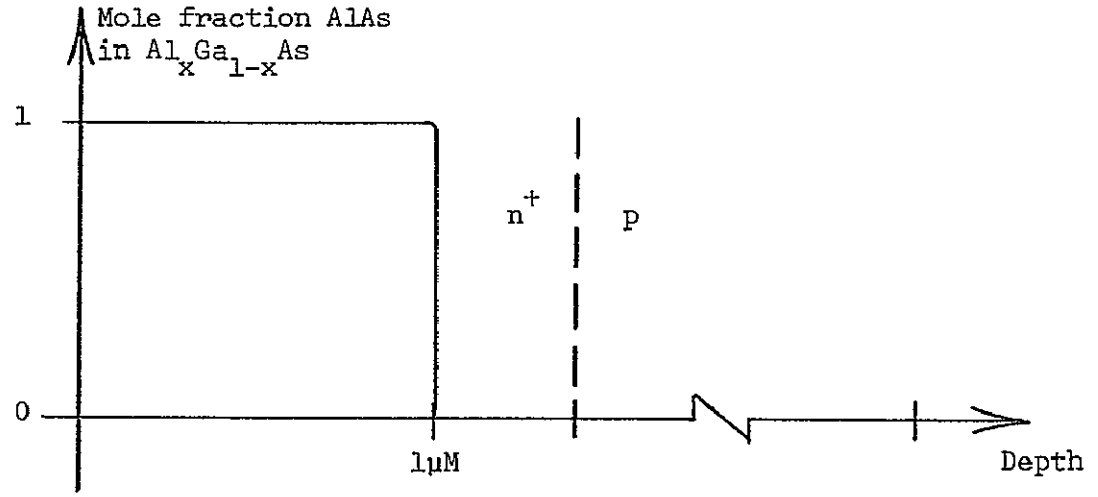

b)

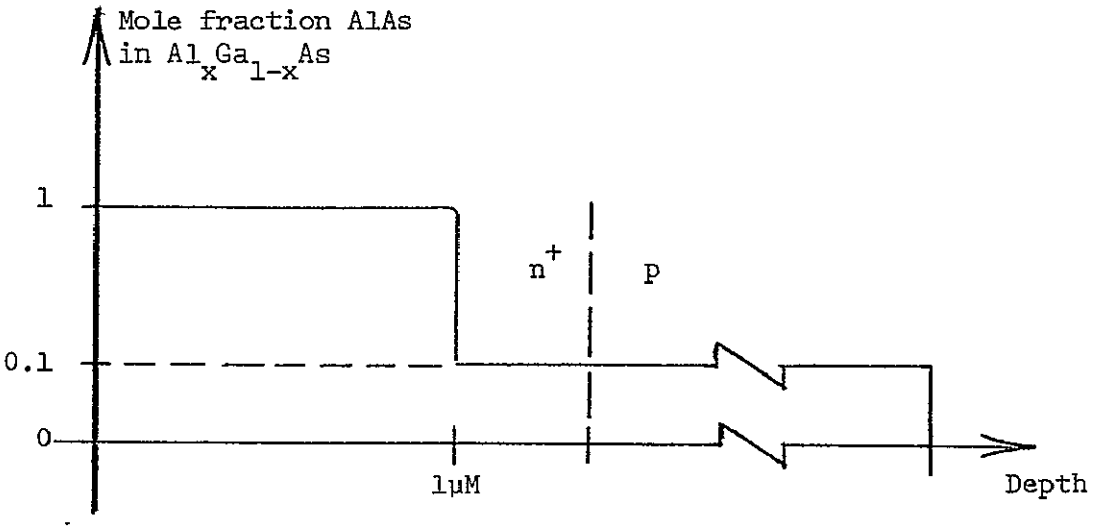

c)

Figure 2.6 Possible composition profiles for $Al_xGa_{1-x}As$ solar cells.

2.2.2 Generation Rate

The most outstanding impact of position dependent composition is on the optical generation rate profile. The profiles of a homojunction GaAs cell, a linearly graded $Al_xGa_{1-x}As$ cell (see Figure 2.6a), and an AlAs-GaAs heterojunction cell (see Figure 2.6b) are shown in Figures 2.7, 2.8 and 2.9 respectively. The calculations used to determine these curves are explained in Chapter 4.

The profile of a homojunction cell consists of the sum of the individual generation rates due to absorption at each wavelength in the solar spectrum. Since the absorption coefficient for a given wavelength is constant if material composition is constant, the generation rate for each wavelength decays exponentially, and the total generation rate is a monotonically decreasing function of depth. In other words, the peak carrier generation for a homojunction cell occurs at the front surface.

However, the carrier generation distribution for a variable composition cell has a more controllable shape determined by the composition profile and the wavelength content of the solar spectrum. As can be seen from Figure 2.8, grading from a semiconductor with a large bandgap to one with a smaller gap can lead to a generation rate peak well below the surface of the cell. As the composition is varied so as to reduce the bandgap, a larger share of the incident photons have sufficient energy to generate carriers. Figure 2.9 shows the extreme case of an abrupt change from a wide bandgap material (AlAs) to a much smaller one (GaAs). The AlAs is relatively transparent to most of the solar photons, while a large percentage of these photons are absorbed by the GaAs layer beneath. This "window effect" is a major advantage of variable

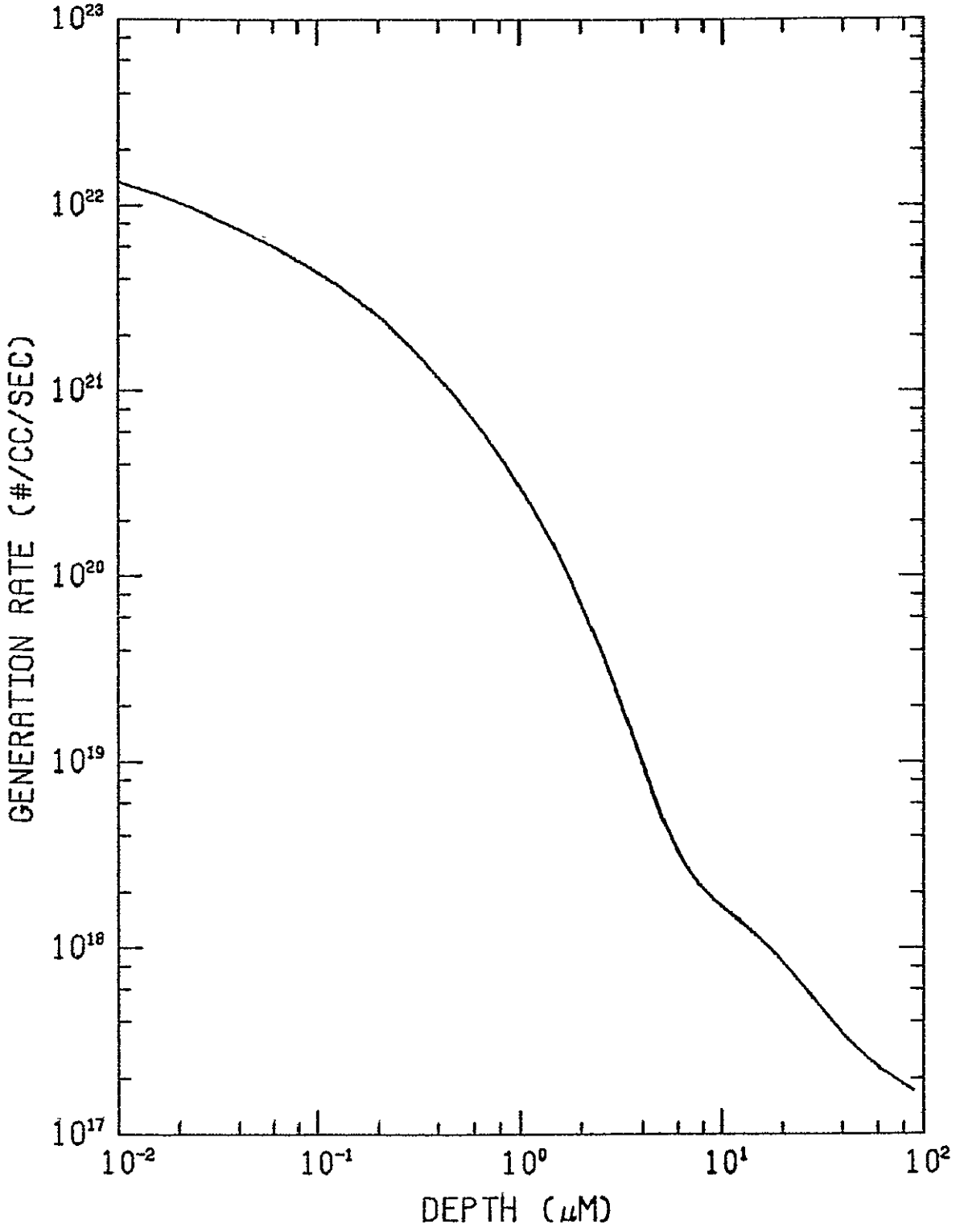

Figure 2.7 Generation rate vs. depth for a GaAs homojunction solar cell under AM0 illumination with an 0.07 μM SiO anti-reflection layer.

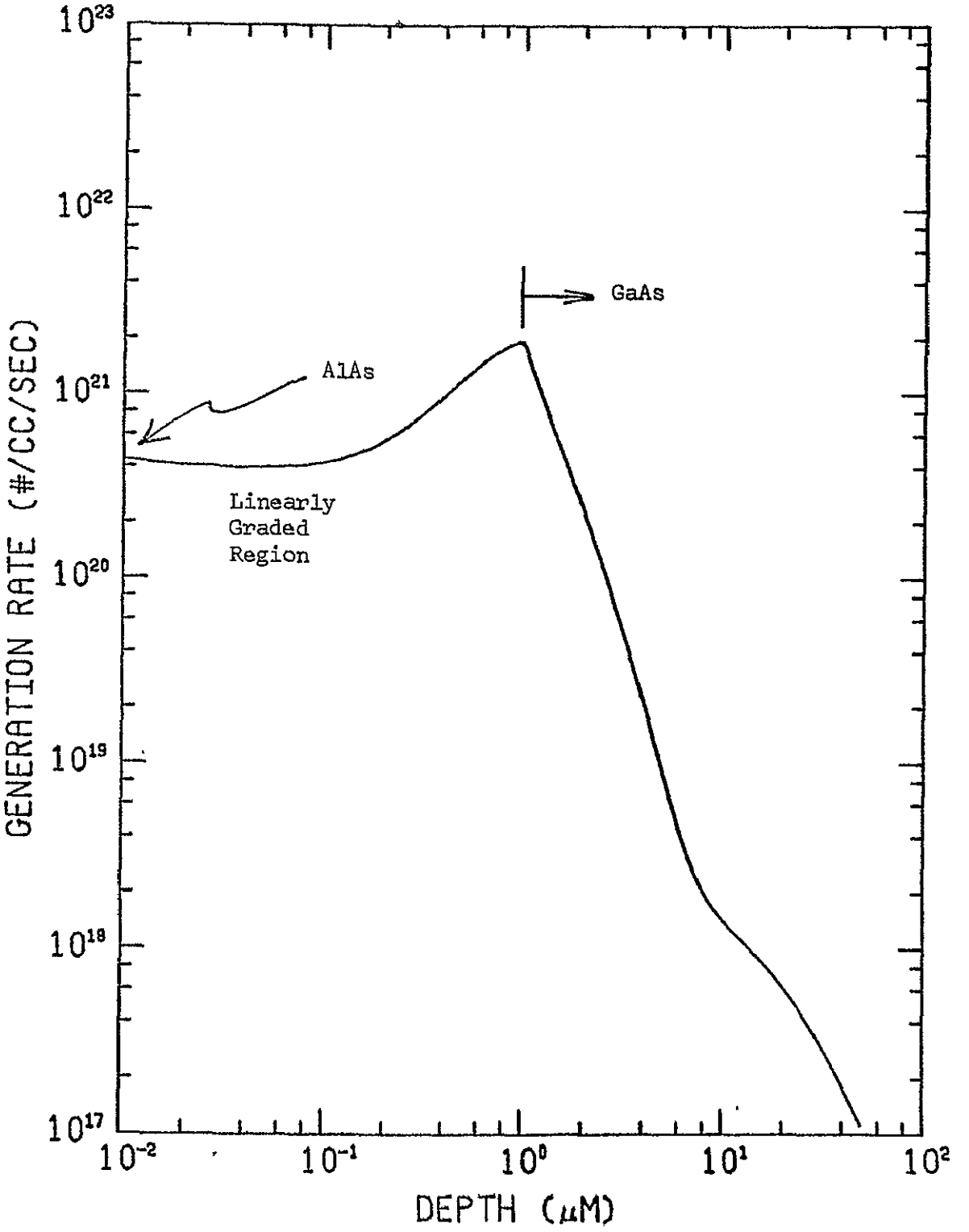

Figure 2.8 Generation rate vs. depth below surface for a graded $Al_xGa_{1-x}As$ solar cell (Figure 2.6à) under AMO illumination with an 0.07μM antireflection layer.

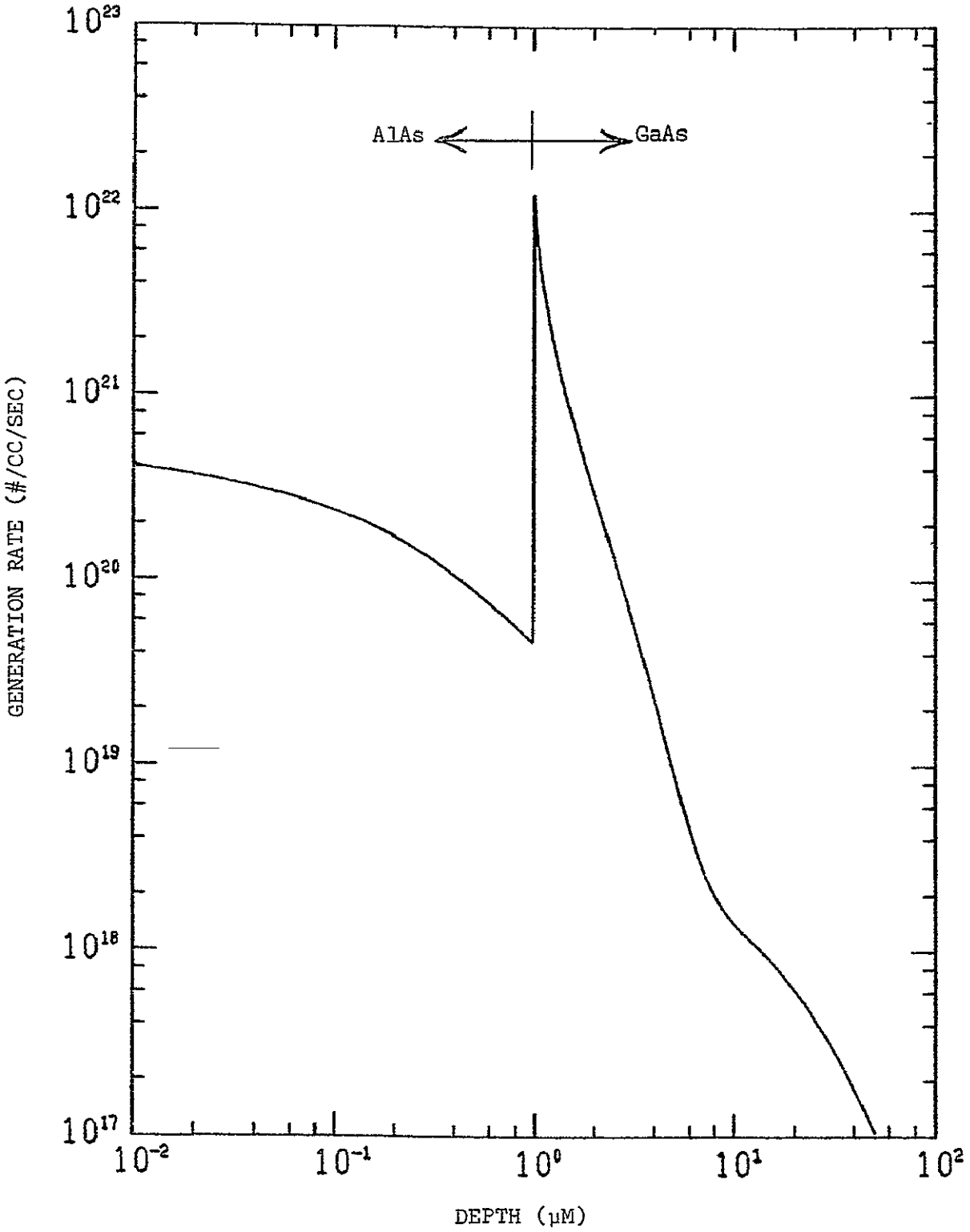

Figure 2.9 Generation rate vs. depth below surface for an AlAs-GaAs heterojunction solar cell (Figure 2.6b) under AM0 illumination with an 0.07μM antireflection layer.

composition solar cells because it separates the region of maximum carrier generation from the top layer of high surface recombination velocity associated with surface imperfections. In addition, the transparency of the window means that the surface layer can be relatively thick and thereby reduce series resistance losses that plague GaAs solar cells [58]. Of course, such a configuration also introduces interface states that reduce lifetime at the heterojunction so that a poor lattice match between materials can nullify the gain in collection efficiency that would otherwise be brought about by the window effect. The problem of interface states is discussed further in the next section.

2.2.3 Interface Recombination

Although it is to be expected that carrier loss by surface recombination can be effectively controlled by use of a wide bandgap window layer, it is by no means certain that interface states due to dangling bonds at the heterojunction will not prevent an overall improvement in collection efficiency. Energy conversion efficiency is especially sensitive to interface state density when the heterojunction is placed within the p-n junction depletion region because recombination there can significantly increase the diode dark current. If depletion region recombination is large enough so that electron and hole currents cannot be assumed constant across the depletion layer, then the current density may be more nearly proportional to $\exp(qV/2kT)$ than to $\exp(qV/kT)$ given by the ideal diode law. In other words, interface states within the depletion region can soften the "knee" of the J-V

characteristics and thus reduce peak output power by reducing the curve factor as well as the open circuit voltage.

However, there are several design options available to control losses due to interface recombination. The most obvious is the selection of a pair of semiconductor materials with a close lattice match. For example, an AlAs-GaAs heterojunction, with a lattice mismatch of about 0.14%, would appear to be a likely candidate for minimizing interface states. An interface between GaP and GaAs, on the other hand, gives a lattice mismatch of about 4%, and could be expected to suffer far more from interface recombination losses.

A second method of minimizing the effects of interface recombination is to place the heterojunction away from the center of the p-n junction depletion region. This prevents the drastic increase in dark current previously mentioned, and also removes the recombination sites from the area of maximum minority carrier collection due to the built-in field within the depletion region. Of course, some loss will still occur as carriers recombine at the dangling bonds even when they are placed in the quasi-neutral region of the device. In order to further reduce the effect of recombination at lattice mismatch sites, the change from the wide bandgap material to the smaller bandgap material can be spread over a finite distance until the effective lifetime in the bulk is not significantly less than the bulk lifetime without interface states.

The detailed reasoning behind these ideas concerning interface recombination is discussed further in Chapter 4 which deals with the computer modeling of several device phenomena. In addition, Chapter 6

discusses the results of several computer simulation runs made expressly to evaluate the effect of interface states on various material arrangements.

2.2.4 Optimization of the Bandgap in the Substrate

It was mentioned in Section 2.1 that no single material can have a bandgap such that all solar photons have sufficient energy to excite carriers without wasting any excess energy as heat. Aside from the secondary generation of pairs by some highly excited carriers, any energy relinquished by absorbed photons exceeding that necessary to bridge the bandgap, eventually serves only to heat up the lattice. On the other hand, virtually all those photons with energy less than the gap are lost as they pass through the crystal without being absorbed in significant numbers.

Research by others indicates that the optimum compromise between these two loss mechanisms calls for a material with a bandgap of about 1.4eV [4,21,23,54]. Although GaAs has a bandgap of approximately this value, it cannot be expected that a single semiconductor will happen to have the optimum gap as well as the most desirable electrical characteristics. It would be more reasonable to examine an alloy between two semiconductors with the proportions selected so as to give optimum overall conversion efficiency. The results of computer simulation runs to determine the optimum composition beneath the window are presented in Chapter 6.

Another option to improve absorption efficiency is also available to the device designer. If composition is graded so that light passes through layers of progressively smaller bandgap, photons of

progressively lower energy can be picked off with less energy waste than would be possible with any fixed bandgap. However, given the complex profile of the solar spectrum, and the fact that the bandgap cannot be controlled independently of other material parameters, it is clear that the determination of the composition profile for maximum conversion efficiency is not a simple problem. In such a situation, the computer simulation data, to be discussed in Chapters 5 and 6, can be very useful.

2.2.5 Built-in Fields due to Composition Grading

As mentioned in Section 2.1, homogenous solar cells depend on doping gradients for the creation of built-in electric fields that collect the carriers generated by optical absorption. However, when material composition varies with position, new built-in electric fields are established that can be used to improve carrier collection efficiency.

The effective built-in field that operates on electrons is proportional to the slope of the conduction band edge as

$$E_{no} = -\frac{1}{q}\frac{d(E_F-E_c)}{dx} \tag{2.7}$$

Similarly for holes, the effective field depends on the slope of the valence band edge as

$$E_{po} = -\frac{1}{q}\frac{d(E_F-E_v)}{dx} \tag{2.8}$$

since

$$E_c = E_v + E_g \tag{2.9}$$

It is clear that different effective fields can be made to operate on electrons and holes only if the bandgap E_g is a function of position. The difference in the two fields is

$$E_{no} - E_{po} = \frac{1}{q}\frac{dE_g}{dx} \tag{2.10}$$

Therefore, by varying the bandgap with position, a built-in field can be established to help sweep excess minority carriers to the p-n junction and thus improve collection efficiency. This option is another advantage gained by allowing material composition to vary with position.

3. DEVICE EQUATIONS FOR COMPUTER ANALYSIS

3.1 Introduction

In order to adequately analyze variable composition solar cells, several device phenomena must be incorporated into the mathematical equations used to model the cells. Among the effects important in ordinary homojunction solar cells are:

1. Drift and diffusion currents
2. Position dependent doping
3. Doping dependent mobility
4. Optical carrier generation
5. Bulk generation-recombination effects
6. Surface recombination effects

The introduction of spatially varying composition demands that additional factors be accounted for:

1. Position dependent bandgap
2. Position dependent electron affinity
3. Built-in fields due to a varying bandgap
4. Composition dependent refractive index at the surface
5. Heterojunction interface recombination
6. Other position dependent material parameters such as:
   a. mobility
   b. dielectric constant
   c. optical absorption coefficient

The computer program used to simulate solar cell behavior is the result of work by several individuals over a number of years. In its original form it was used to analyze p-n junction diodes with no

provision for optical carrier generation [13]. In 1974 it was modified by introduction of a separately computed optical generation rate so that homogeneous solar cells could be studied [19]. In 1975, as part of the present work, the program was again modified to allow for position dependent composition. In the following sections, the equations used in the homogeneous solar cell program will be presented, followed by a development of the corresponding equations used to model variable composition solar cell behavior.

3.2 Equations for Homogeneous Solar Cells

The one-dimensional device equations used to describe homojunction solar cell operation are

Transport:

$$J_n = q\mu_n nE + q D_n \frac{\partial n}{\partial x}, \tag{3.1}$$

$$J_p = q\mu_p pE - q D_p \frac{\partial p}{\partial x} \tag{3.2}$$

Continuity:

$$\frac{\partial n}{\partial t} = - U + \frac{1}{q} \frac{\partial J_n}{\partial x} + G_e, \tag{3.3}$$

$$\frac{\partial p}{\partial t} = - U - \frac{1}{q} \frac{\partial J_p}{\partial x} + G_e, \tag{3.4}$$

Poisson's equation:

$$\frac{\partial E}{\partial x} = \frac{q}{\varepsilon} (p-n+N), \tag{3.5}$$

Auxilliary equations:

$$U = \frac{np-n_i^2}{\tau_{no}(p+p_1)+\tau_{po}(n+n_1)}, \tag{3.6}$$

(Shockley-Read-Hall model with single trapping level)

$$n = N_c \exp\left[\frac{E_{Fn} - E_c}{kT}\right] \text{ (non-degenerate)}, \tag{3.7}$$

$$p = N_v \exp\left[\frac{E_v - E_{Fp}}{kT}\right] \text{ (non-degenerate)}, \tag{3.8}$$

$$N = N_D^+ - N_A^- \text{ (net doping)} \tag{3.9}$$

This system of equations is valid only for a device made of a single semiconductor material doped with enough impurities to create the desired doping profile. The electron energy band structure and its associated characteristics must be the same throughout the device.

As shown by Graham and Dunbar [13,19], the preceding group of equations can be reduced to three equations in the three unknowns ψ, ϕ_n, and ϕ_p, where ψ is the electrostatic potential and ϕ_n and ϕ_p are the Fermi potentials defined by

$$\phi_n = -\frac{1}{q} E_{Fn}, \tag{3.10}$$

$$\phi_p = -\frac{1}{q} E_{Fp}. \tag{3.11}$$

It can be shown that the same basic approach using the same three variables, can be used to analyze variable composition solar cells. The modifications required to account for material variations are discussed in the next section.

3.3 Modification of Equations to Allow for Variable Composition

In order to rewrite the device equations so that they apply to variable composition devices, it is useful to recall the basic principles

from which they were derived. In particular, Equations (3.1) and (3.2) can be written in the more general form

$$J_n = \mu_n n \frac{dE_{Fn}}{dx}. \tag{3.12}$$

$$J_p = \mu_p p \frac{dE_{Fp}}{dx} \tag{3.13}$$

Transport equations involving the field and carrier concentration gradients proceed from the above equations as follows. Referring to Figure 3.1 the conduction band edge energy can be written in general as

$$E_c = q(\psi_o - \psi) - \chi_c, \tag{3.14}$$

where χ_c is the electron affinity, ψ is the electrostatic potential and ψ_o is some reference potential. In a similar manner

$$E_v = q(\psi_o - \psi) - \chi_c - E_g \tag{3.15}$$

From Equations (3.7) and (3.8),

$$E_{Fn} = E_c + kT \ln \left(\frac{n}{N_c}\right), \tag{3.16}$$

$$E_{Fp} = E_v - kT \ln \left(\frac{p}{N_v}\right). \tag{3.17}$$

Then using Equations (3.14) and (3.16), Equation (3.12) can be rewritten as

$$J_n = \mu_n n \left[qE - \frac{d\chi_c}{dx} + \frac{kT}{n}\frac{dn}{dx} - \frac{kT}{N_c}\frac{dN_c}{dx}\right]. \tag{3.18}$$

In a similar manner the hole density equation becomes

$$J_p = \mu_p p \left[qE - \frac{d\chi_c}{dx} - \frac{dE_g}{dx} - \frac{kT}{p}\frac{dp}{dx} + \frac{kT}{N_v}\frac{dN_v}{dx}\right] \tag{3.19}$$

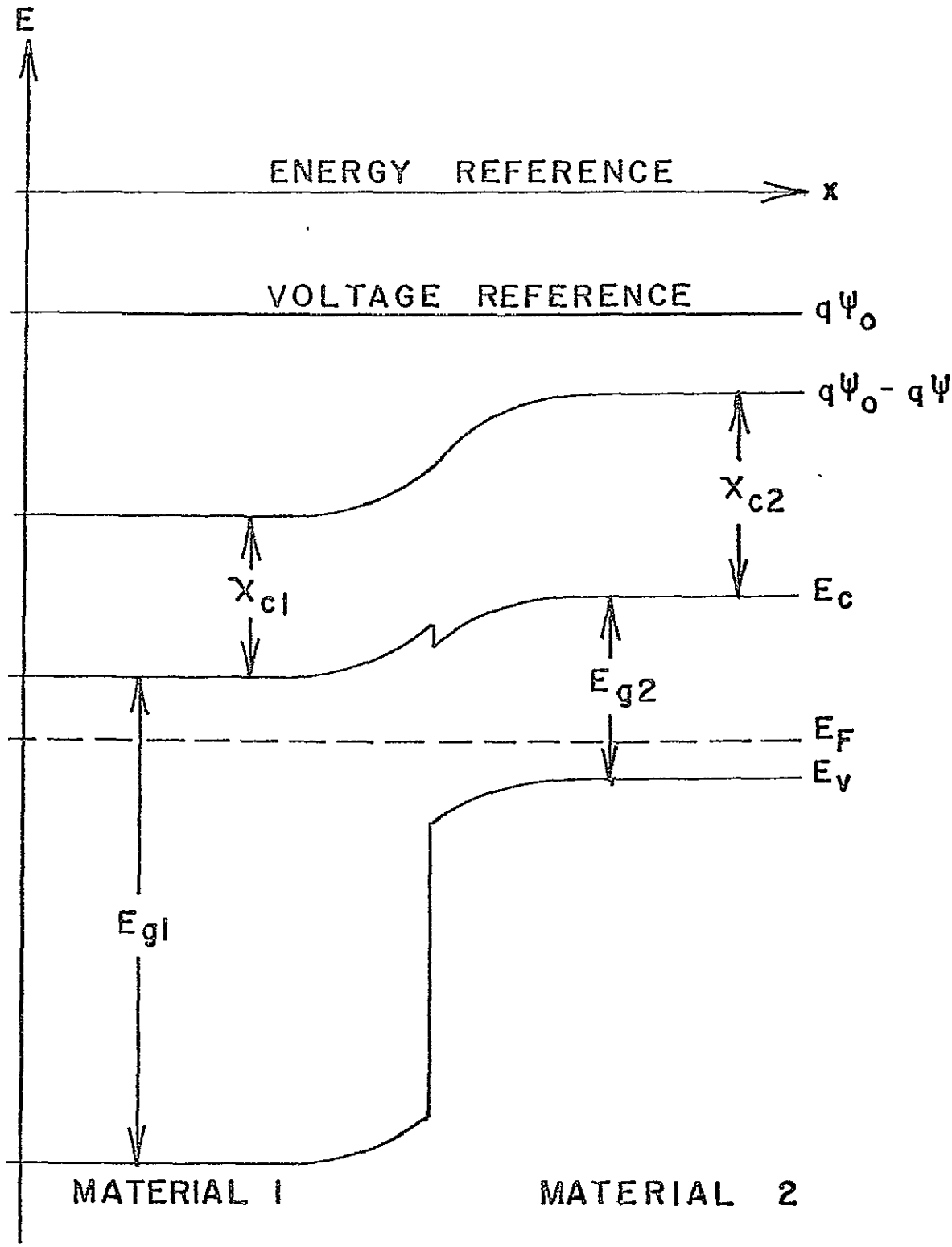

Figure 3.1 Electron energy band diagram for a heterojunction solar cell at equilibrium in the dark.

For a homogeneous material, χ_c, E_g, N_c, and N_v are constant throughout the device, and Equations (3.18) and (3.19) simplify to Equations (3.1) and (3.2). But for a variable composition structure, Equations (3.1) and (3.2) must be replaced by Equations (3.18) and (3.19), or by the simpler forms of Equations (3.12) and (3.13). As discussed in Chapter 2, effective fields acting on electrons and holes arise in Equations (3.18) and (3.19) from bandgap, electron affinity, and density of states variations with position.

The continuity Equations (3.3) and (3.4), apply equally well to heterogeneous or homogeneous materials. Poisson's equation, however, fails to reduce to the simple expression of Equation (3.5) when composition (and therefore dielectric constant, ε) is allowed to vary with position. The more general form which results from $\nabla \cdot \vec{D} = \rho$, is

$$\frac{d^2\psi}{dx^2} = -\frac{q}{\varepsilon}(p-n+N) - \frac{1}{\varepsilon}\frac{d\psi}{dx}\frac{d\varepsilon}{dx}. \qquad (3.20)$$

Thus, when the dielectric constant becomes a function of position, Equation (3.20) must replace Equation (3.5).

The carrier concentration equations demand no modification, but they can be written in a more convenient form for the purposes of computer analysis. Using Equations (3.10), (3.11), (3.14) and (3.15), Equations (3.7) and (3.8) become:

$$n = n_{i2}\exp\left[\frac{q}{kT}\left(\psi-\phi_n + \frac{\chi_c}{q} - \psi_o + \frac{kT}{q}\ln\frac{N_c}{n_{i2}}\right)\right] \qquad (3.21)$$

$$p = n_{i2}\exp\left[\frac{q}{kT}\left(\phi_p-\psi- \frac{\chi_c}{q} - \frac{E_g}{q} + \psi_o + \frac{kT}{q}\ln\frac{N_v}{n_{i2}}\right)\right] \qquad (3.22)$$

where n_{i2} = intrinsic carrier concentration of some reference material (taken as alloy component #2 in this work).

The composition dependent (and therefore position dependent) parameters can be conveniently grouped into two terms

$$\theta_n = \frac{\chi_c}{q} - \psi_o + \frac{kT}{q} \ell n \left(\frac{N_c}{n_{i2}}\right), \tag{3.23}$$

$$\theta_p = -\frac{1}{q}(\chi_c + E_g) + \psi_o + \frac{kT}{q} \ell n \left(\frac{N_v}{n_{i2}}\right). \tag{3.24}$$

Then, the carrier density equations can be written concisely as

$$n = n_{i2} \exp\left[\frac{q}{kT}(\psi - \phi_n + \theta_n)\right], \tag{3.25}$$

$$p = n_{i2} \exp\left[\frac{q}{kT}(\phi_p - \psi + \theta_p)\right]. \tag{3.26}$$

These expressions are analogous to the forms used in the computer analysis of homogeneous solar cells [19], i.e.

$$n = n_i \exp\left[\frac{q}{kT}(\psi - \phi_n)\right].$$

$$p = n_i \exp\left[\frac{q}{kT}(\phi_p - \psi)\right].$$

The parameters, θ_n and θ_p depend only on composition, and must be externally supplied as functions of position for the specific composition profile being considered.

The other auxilliary equations remain the same whether or not composition is spatially varying. However, it is important to note that several variables no longer can be assumed to be constant. In fact, the material parameters μ_n, μ_p, ε, n_i, n_1 and p_1 must be given as known functions of composition (or position, when the composition profile is known).

Thus, the complete one-dimensional mathematical model for variable composition solar cells consists of the following system of equations:

$$J_n = -q\mu_n n \frac{d\phi_n}{dx}, \tag{3.27}$$

$$J_p = -q\mu_p p \frac{d\phi_p}{dx}, \tag{3.28}$$

$$\frac{\partial n}{\partial t} = G_e - U + \frac{1}{q}\frac{dJ_n}{dx}, \tag{3.29}$$

$$\frac{\partial p}{\partial t} = G_e - U - \frac{1}{q}\frac{dJ_p}{dx}, \tag{3.30}$$

$$\frac{d^2\psi}{dx^2} = -\frac{q}{\varepsilon}(p-n+N) - \frac{1}{\varepsilon}\frac{d\psi}{dx}\frac{d\varepsilon}{dx} \tag{3.31}$$

$$U = \frac{np-n_i^2}{\tau_{no}(p+p_1) + \tau_{po}(n+n_1)}, \tag{3.32}$$

$$n = n_{i2} \exp\left[\frac{q}{kT}(\psi-\phi_n+\theta_n)\right], \tag{3.33}$$

$$p = n_{i2} \exp\left[\frac{q}{kT}(\phi_p-\psi+\theta_p)\right], \tag{3.34}$$

with the following parameters given as functions of position:

$$N = N(x) = N_D^+ - N_A^-, \text{ net doping profile} \tag{3.35}$$

$$C = C(x), \text{ composition profile} \tag{3.36}$$

(for example, C = mole fraction, x, of AlAs in an $Al_xGa_{1-x}As$ solar cell)

$$\mu_n = \mu_n(x), \text{ electron mobility} \tag{3.37}$$

$$\mu_p = \mu_p(x), \text{ hole mobility} \tag{3.38}$$

$$\varepsilon = \varepsilon(x), \text{ dielectric constant} \tag{3.39}$$

$$n_i = n_i(x), \text{ intrinsic carrier concentration} \tag{3.40}$$

$$n_1 = n_1(x), \text{ trapping center parameter for electrons} \tag{3.41}$$

$$p_1 = p_1(x), \text{ trapping center parameter for holes} \tag{3.42}$$

$$\tau_{no} = \tau_{no}(x), \text{ excess carrier lifetime in p+ material} \tag{3.43}$$

$$\tau_{po} = \tau_{po}(x), \text{ excess carrier lifetime in } n^+ \text{ material} \tag{3.44}$$

$$E_g = E_g(x), \text{ bandgap} \tag{3.45}$$

$$\theta_n = \theta_n(x), \text{ conduction band parameter} \tag{3.46}$$

$$\theta_p = \theta_p(x), \text{ valence band parameter} \tag{3.47}$$

$$G_e = G_e(x), \text{ optical generation rate} \tag{3.48}$$

The position dependence of these parameters can arise from compositional changes and/or doping changes with position. The parameters ε, θ_n, θ_p, n_i, n_1, p_1 are fundamentally functions of composition C(x). The parameters μ_n and μ_p are functions of both doping density and alloy composition. The generation rate, G_e, has an intrinsic position dependence as well as a composition dependence. Finally τ_{no} and τ_{po} are assumed to depend on the density of intrinsic recombination sites as well as the density of dislocations introduced by lattice mismatch in graded compositional materials. Magnetic fields and thermal gradients are assumed to be negligible. Additional discussion of the modeling of these various material parameters is given in Chapter 4.

This apparently unwieldy mathematical system can actually be reduced to three equations in three unknowns in exactly the same manner used for homogeneous solar cells in previous computer models. The fact that

composition (and the associated material parameters) is allowed to vary through the cell simply adds some complexity to the detailed computations without altering the method of solution. The next section discusses the techniques used to solve the device equations by computer.

3.4 Computer Solution by Quasilinearization

Although previous reports by Graham and Dunbar [13,19] will prove useful as references for the detailed computer techniques, this section discusses those ideas concerning the numerical solution of the device equations that are most important in understanding the analysis results that follow. In order to maximize the accuracy and minimize routine calculations, all basic variables are normalized by the constants given in Table 3.1 before the solution process begins. The normalized steady state device equations for variable composition solar cells are, from Section 3.3 and Table 3.1,

$$J_n = n\mu_n \frac{\partial \phi_n}{\partial x} \tag{3.49}$$

$$J_p = p\mu_p \frac{\partial \phi_p}{\partial x} \tag{3.50}$$

$$0 = G_e - U - \frac{\partial J_n}{\partial x} \tag{3.51}$$

$$0 = G_e - U + \frac{\partial J_p}{\partial x} \tag{3.52}$$

$$\frac{d^2\psi}{dx^2} = \frac{1}{\varepsilon}\left[n-p-N-\frac{d\varepsilon}{dx}\frac{d\psi}{dx}\right] \tag{3.53}$$

$$n = \exp\left[\psi-\phi_n+\theta_n\right] \tag{3.54}$$

$$p = \exp\left[\phi_p-\psi+\theta_p\right] \tag{3.55}$$

Table 3.1 Normalization constants (Subscript "2" indicates semiconductor #2 in alloy, GaAs in this work).

Normalized Variable	Description	Normalizing Constant
x	position	$L_D = \sqrt{\varepsilon_2 V_T / q n_{i2}}$
τ_{no}, τ_{po}	lifetimes	L_D^2/D_o
ψ	electrostatic potential	$V_T = kT/q$
ϕ_n, ϕ_p	quasi-Fermi potentials	V_T
V_A	terminal voltage	V_T
E	electric field	V_T/L_D
n, p, n_1, p_1, n_i	carrier densities	$n_{i2} = \sqrt{N_{c2} N_{v2} \exp(-E_{g2}/kT)}$
N, N_D, N_A	net impurity, donor, acceptor concentrations	n_{i2}
J, J_n, J_p	current densities	$-qD_o n_{i2}/L_D$
D_n, D_p	carrier diffusion constants	$D_o = 1 cm^2/sec$
μ_n, μ_p	carrier mobilities	D_o/V_T
U	generation-recombination rate	$D_o n_{i2}/L_D^2$
G_e	optical generation rate	$D_o n_{i2}/L_D^2$
S	recombination velocity	D_o/L_D
θ_n, θ_p	band structure parameters	V_T
N_c, N_v	effective densities of states	n_{i2}
E_g	bandgap	kT
χ_c	electron affinity	kT
ε	relative dielectric constant	ε_2

$$U = \frac{np - n_i^2}{\tau_{no}(p+p_1) + \tau_{po}(n+n_1)} \tag{3.56}$$

Taking ψ, ϕ_n, and ϕ_p as the set of independent variables, the above eight equations can be reduced to three differential equations of the form:

$$\frac{d^2\psi}{dx^2} = F_1(\psi, \phi_n, \phi_p, \psi') \tag{3.57}$$

$$\frac{d^2\phi_n}{dx^2} = F_2(\psi, \phi_n, \phi_p, \psi', \phi_n') \tag{3.58}$$

$$\frac{d^2\phi_p}{dx^2} = F_3(\psi, \phi_n, \varphi_p, \psi', \phi_p') \tag{3.59}$$

where the primes indicate differentiation with respect to x. For reference, the three functions F_1, F_2, and F_3 are given below.

$$F_1(\psi, \phi_n, \phi_p, \psi') = \frac{1}{\varepsilon}\left[\exp(\psi-\phi_n+\theta_n) - \exp(\phi_p-\psi+\theta_p) - N - \frac{d\varepsilon}{dx}\frac{d\psi}{dx}\right] \tag{3.60}$$

$$F_2(\psi, \phi_n, \phi_p, \psi, \phi_n') = \frac{G_e \exp(\phi_n-\psi-\theta_n)}{\mu_n} - \frac{1}{\mu_n}\frac{d\phi_n}{dx}\frac{d\mu_n}{dx} - \frac{d\phi_n}{dx}\left(\frac{d\psi}{dx} - \frac{d\phi_n}{dx} + \cdots\right.$$

$$\left.\cdots \frac{d\theta_n}{dx}\right) + \frac{\exp(\theta_p) - \exp(\phi_p-\phi_n+\theta_p)}{\mu_n \exp(\psi-\phi_n)\left[\tau_{no}\exp(\phi_p-\psi+\theta_p) + p_1\tau_{no}+\tau_{po}\exp(\psi-\phi_n+\theta_n) + n_1\tau_{po}\right]} \tag{3.61}$$

$$F_3(\psi, \phi_n, \phi_p, \psi, \phi_p') = -\frac{G_e \exp(\psi-\phi_p-\theta_p)}{\mu_p} - \frac{1}{\mu_p}\frac{d\phi_p}{dx}\frac{d\mu_p}{dx} - \frac{d\phi_p}{dx}\left(\frac{d\phi_p}{dx} - \cdots\right.$$

$$\left.\cdots \frac{d\psi}{dx} + \frac{d\theta_p}{dx}\right) - \frac{\exp(\theta_n) - \exp(\phi_p-\phi_n+\theta_n)}{\mu_p \exp(\phi_p-\psi)\left[\tau_{no}\exp(\phi_p-\psi+\theta_p)+p_1\tau_{no}+\tau_{po}\exp(\psi-\phi_n+\theta_n)+n_1\tau_{po}\right]} \tag{3.62}$$

As discussed in Chapter 4, the parameters ε, G_e, N, n_1, p_1, τ_{no}, τ_{po}, θ_n, θ_p, μ_n, μ_p must be evaluated as functions of position.

The method of solution used in the present research is identical to that used by Graham and Dunbar for less complicated structures [13,19]. Briefly, the computer program accepts input data specifying device structure and terminal voltage, and uses first order approximations and/or available data on previous solutions for a similar device to produce an initial estimate for each of the variables in the arguments of F_1, F_2 and F_3. Linear approximations to Equations (3.57 - 3.59) are then obtained by expanding F_1, F_2 and F_3 in function space about the initial estimate and truncating the resulting series to eliminate higher order (nonlinear) terms. These approximations are used to generate a new estimate for the variables ψ, ϕ_n and ϕ_p and the process is repeated. If the initial estimate was close enough to the exact solution, this iterative procedure will converge to a solution of the original set of equations, i.e. a position dependence for ψ, ϕ_n, and ϕ_p throughout the solar cell. Further calculations on these three variables provide profiles of physically meaningful quantities such as electron and hole concentrations and current densities everywhere within the device. These results can then be examined to insure that the program's iterative process has converged to a physically reasonable solution.

The operation of the main solar cell analysis program is summarized in Figure 3.2. First, the material parameters for the ternary alloy system are initialized and the specifications (doping levels, layer thicknesses, polarity, etc.) for the desired structure are read in. The terminal voltage is then read in, and the program calculates an

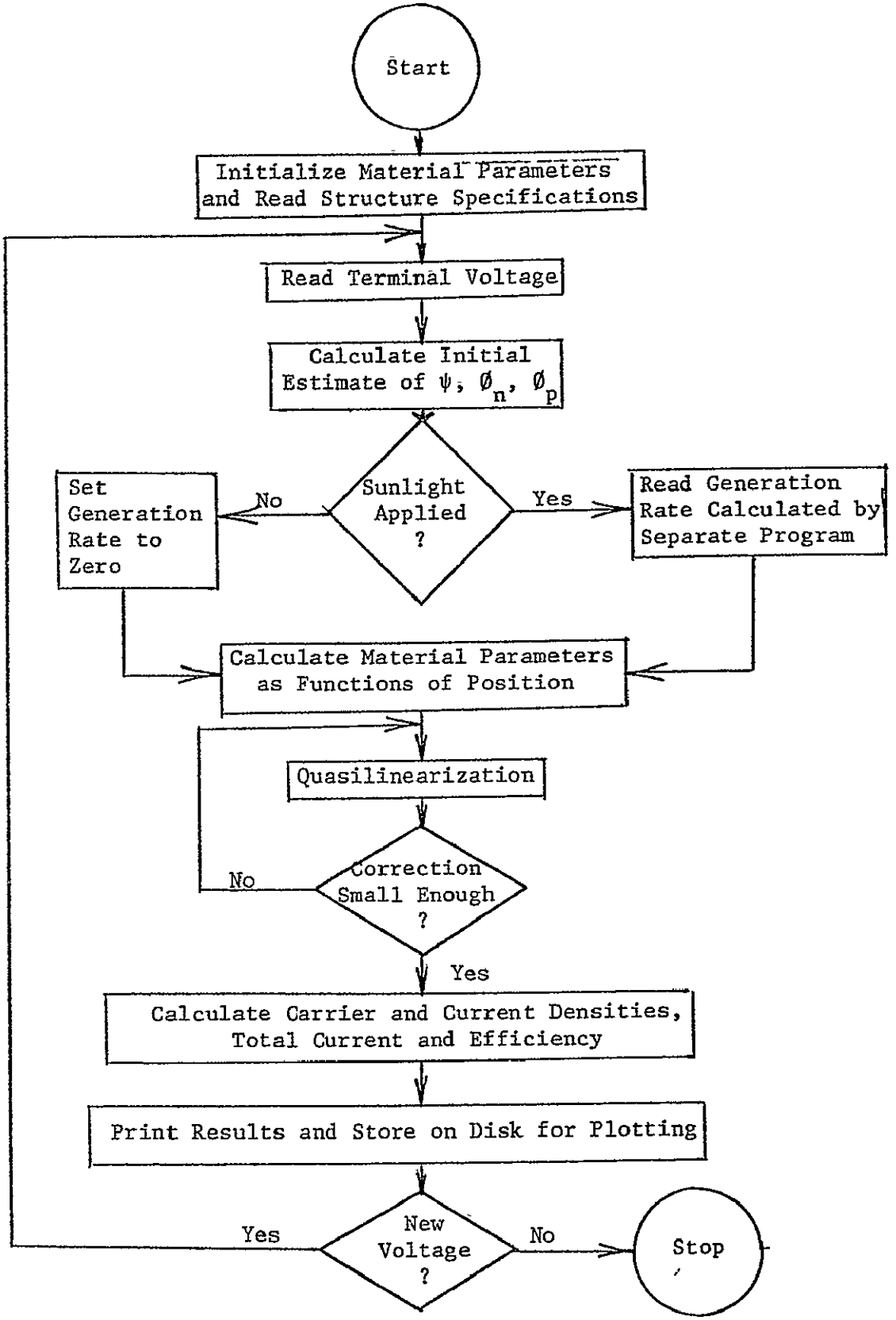

Figure 3.2 Flow chart for main variable composition solar cell analysis program.

initial estimate for the three independent variables ψ, ϕ_n, and ϕ_p. If the same device structure has been previously analyzed (perhaps at slightly different lighting and voltage levels) data may be recalled from disk storage to provide an initial estimate. However, if no previous analysis has been done, the program must build up an initial estimate in stages, beginning with an analysis of a homogeneous cell in darkness with zero volts across the terminals. The composition profile is then built up in steps by using the previous solution as an initial estimate for determining a more exact solution by quasilinearization. Once the composition profile is established, the terminal voltage is stepped up in a similar fashion until the expected open circuit voltage has been exceeded. Next, the illumination intensity (i.e., generation rate) is built up in steps. As soon as this stepping process is complete, the terminal voltage can be swept down again to obtain a complete J-V characteristic for the cell under full lighted conditions.

As shown in the flow chart, the results can be obtained in both plotted and tabulated form. Figures 3.3 through 3.12 present a sample of the plotted output that the analysis program produced for an AlAs-GaAs heterojunction solar cell with a window thickness of 0.1 μM and an abrupt p-n junction placed 0.4 μM below the surface. The abrupt change in bandgap and electron affinity at the 0.1 μM heterojunction is clearly evident in the equilibrium band diagram of Figure 3.3. The built-in fields around the heterojunction and p-n junction can be seen in Figure 3.4, which shows the electrostatic potential near the surface under AM0 conditions at various terminal voltages. Figures 3.5 and 3.7 show the position dependence of electron and hole current densities for the entire solar cell depth while Figures 3.6 and 3.8 are expanded views

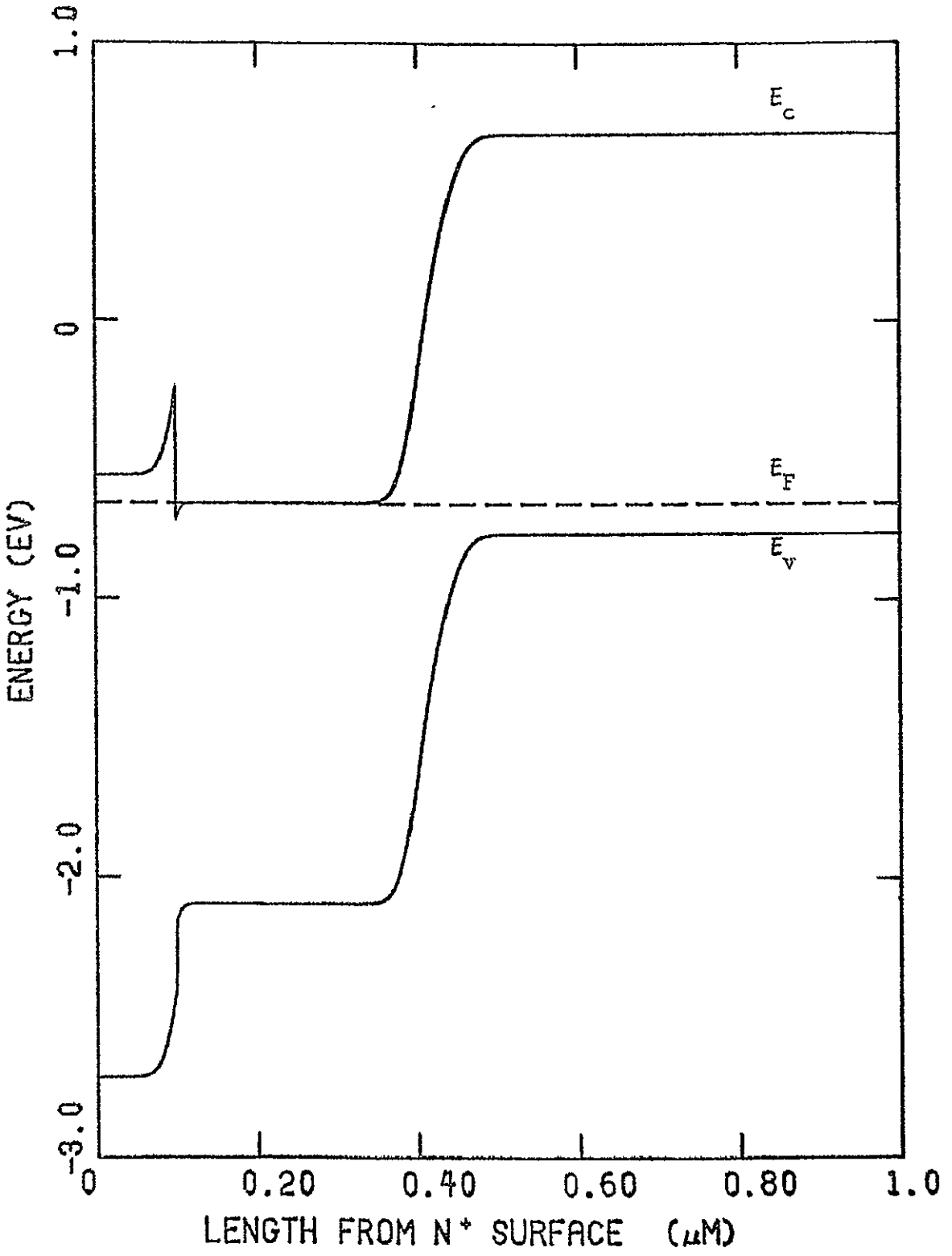

Figure 3.3 Equilibrium band diagram for an abrupt heterojunction AlAs-GaAs solar cell calculated and plotted by computer.

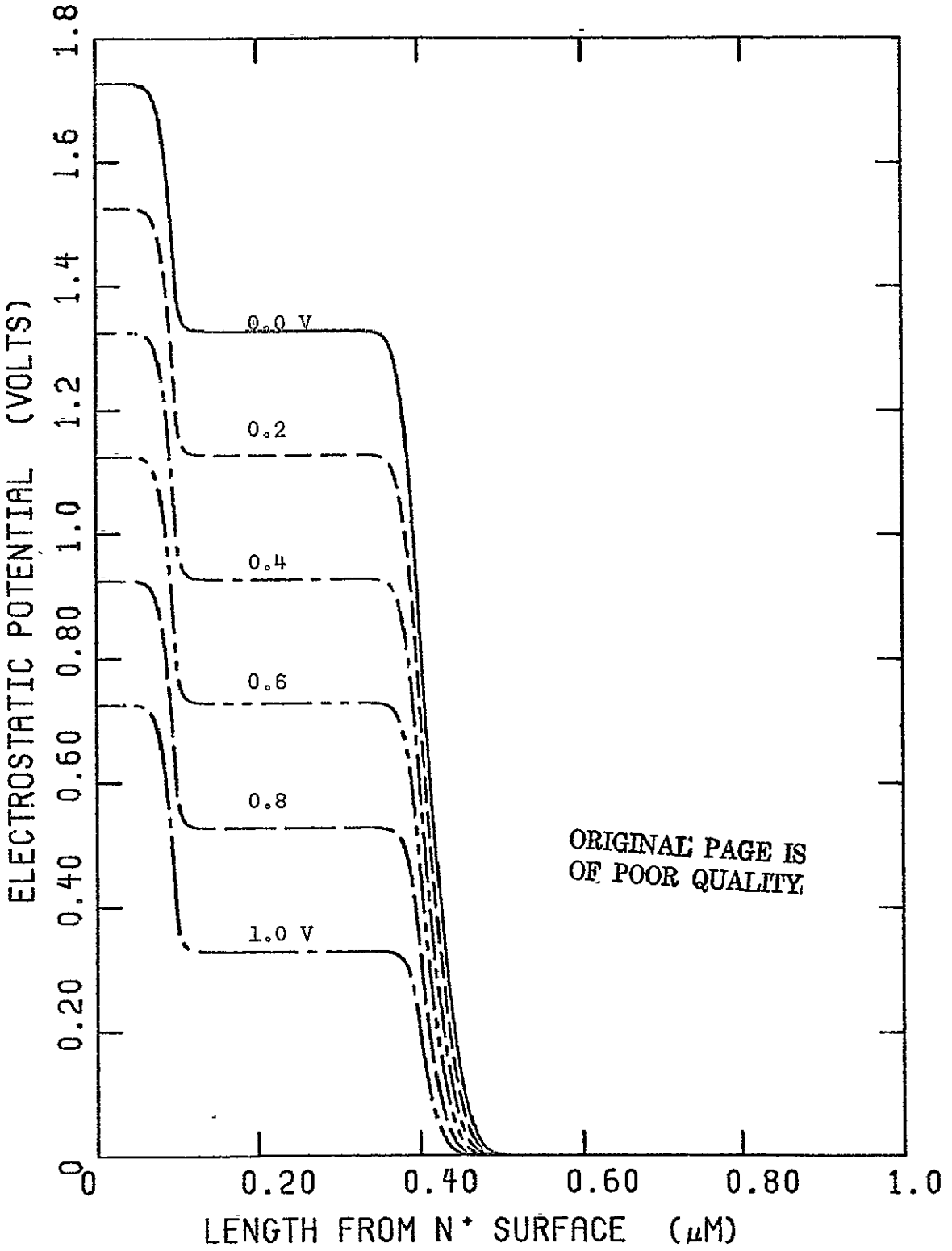

Figure 3.4 Computer-drawn electrostatic potential near the surface of a heterojunction cell under AM0 conditions at various terminal voltages. The heterojunction is at 0.1 μM and the p-n junction is at 0.4 μM.

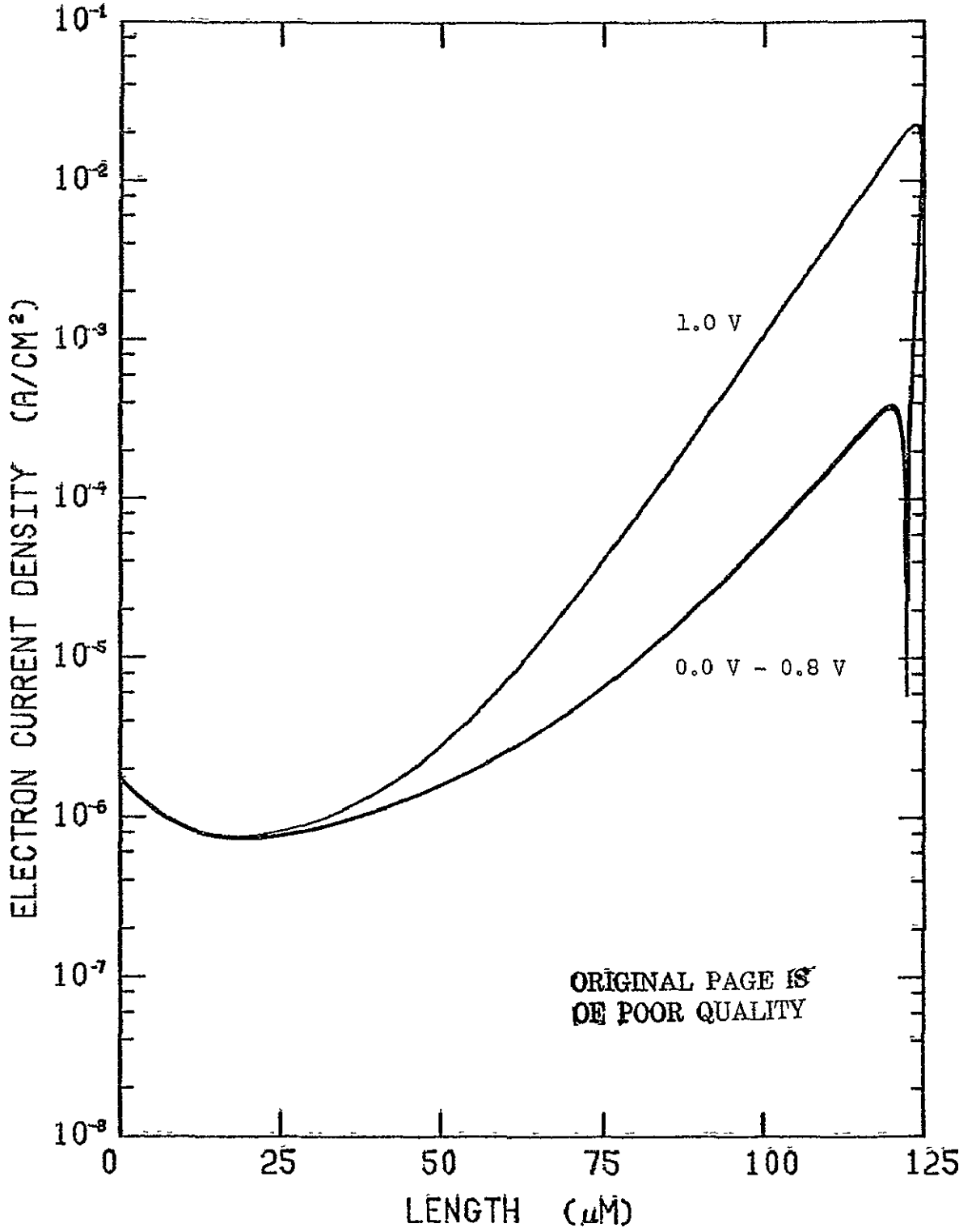

Figure 3.5 Electron current density through the entire depth of an abrupt heterojunction solar cell.

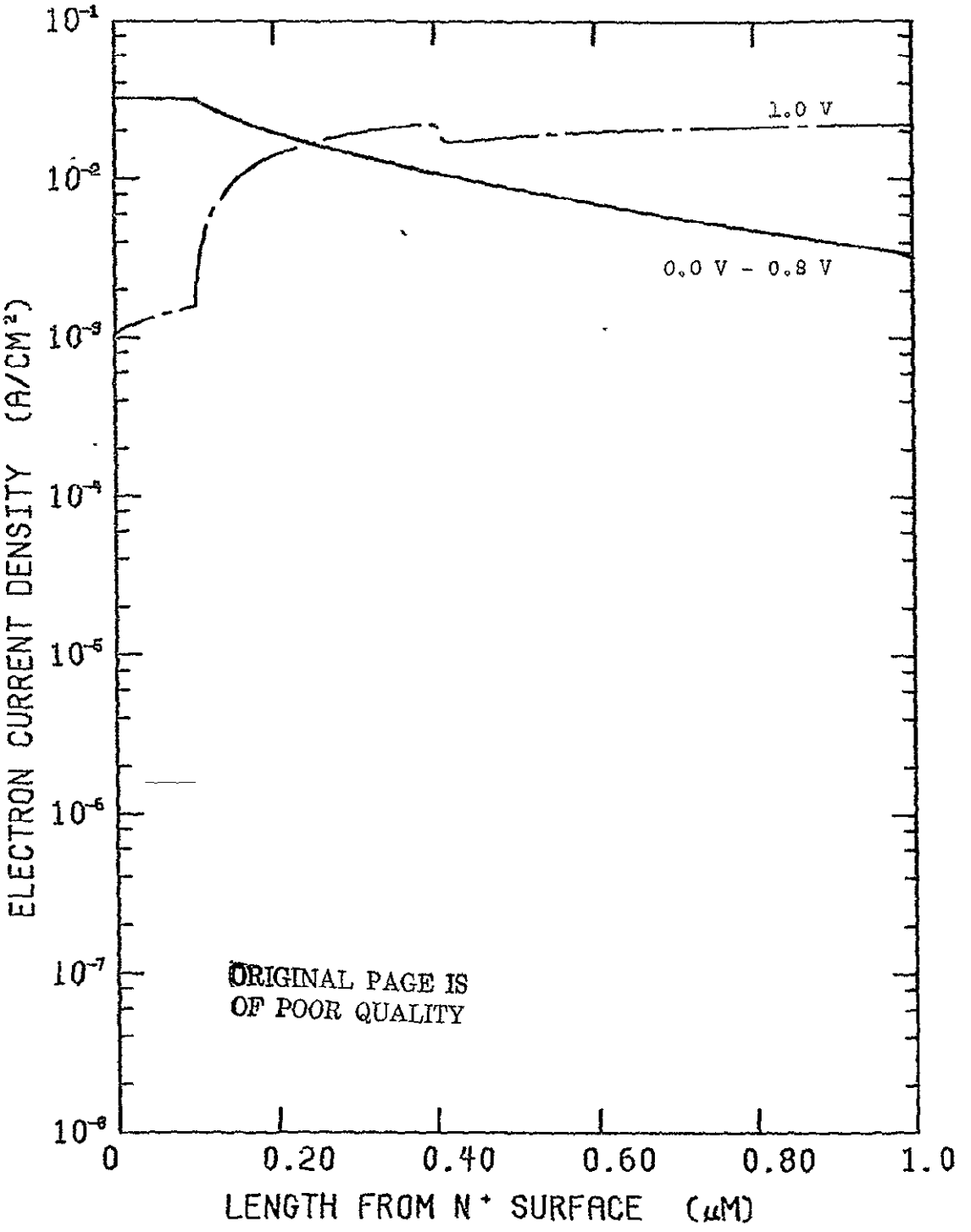

Figure 3.6 Expanded plot of electron current density near the front surface.

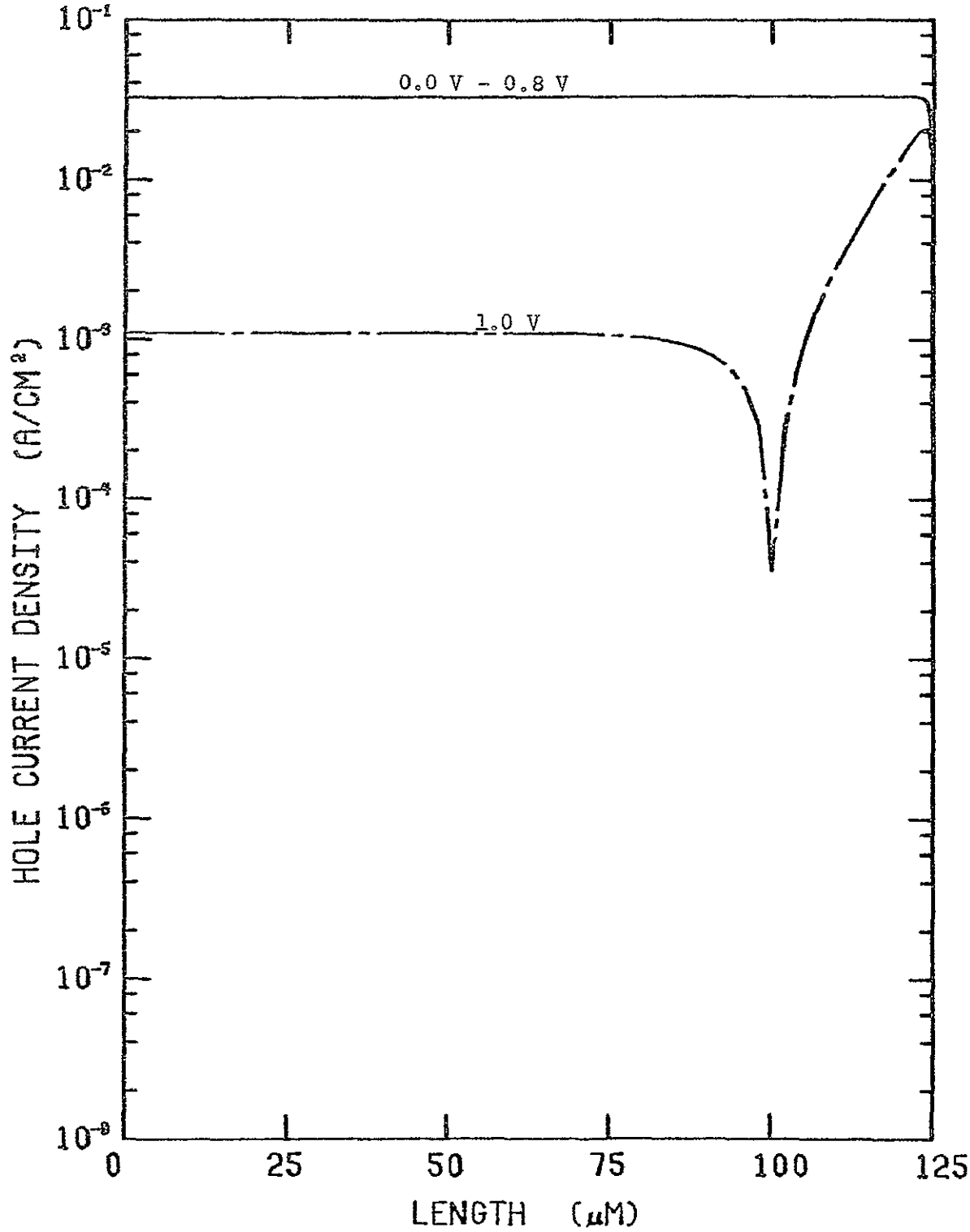

Figure 3.7 Hole current density as a function of position through the entire depth of an abrupt heterojunction solar cell.

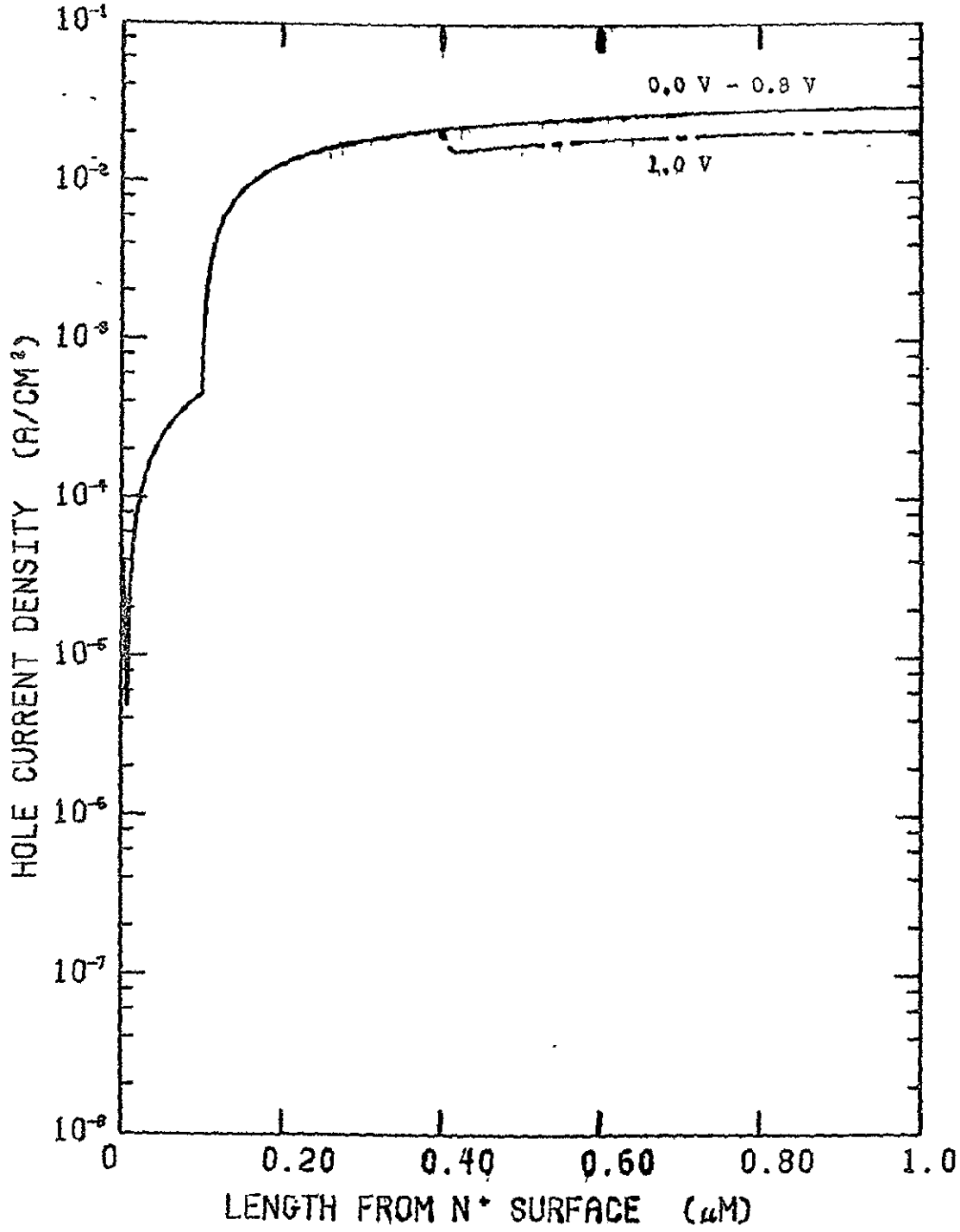

Figure 3.8 Expanded plot of hole current density near the front surface.

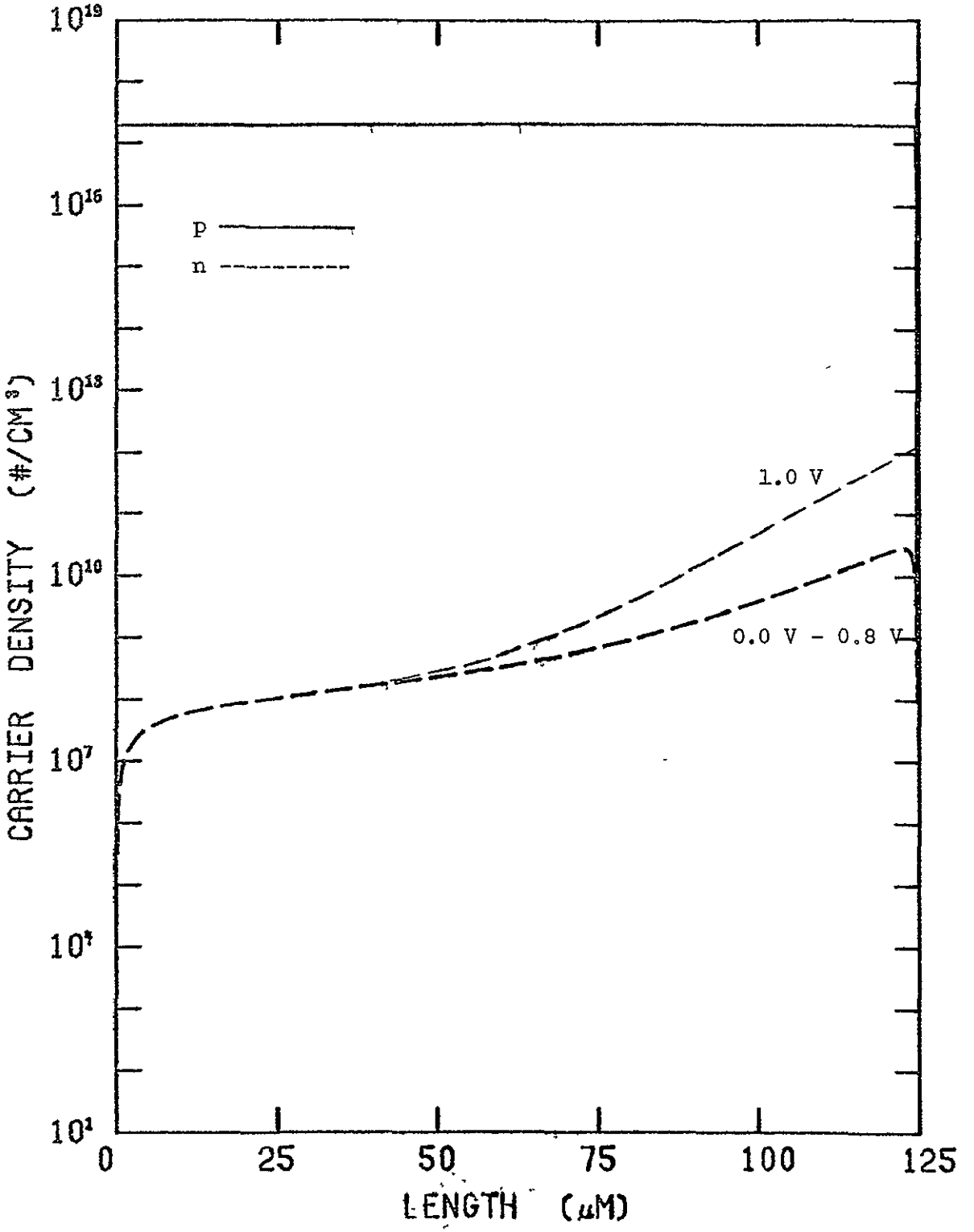

Figure 3.9 Electron and hole densities through the entire solar cell depth.

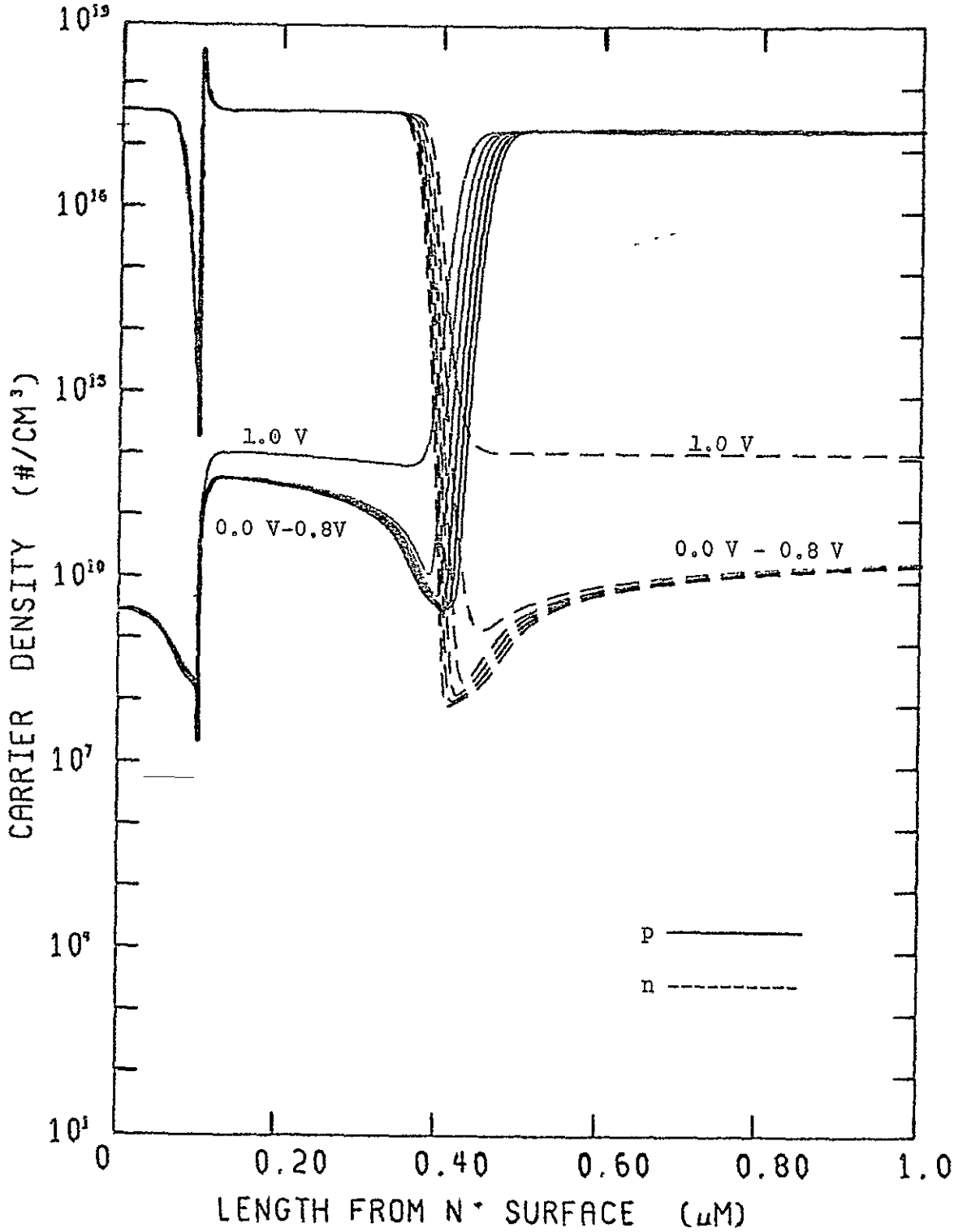

Figure 3.10 Expanded plot of electron and hole densities around the heterojunction and p-n junction near the front surface.

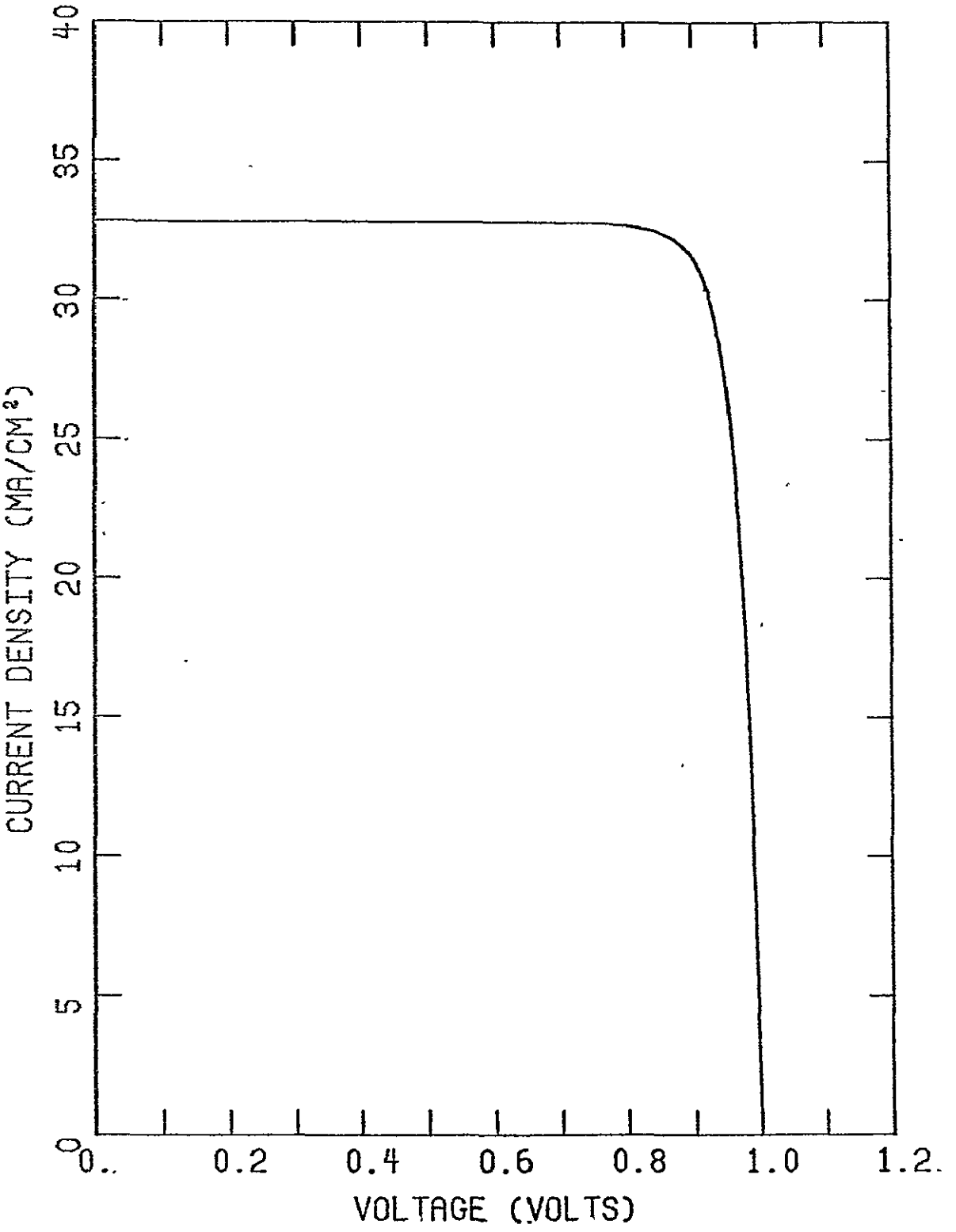

Figure 3.11 J-V characteristic produced by computer analysis of an abrupt heterojunction AlAs-on-GaAs solar cell.

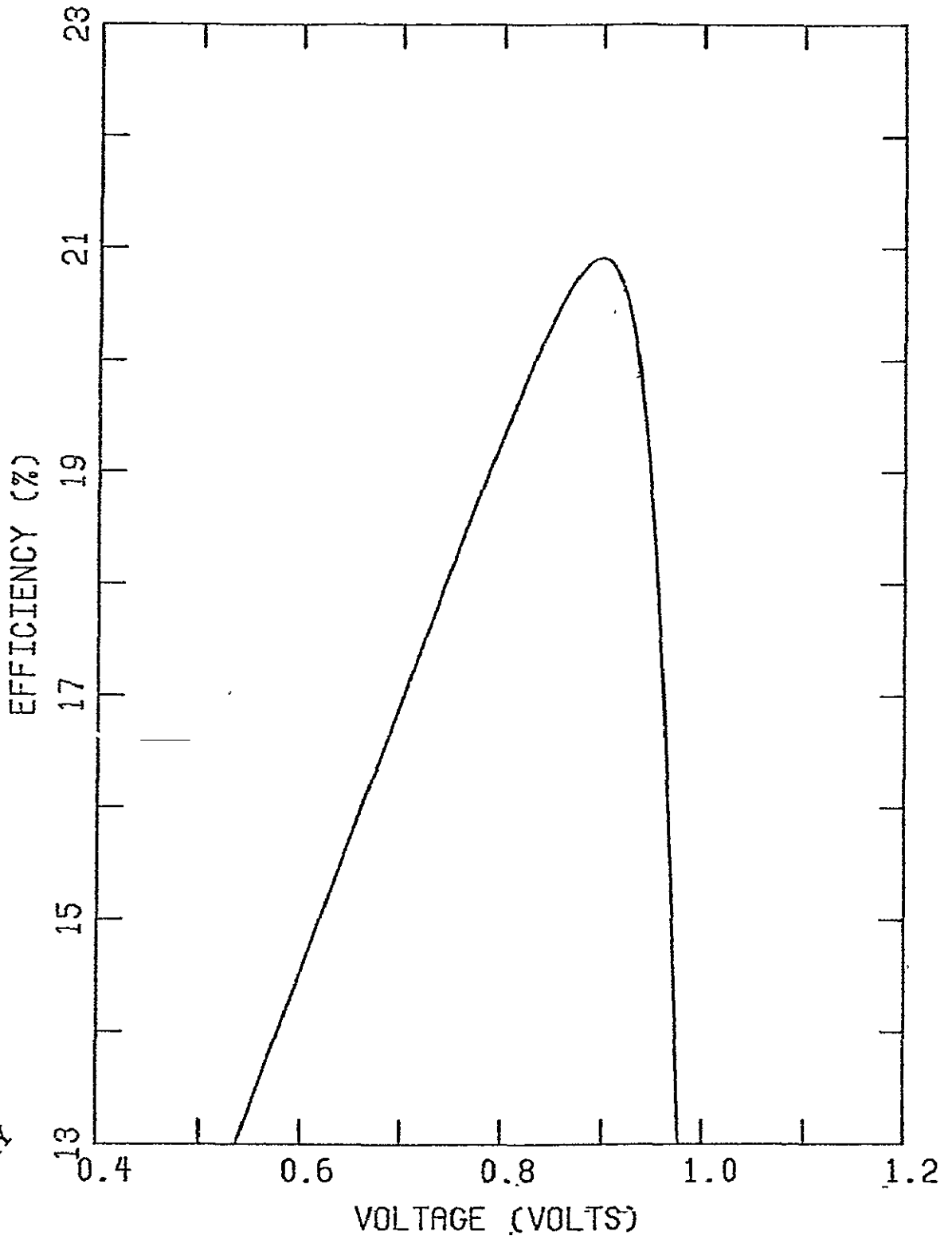

Figure 3.12 Dependence of efficiency on terminal voltage for an abrupt heterojunction AlAs-on-GaAs solar cell as calculated by computer simulation.

of the same data near the front surface. Although the carrier densities plotted in Figure 3.9 appear relatively smooth, an expanded view (Figure 3.10) near the surface shows the large changes in carrier concentration that occur around an abrupt AlAs-GaAs heterojunction and an abrupt p-n junction.

The J-V characteristic calculated by the computer analysis program for this device is shown in Figure 3.11, and finally the dependence of peak efficiency on terminal voltage is plotted in Figure 3.12. The availability of data such as that shown in the preceding ten figures makes computer simulation a useful tool in determining the device characteristics that control solar cell behavior.

4. MATERIAL PARAMETER MODELING

4.1 Introduction

As mentioned in earlier chapters, various material parameters must be given as functions of position before the device equations can be solved. The material parameter modeling discussed in the following sections makes possible the computer analysis of solar cells made of a spatially varying alloy of two compatible semiconductors. Given the material properties of the two binary materials, the computer program generates approximate parameters for the specified ternary composition profile. For example, solar cells made of the alloy, $Al_xGa_{1-x}As$, are analyzed by providing the material properties of AlAs and GaAs, along with the desired composition profile, i.e. the mole fraction of AlAs, x, vs. position. The program then uses this information to determine the values of the parameters needed for the device equations at each point within the solar cell. Equations of both a theoretical and empirical nature have been used to obtain the alloy material parameters from the corresponding binary material parameters. Whenever possible, these approximations have been checked against experimental results and adjusted to improve the agreement with available data. The most important approximations are described in the following sections.

4.2 Dielectric Constant vs. Composition

Given the dielectric constants, ε_1 and ε_2, for semiconductors 1 and 2, the following interpolation scheme is used to estimate the dielectric constant, ε, for an alloy that has mole fraction, C, of material 1, [24]:

$$\varepsilon = \frac{1+2\left[C\left(\frac{\varepsilon_1-1}{\varepsilon_1+2}\right) + (1-C)\left(\frac{\varepsilon_2-1}{\varepsilon_2+2}\right)\right]}{1-C\left(\frac{\varepsilon_1-1}{\varepsilon_1+2}\right) - (1-C)\left(\frac{\varepsilon_2-1}{\varepsilon_2+2}\right)} \qquad (4.1)$$

This form was used to approximate the values of the high frequency dielectric constant, ε_h, and the low frequency dielectric constant ε_ℓ, both of which are needed in the mobility calculations to be discussed in later sections.

4.3 Band Structure Parameters vs. Composition

4.3.1 Introduction

$Al_xGa_{1-x}As$ and $GaAs_{1-x}P_x$ have both a direct and an indirect bandgap which are important over various alloy compositions, and the solar cell program permits the specification of two valleys, as shown in Figure 4.1, each with its own composition dependent parameters such as bandgap, effective mass and mobility. Since the mean time between intervalley scattering is about 10^{-12} sec (or less), these two electron populations are essentially at equilibrium with each other and a single electron quasi-Fermi potential, ϕ_n, can be used in the device equations. Then an "effective" electron mobility and "effective" electron mass can be defined such that a single current density equation (Equation 3.27) and a single carrier density equation (Equation 3.33) is sufficient for this two conduction band valley model. The following sections describe the techniques used to determine the resultant band structure parameters (such as electron and hole mobilities) of an alloy, from the band structure parameters for each of the two components.

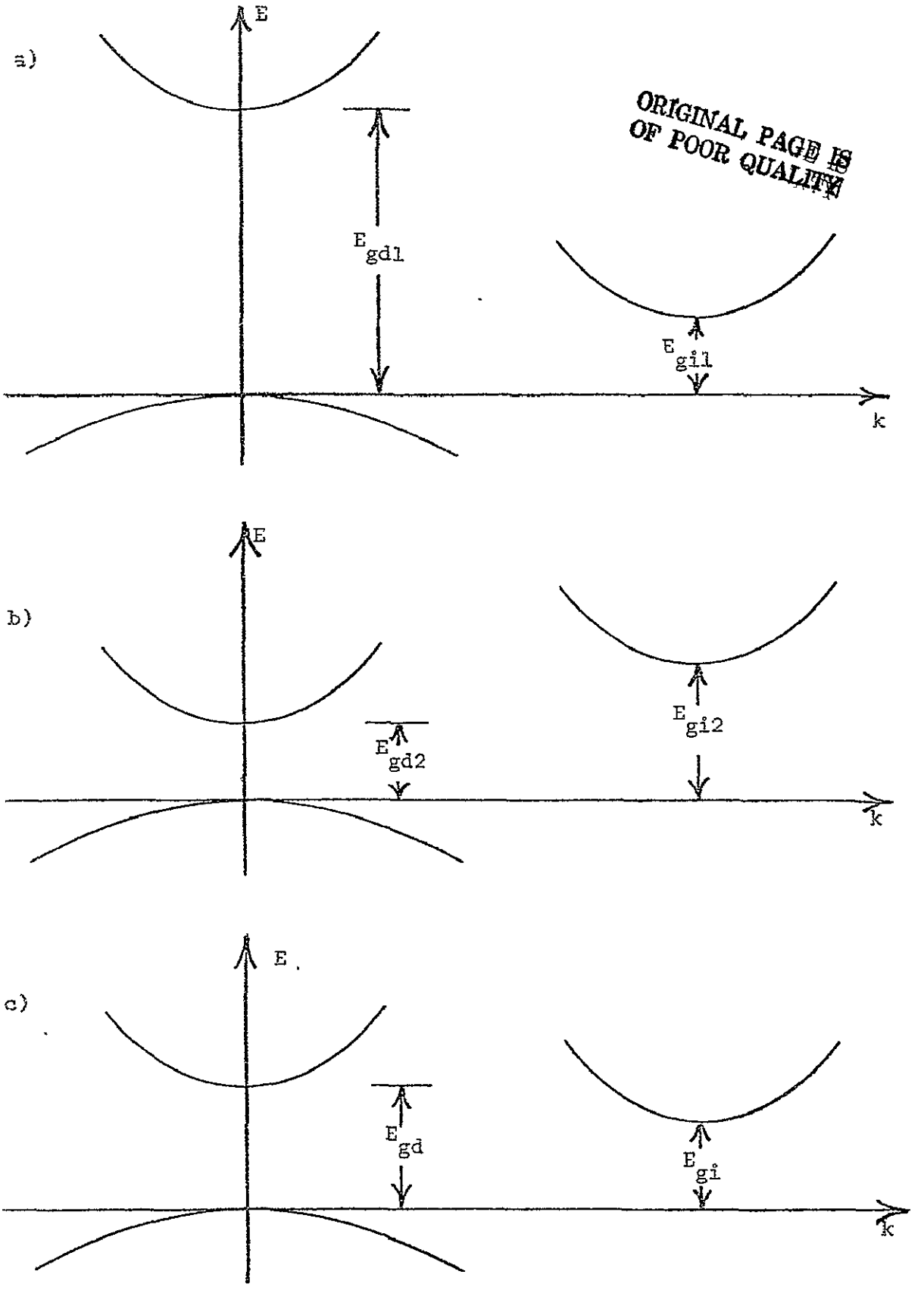

Figure 4.1 Electron energy, E, vs. wave vector, k, for a) indirect semiconductor, material 1, b) direct semiconductor, material 2, c) alloy of materials 1 and 2.

4.3.2 Bandgap vs. Composition

Experimental studies have shown that the direct energy gap for III-V alloys has an approximately quadratic dependence on composition such as

$$E_{gd} = aC^2 + bC + E_{gd2} \tag{4.2}$$

where a and b are experimental values. The same form was used to model the indirect variation in $GaAs_{1-x}P_x$, while for $Al_xGa_{1-x}As$, the indirect gap was estimated by a linear variation with composition. The bandgap is the minimum of the direct or indirect bandgaps.

4.3.3 Effective Masses

The next task is to determine the effective masses for holes and electrons. Since the valence band in each of the two semiconductors is assumed to have a single dominant valley with a characteristic effective mass, it is simply necessary to interpolate between the two effective masses to approximate the resultant hole effective mass for the alloy. The following interpolation form was used [24]:

$$\frac{1}{m_p^*} = \frac{C}{m^*_{p1}} + \frac{1-C}{m^*_{p2}} \tag{4.3}$$

where m^*_{p1} = hole effective mass in material 1

m^*_{p2} = hole effective mass in material 2

m^*_p = hole effective mass in alloy

C = mole fraction of material 1

The same form was used to find the electron effective mass for the indirect valley:

$$\frac{1}{m^*_{cd}} = \frac{C}{m^*_{cd1}} + \frac{1-C}{m^*_{cd2}} \tag{4.4}$$

where m^*_{cd1} = conduction band effective mass in direct valley for material 1.

m^*_{cd2} = conduction band effective mass in direct valley for material 2.

m^*_{cd} = conduction band effective mass in direct valley for alloy.

Likewise for the indirect valley:

$$\frac{1}{m^*_{ci}} = \frac{C}{m^*_{ci1}} + \frac{1-C}{m^*_{ci2}} \tag{4.5}$$

Now, it will prove useful to define, if possible, a single effective mass for all electrons. This can be done by considering the total electron density expressed as

$$n = N_{cd} \exp[\frac{E_{Fn}-E_{cd}}{kT}] + N_{ci} \exp[\frac{E_{Fn}-E_{ci}}{kT}], \tag{4.6}$$

where N_{cd} = direct valley effective density of states,

N_{ci} = indirect valley effective density of states

E_{cd} = direct valley minimum

E_{ci} = indirect valley minimum

It is desired to obtain the following form:

$$n = N_c \exp[\frac{E_{Fn}-E_c}{kT}] \tag{4.7}$$

where N_c = effective density of states for entire conduction band

E_c = absolute minimum of conduction band (the lesser of E_{cd} and E_{ci}).

Since $N_{cd} = K\, m^*_{cd}{}^{3/2}$

$N_{ci} = K\, m^*_{ci}{}^{3/2}$

$N_c = K\, m^*_n{}^{3/2}$

where K is a proportionality constant and m^*_n = effective mass for all electrons, then

$$m^*_n{}^{3/2} \exp[\frac{E_{Fn}-E_c}{kT}] = m^*_{cd}{}^{3/2} \exp[\frac{E_{Fn}-E_{cd}}{kT}] + m^*_{ci}{}^{3/2} \exp[\frac{E_{Fn}-E_{ci}}{kT}]$$

$$m^*_n = [m^*_{cd}{}^{3/2} \exp(\frac{E_c-E_{cd}}{kT}) + m^*_{ci}{}^{3/2} \exp(\frac{E_c-E_{ci}}{kT})]^{2/3}$$

or, in terms of bandgaps:

$$m^*_n = [m^*_{cd}{}^{3/2} \exp(\frac{E_g-E_{gd}}{kT}) + m^*_{ci}{}^{3/2} \exp(\frac{E_g-E_{gi}}{kT})]^{2/3} \qquad (4.8)$$

where E_{gd}, E_{gi}, E_g, m^*_{cd} and m^*_{ci} are given by Equations (4.2), (4.4), and (4.5).

4.3.4 Hole Mobility

Mobility depends not only on alloy composition, but on the doping level as well. In order to calculate hole mobility for an arbitrary doping and composition, an empirical formula, f_{p2}, was constructed to approximate the doping dependence of hole mobility for one of the alloy components, to be referred to as material 2:

$$\mu_{p2} = f_{p2}(N)$$

where N = total impurity concentration. The form of f_{p2} was taken to be

$$f_{p2}(N) = \frac{A_p}{(1+N/N_p)^{\alpha}}. \qquad (4.9)$$

Now, because

$$\mu_p = \frac{q\langle\tau_p\rangle}{m^*_p} = \mu_{p2}\,\frac{m^*_{p2}}{\langle\tau_{p2}\rangle}\,\frac{\langle\tau_p\rangle}{m^*_p}, \tag{4.10}$$

where $\langle\tau_p\rangle$ and $\langle\tau_{p2}\rangle$ are the mean times between scattering for holes in the alloy and in material 2, respectively, it is apparent that if $\langle\tau_p\rangle$ and m^*_p can be specified as functions of composition, then a reasonable approximation to hole mobility for any doping level and composition can be made. In the III-V semiconductors, it was assumed that mobility is controlled primarily by a polar optical phonon scattering process[1] of the form [25]

$$\langle\tau\rangle = \frac{K}{\sqrt{m^*}\left(\frac{1}{\varepsilon_h} - \frac{1}{\varepsilon_\ell}\right)} \tag{4.11}$$

where K is a proportionality constant for all materials and ε_h and ε_ℓ are the high and low frequency relative dielectric constants.

Combining Equations (4.10) and (4.11) then gives as an approximation to the mobility

$$\mu_p(N,C) = \frac{f_{p2}(N)\; m^{*\,3/2}_{p2}\left(\frac{1}{\varepsilon_{h2}} - \frac{1}{\varepsilon_{\ell 2}}\right)}{m^{*\,3/2}_{p}\left(\frac{1}{\varepsilon_h} - \frac{1}{\varepsilon_\ell}\right)}. \tag{4.12}$$

where m^*_{p2}, $\varepsilon_{\ell 2}$, and ε_{h2} are known parameters of material 2, and ε_ℓ, ε_h, and m^*_p are given as functions of composition by Equations (4.1) and (4.3).

---

[1] The validity of this assumption has been questioned for hole mobility in n-type indirect gap and p-type III-V semiconductors [48].

4.3.5 Electron Mobility

The modeling of electron mobility is more complex than hole mobility because of the indirect and direct bands. Treating the direct and indirect valleys independently, and using the same technique as described for hole mobility, a direct valley electron mobility, μ_d, and an indirect valley electron mobility, μ_i, can be determined approximately as:

$$\mu_d(N,C) = \frac{f_{n2}(N)\, m^*_{cd2}{}^{3/2}\left(\frac{1}{\varepsilon_{h2}} - \frac{1}{\varepsilon_{\ell 2}}\right)}{m^*_{cd}{}^{3/2}\left(\frac{1}{\varepsilon_h} - \frac{1}{\varepsilon_\ell}\right)} \tag{4.13}$$

$$\mu_i(N,C) = \frac{f_{n1}(N) m^*_{ci2}{}^{3/2}\left(\frac{1}{\varepsilon_{h1}} - \frac{1}{\varepsilon_{\ell 1}}\right)}{m^*_{ci}{}^{3/2}\left(\frac{1}{\varepsilon_h} - \frac{1}{\varepsilon_\ell}\right)} \tag{4.14}$$

where m^*_{cd2}, m^*_{ci1}, $\varepsilon_{\ell 2}$, $\varepsilon_{\ell 1}$, ε_{h2} and ε_{h1} are known parameters of materials 1 and 2, $f_{n2}(N)$ is an empirical function relating electron mobility to doping for material 2, $f_{n1}(N)$ is an empirical function relating electron mobility to doping for material 1 and ε_ℓ, ε_h, m^*_{cd} and m^*_{ci} are given by Equations (4.1), (4.4) and (4.5). The functions f_{n1} and f_{n2} used the same functional form as Equation (4.9). An "effective" mobility for use in the current density equation can be found by weighing the direct and indirect mobilities by their respective electron populations, as

$$\mu_n(N,C) = \mu_d R_d + \mu_i(1-R_d) \tag{4.15}$$

where R_d is the fraction of electrons in the direct valley given by the expression

$$R_d = \frac{n_d}{n_d+n_i} = \frac{1}{1+\left(\frac{m^*_{ci}}{m^*_{cd}}\right)^{3/2}\exp\left(\frac{E_{gd}-E_{gi}}{kT}\right)} \tag{4.16}$$

4.3.6 Electron Affinity

It is apparent from experimental data reported by others [26] that the electron affinity for a direct gap ternary alloy of two binary semiconductors is often approximately linearly related to the bandgap as

$$\chi_c = \chi_{c2} - K_a (E_{gd} - E_{g2}) \tag{4.17}$$

where χ_{c2} is the electron affinity for one binary semiconductor (material #2, having a direct bandgap), E_{g2} is the bandgap of material #2, E_{gd} is the direct bandgap of the alloy, and K_a is a proportionality constant associated with the alloy being considered.

The determination of electron affinity is slightly more complicated if one binary semiconductor (material #1) is indirect so that the alloy itself will be indirect over some range of composition. Since electron affinity is defined as the energy difference between the conduction band edge and the vacuum level, the relationship between absolute bandgap and electron affinity in the present work was approximated by

$$\chi_c = \chi_{c2} - K_a(E_{gd}-E_{g2}) + E_{gd} - E_g \tag{4.18}$$

where E_g is the absolute gap of the alloy. This equation preserves the linear relationship between the vacuum level and the direct valley conduction band minimum over both direct and indirect alloy compositions.

4.3.7 Band Parameters, θ_n and θ_p

In order to model the composition dependence of the band parameters, θ_n and θ_p, defined in Section 3.3, some knowledge of the variation of electron affinity, χ_c, and bandgap, E_g, must be available. It has been found to be advantageous to select the potential reference, ψ_o, so that

$\theta_n = \theta_p = 0$ when the mole fraction of material 1 is zero. In other words, θ_n and θ_p are zero in regions of the solar cell consisting entirely of material 2. Then, from Equations (3.23) and (3.24)

$$\psi_o = \frac{\chi_{c2}}{q} + \frac{kT}{q} \ell n \left(\frac{N_{c2}}{n_{i2}}\right), \tag{4.19}$$

or equivalently,

$$\psi_o = \frac{\chi_{c2}+E_{g2}}{q} - \frac{kT}{q} \ell n \left(\frac{N_{v2}}{n_{i2}}\right). \tag{4.20}$$

Now, inserting Equation (4.19) into Equation (3.23), and Equation (4.20) into Equation (3.24) gives

$$\theta_n = \frac{\chi_c - \chi_{c2}}{q} + \frac{kT}{q} \ell n \left(\frac{N_c}{N_{c2}}\right), \tag{4.21}$$

$$\theta_p = \frac{\chi_{c2} - \chi_c}{q} + \frac{E_{g2} - E_g}{q} + \frac{kT}{q} \ell n \left(\frac{N_v}{N_{v2}}\right). \tag{4.22}$$

Finally, in terms of effective mass

$$\theta_n = \frac{\Delta\chi_c}{q} + \frac{3}{2} \frac{kT}{q} \ell n \left(\frac{m^*_n}{m^*_{n2}}\right) \tag{4.23}$$

$$\theta_p = \frac{-(\Delta\chi_c + \Delta E_g)}{q} + \frac{3}{2} \frac{kT}{q} \ell n \left(\frac{m^*_p}{m^*_{p2}}\right) \tag{4.24}$$

where $\Delta E_g = E_g - E_{g2}$, and $\Delta\chi_c = \chi_c - \chi_{c2}$ are given as functions of composition by Equations (4.2) and (4.18).

Equations (4.23) and (4.24) are the forms used to compute the band parameters for an arbitrary ternary alloy of two binary materials.

4.4 Interface Recombination

At an abrupt interface between two semiconductors, lattice mismatch introduces trapping levels due to dangling bonds. The density of dangling bonds at such an abrupt heterojunction is given by [27]:

$$N_h = \frac{K|a_2^2 - a_1^2|}{a_2^2 a_1^2} \tag{4.25}$$

where a_1 and a_2 are the lattice constants of the two materials and $K = 4$ for a [100] interface, $K = 2\sqrt{2}$ for a [110] interface, and $K = 4/\sqrt{3}$ for a [111] interface. If the composition change is gradual, rather than abrupt, the trapping centers have been assumed to have a volume density that is proportional to the slope of the composition profile as

$$N_g = N_h \frac{dC}{dx} \tag{4.26}$$

These interface states have been incorporated into the Shockley-Read-Hall model by modification of the excess carrier lifetimes:

$$\frac{1}{\tau_{no}} = \frac{1}{\tau_{no}}\Big|_{Bulk} + N_g C_R \tag{4.27}$$

$$\frac{1}{\tau_{po}} = \frac{1}{\tau_{po}}\Big|_{Bulk} + N_g C_R \tag{4.28}$$

where C_R is the capture coefficient. Ettenberg and Kressel [28] obtained a value of 8×10^3 cm/s for the interface recombination velocity at an abrupt $Al_{0.5}Ga_{0.5}As$ - GaAs heterojunction, from which C_R can be calculated as

$$\frac{1}{C_R} = \frac{0.5N_h}{S} = \frac{(0.5)\left[\frac{4|a_2^2 - a_1^2|}{a_2^2\, a_1^2}\right]}{8\times10^3 \text{ cm/s}},$$

$$C_R = 5.2 \times 10^{-9} \text{ cm}^3/\text{s},$$

where the lattice constants a_1 and a_2 for AlAs and GaAs were taken as 5.661×10^{-8} cm and 5.654×10^{-8} cm, respectively [29].

4.5 Optical Carrier Generation

It is apparent from the equations discussed in Chapter 3 that an optical generation rate G_e for electron and hole pairs must be known as a function of position prior to the solution of the equations. This generation rate profile is calculated by means of a separate computer program in a manner similar to that used for homogeneous solar cells [19].

The program calculates the position dependence of the generation rate for a device made of an alloy of two compatible semiconductors covered by an antireflection layer of arbitrary thickness and made of SiO (see Figure 4.2).

The composition profile is arbitrary, and the program is designed to determine the most efficient thickness for the antireflection layer. The input data required consists of the optical properties (absorption coefficients and refractive indices) of the two semiconductors and SiO, and the intensity vs. wavelength profile of the solar spectrum. Although only AM0 conditions have been selected for calculations reported in this work, data for AM2 conditions is also available as a user option. The intensity profile of the solar spectrum is provided

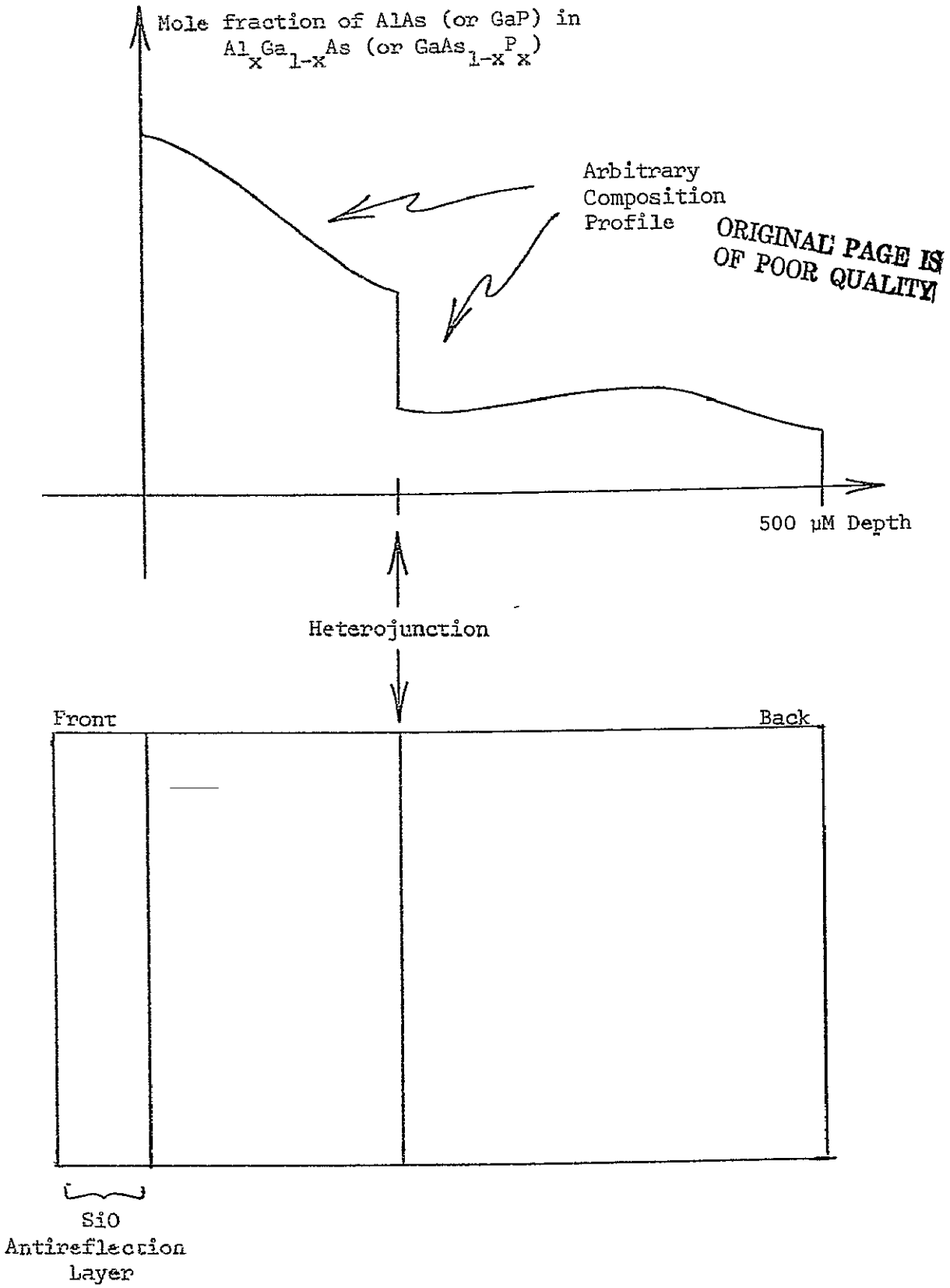

Figure 4.2 Device structure assumed for calculation of generation rate profile.

in terms of power density per wavelength interval $P(\lambda)$, at a finite number of wavelength values. This information then gives the incident photon density per second as

$$N_i(\lambda) = \frac{P(\lambda)\Delta\lambda}{E(\lambda)} \tag{4.29}$$

where $E(\lambda)$ is the average photon energy over the wavelength interval $\Delta\lambda$.

The program uses the absorption coefficient and refractive index data for SiO and the semiconductor alloy to determine a transmission coefficient $T(\lambda)$ for the antireflection layer. Thus the photon density per second entering the semiconductor (at $x = 0$) is

$$N(\lambda,0) = N_i(\lambda)\ T(\lambda). \tag{4.30}$$

At this point however, the calculations for variable composition solar cells begin to differ from those for homogeneous cells because the absorption coefficient α is a function of position as well as wavelength. If $N(\lambda,x)$ is the photon density per second passing any point at depth x beneath the semiconductor crystal surface, then the rate of change of photon density can be written

$$\frac{\partial N(\lambda,x)}{\partial x} = -\alpha[\lambda,C(x)]\ N(\lambda,x) \tag{4.31}$$

where $C(x)$ is the mole fraction of binary semiconductor #1 (such as AlAs) present in the ternary alloy ($Al_xGa_{1-x}As$ for example).

Since experimental absorption data is available for only a limited number of alloy compositions, an interpolation procedure was created to determine α for arbitrary wavelength and composition. Because the program allows for a two-conduction-band-valley model for an alloy between an indirect gap material (#1) and a direct gap material (#2) the

total absorption coefficient for a given wavelength was taken to be the sum of an absorption coefficient due to direct transitions and an absorption coefficient due to indirect transitions. The indirect coefficient was approximated by shifting the indirect portion of the α vs. E profile of material #1 by the difference between the indirect bandgaps of material #1 and the alloy. Similarly, the direct coefficient was approximated by shifting the α vs. E profile of material #2 by the difference between the direct bandgaps of material #2 and the alloy. This procedure only requires that the absorption coefficient vs. photon energy curves for both binary components be available, along with the bandgap vs. composition relationship (see Section 4.3.2) for the alloy. The results of this interpolation which is similar to that used by Hutchby [30], appear in Figures (5.5) and (5.9) in Chapter 5 for $Al_xGa_{1-x}As$ and $GaAs_{1-x}P_x$.

Now, if the composition profile, C(X) is known, then, by the above procedure, $\alpha(\lambda,x)$ is known, so that Equation (4.31) can be solved as

$$N(\lambda,x) = N(\lambda,0)\ \exp[-\int_o^x \alpha(\lambda,y)dy]. \tag{4.32}$$

Thus, if each absorbed photon generates one electron-hole pair, the generation rate for a given wavelength can be written as

$$G_e(\lambda,x) = -\frac{\partial N(\lambda,x)}{\partial x} = \alpha(\lambda,x)\ N(\lambda,0)\ \exp[-\int_o^x \alpha(\lambda,y)dy]. \tag{4.33}$$

Finally, the total generation rate for all values of λ is

$$G_e(x) = \sum_{\lambda} T(\lambda)N_i(\lambda)\alpha(\lambda,x)\ \exp[-\int_o^x \alpha(\lambda,y)dy]. \tag{4.34}$$

Of course, if the semiconductor composition does not vary with depth, then Equation (4.34) reduces to the simpler form used in

calculating the generation rate profile for homogeneous solar cells [19].

Figure 4.3 shows the flow chart for the program used to calculate the generation rate profile for analysis of variable composition cells. Among the secondary outputs available as user options are: the dependence of antireflection layer efficiency on layer thickness; the position dependence of the absorption coefficient; crystal surface and SiO refractive indices; and the total optical current available as a function of sample thickness. The details of the numerical techniques used in the program can be found in Reference [19].

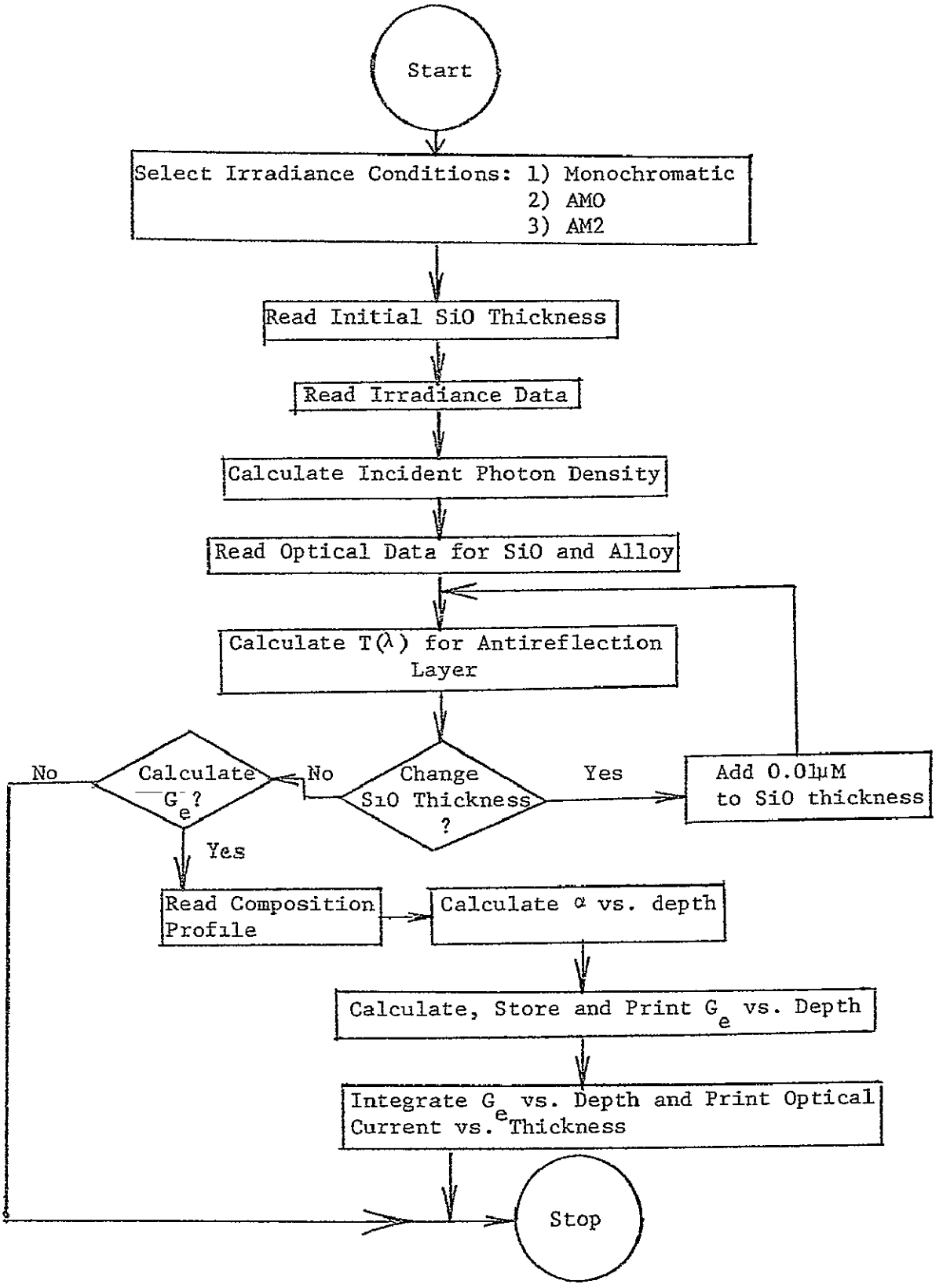

Figure 4.3 Flow chart for optical generation rate program.

5. PROPERTIES OF MATERIALS STUDIED

5.1 Introduction

At the present time, the computer program discussed in the preceding chapters has been used to analyze the performance of solar cells made of $Al_xGa_{1-x}As$, $In_xGa_{1-x}As$ and $GaAs_{1-x}P_x$. Since the results of these analyses must be interpreted in light of the experimental data fed into the program, this chapter presents the values used for the material parameters for these alloys. Every effort has been made to collect the latest, most reliable data in order to maximize the accuracy of the computer predictions.

5.2 Material Properties of $Al_xGa_{1-x}As$

One of the most promising alloys for solar cells is $Al_xGa_{1-x}As$. Since it has been used extensively in semiconductor laser research, its fabrication technology is well established and experimental data on its electrical and optical properties is relatively abundant. The lattice match between AlAs and GaAs is one of the best (less than .14% lattice mismatch) to be found among the material pairs suggested for solar cells so that recombination losses at any AlAs-GaAs heterojunction should be of minimum consequence [29]. In addition, AlAs is an indirect semiconductor with a much larger bandgap (2.16eV) than GaAs (1.439 eV) which is a direct material. Such a combination permits the selection of a wide range of optical properties that should lead to interesting computer analysis results.

The following material parameters were used in the computer analysis of $Al_xGa_{1-x}As$ solar cells. The subscript 1 refers to AlAs while the subscript 2 refers to GaAs.

The two sets of relative dielectric constants used were [35]:

low frequency: $\varepsilon_{\ell 1} = 10.9$

$\varepsilon_{\ell 2} = 13.2$

high frequency: $\varepsilon_{h1} = 8.5$

$\varepsilon_{h2} = 10.9$

The effective masses in terms of electron rest mass m_o were [36]:

holes: $m^*_{p1} = 0.85m_o$

$m^*_{p2} = 0.68m_o$

electrons:

direct valley: $m^*_{cd1} = 0.128\ m_o$

$m^*_{cd2} = 0.0636\ m_o$

indirect valley: $m^*_{ci1} = (0.37)(3)^{2/3}m_o$

$m^*_{ci2} = (0.39)(3)^{2/3}m_o$

All calculations were done for a temperature of 300°K. The single trapping center assumed by the Shockley-Read-Hall recombination model in Equation (3.32) was set near the center of the bandgap regardless of alloy composition so that

$$n_1 = p_1 = n_i \tag{5.1}$$

Of course the two parameters n_1 and p_1 can easily be changed to fit the characteristics of any trapping level within the bandgap.

The procedure discussed in Sections (4.3.4) and (4.3.5) for determining mobility as a function of composition and doping requires

the following set of equations which represent curves fitted to available data (see Figures 5.1, 5.2 and 5.3).

Holes, data for GaAs used [37]:

$$\mu_{p2} = f_{p2}(N) = \frac{380\text{cm}^2/\text{V}\cdot\text{sec}}{[1+(3.17\text{x}10^{-17}\text{cm}^3)N]^{0.266}} \tag{5.2}$$

where N = total impurity density

Electrons, indirect valley, data for AlAs used [38]:

$$\mu_{n1} = f_{n1}(N) = \frac{165\text{cm}^2/\text{V}\cdot\text{sec}}{[1+(8.1\text{x}10^{-17}\text{cm}^3)N]^{0.13}} \tag{5.3}$$

Electrons, direct valley, data for GaAs used [37]:

$$\mu_{n2} = f_{n2}(N) = \frac{7200\text{cm}^2/\text{V}\cdot\text{sec}}{[1+(5.51\text{x}10^{-17}\text{cm}^3)N]^{0.233}} \tag{5.4}$$

By curve fitting experimental data [31,33,34], the following equations were used to estimate the diffusion lengths of electrons and holes:

$$L_n \simeq \frac{8\mu M}{1+N(8\text{x}10^{-19}/\text{cm}^3)} \tag{5.5}$$

$$L_p \simeq \frac{3\mu M}{1+N(1.2\text{x}10^{-18}/\text{cm}^3)} \tag{5.6}$$

where N = total doping density. Then, by using Equations (5.2) and (5.4) to calculate the mobilities, the lifetimes required by the Shockley-Read-Hall model were estimated to be:

$$\tau_{no} = \frac{L_n^2}{\frac{kT}{q}\mu_n} = 5.3 \text{ nsec}$$

$$\tau_{po} = \frac{L_p^2}{\frac{kT}{q}c\mu_p} = 8.5 \text{ nsec}$$

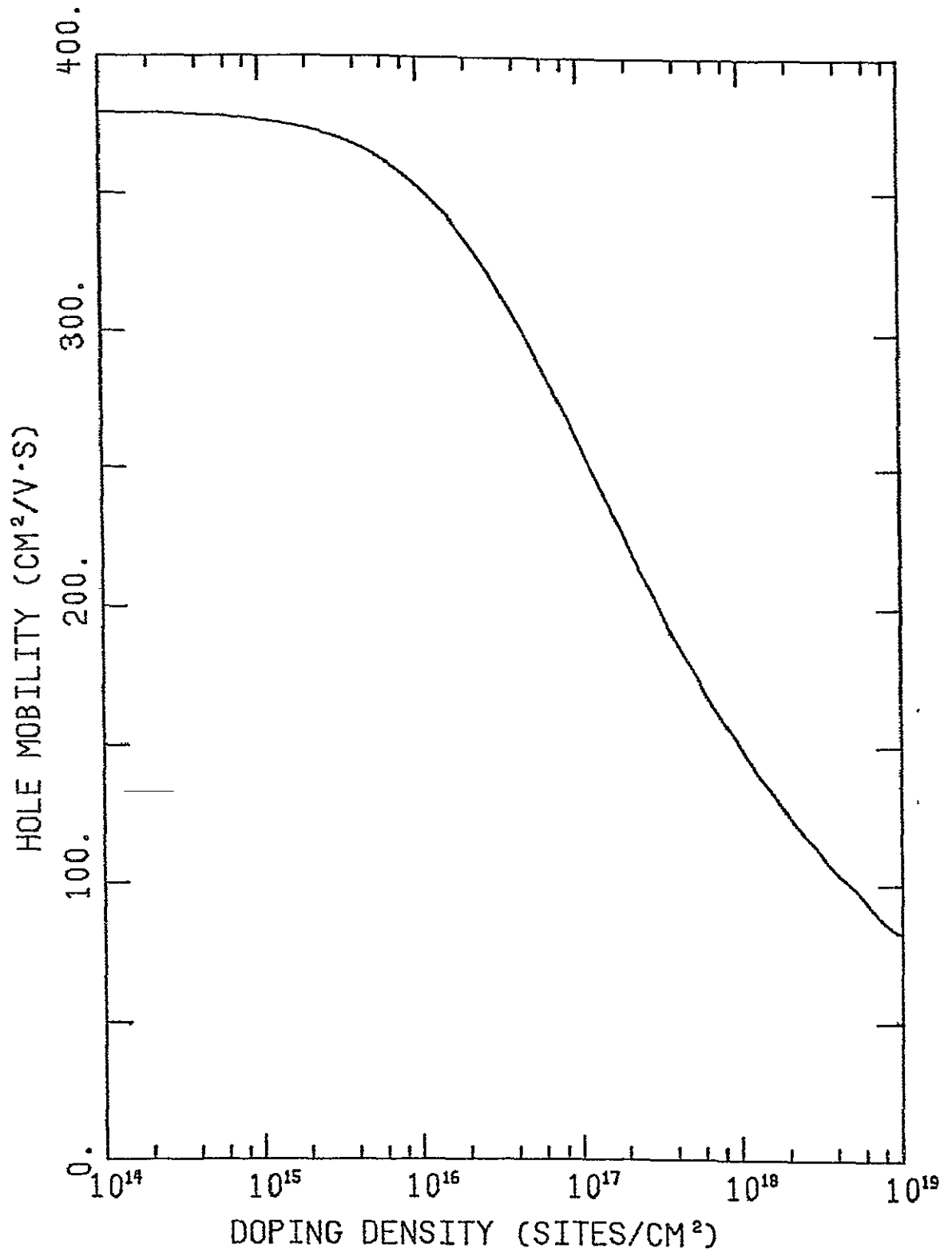

Figure 5.1 Empirical relationship between hole mobility and doping in GaAs as given by Equation (5.2).

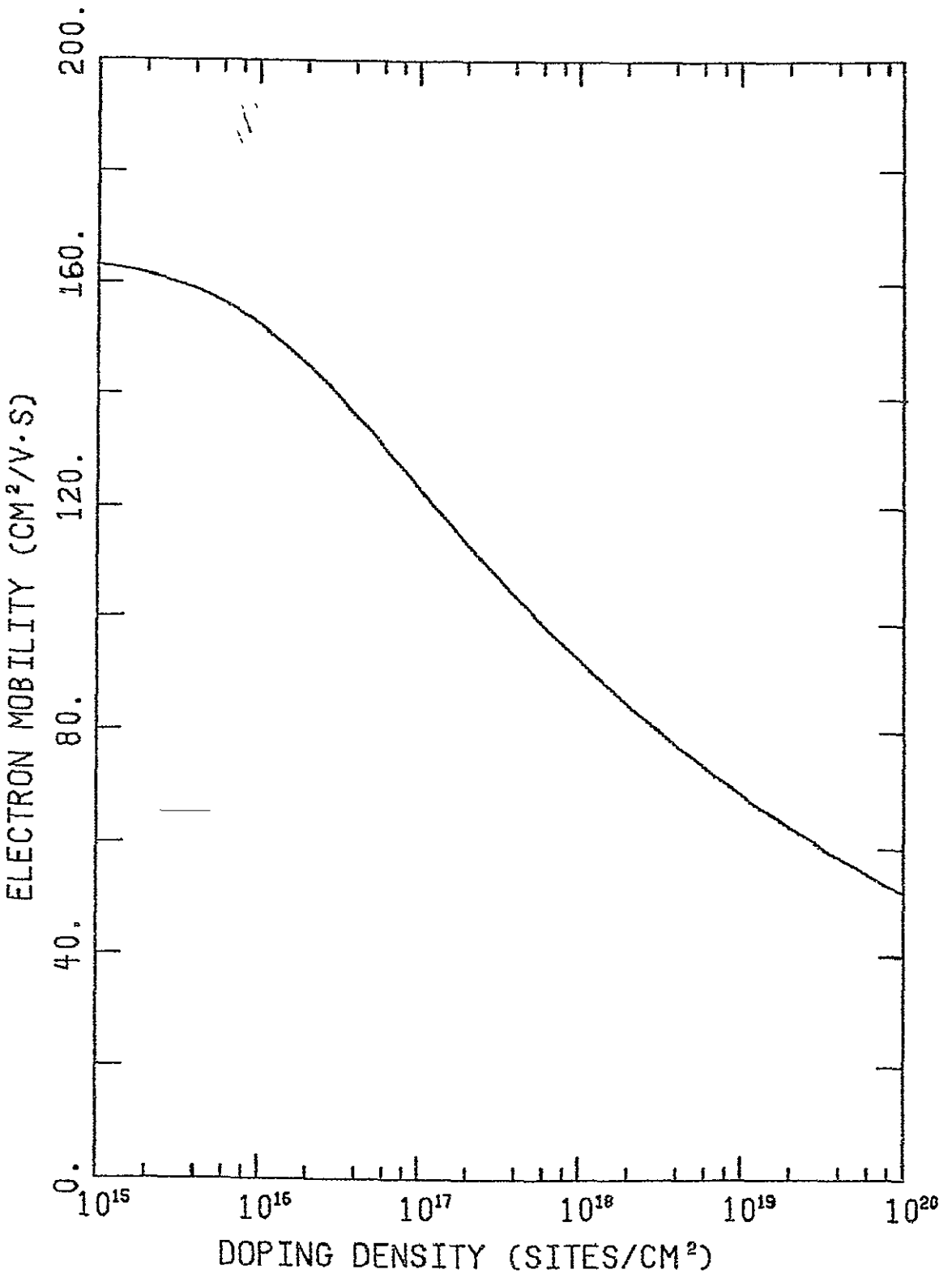

Figure 5.2 Empirical relationship between electron mobility and doping in AlAs as given by Equation (5.3).

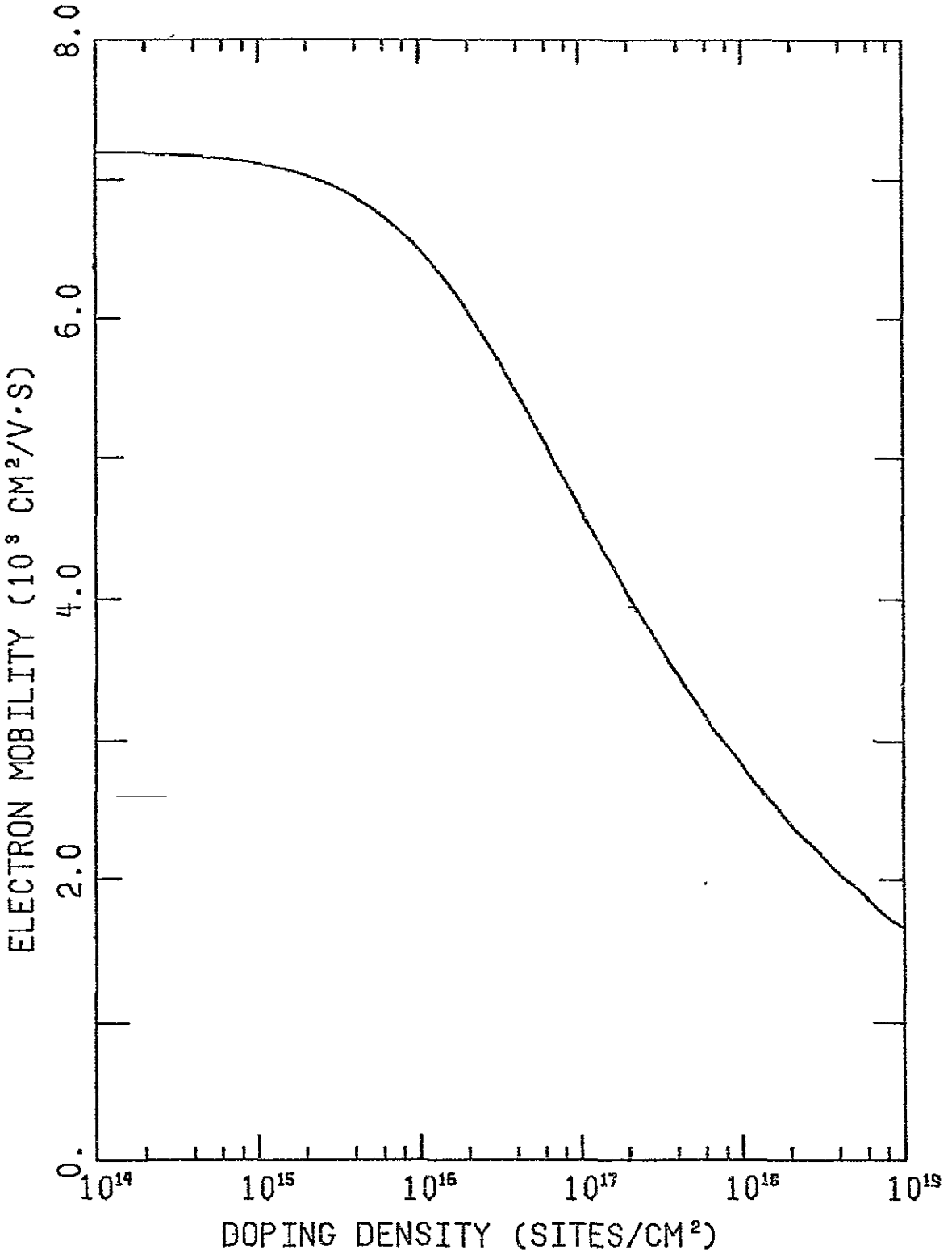

Figure 5.3 Empirical relationship between electron mobility and doping in GaAs as given by Equation (5.4).

when the total doping concentration was $4x10^{17}/cm^3$ in the top n-type layer and $2x10^{17}/cm^3$ in the p-type base.

The values used for the direct and indirect bandgaps of the two binary semiconductors were:

AlAs: direct gap = E_{gd1} = 2.95eV [39]

indirect gap = E_{gi1} = 2.16eV [40]

absolute gap = $E_{g1} = E_{gi1}$ = 2.16 eV

GaAs: direct gap = E_{gd2} = 1.439eV [41]

indirect gap = E_{gi2} = 1.87eV [41]

absolute gap = $E_{g2} = E_{gd2}$ = 1.439eV

The direct gap for the ternary alloy was calculated as a function of composition by [41]:

$$E_{gd}(C) = 0.468C^2 + 1.042C + 1.439 \qquad (5.7)$$

where C = mole fraction of AlAs.

The indirect gap for the alloy was approximated linearly as

$$E_{gi}(C) = 1.87 + 0.29C \qquad (5.8)$$

It is apparent from the bandgap vs. composition curves of Figure 5.4 that the direct-indirect transition occurs at about 44% AlAs, in approximate agreement with the transition point determined experimentally by others [42]. As discussed in Section 4.3.6 the electron affinity is assumed to depend on bandgap through a proportionality constant K_a. The values used for K_a and for the electron affinity in the two binary semiconductors were [26,35]:

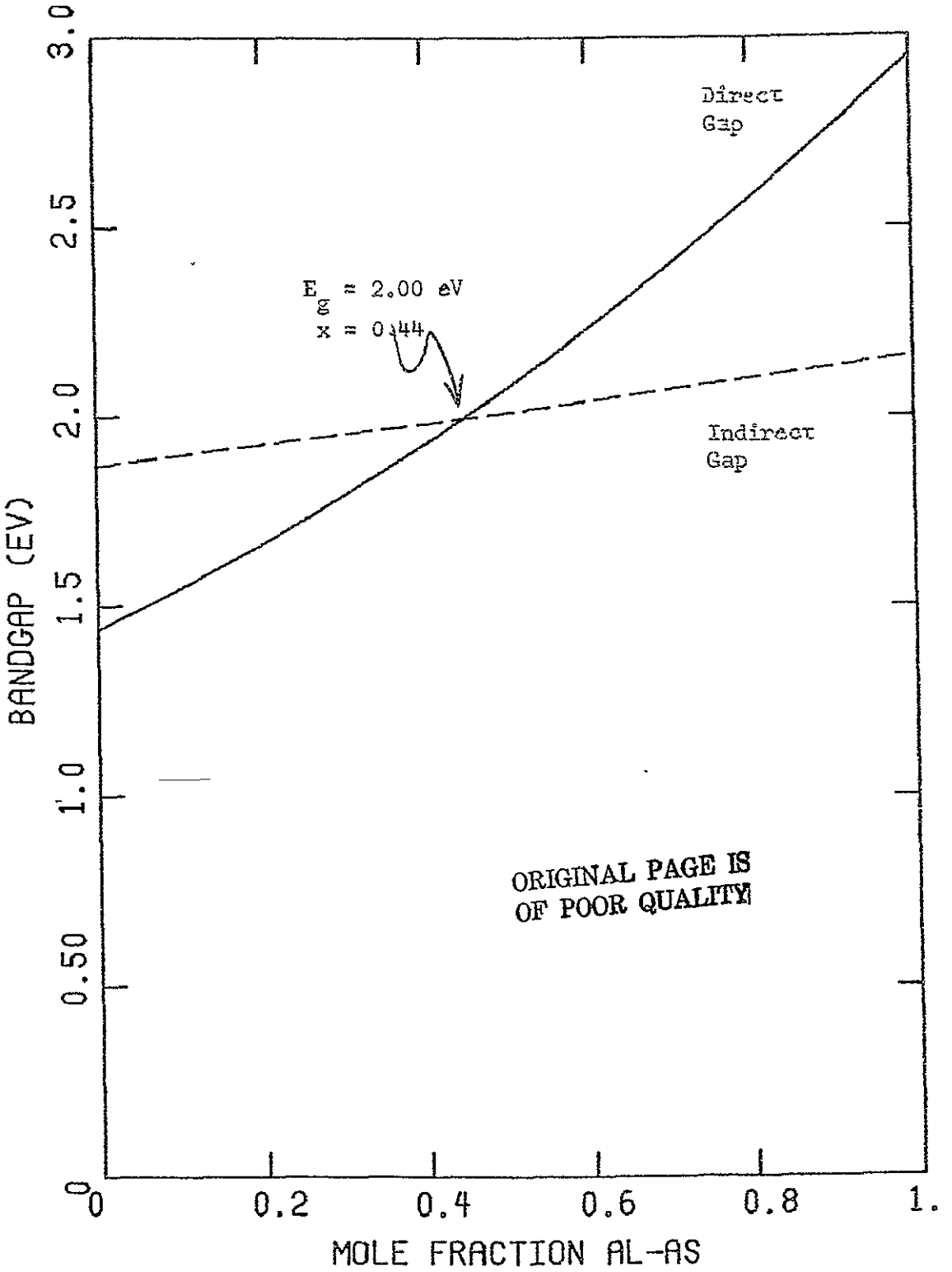

Figure 5.4 Bandgap of $Al_xGa_{1-x}As$ as a function of composition [39,40,41].

$$K_a = 0.85$$

AlAs: $\chi_{c1} = 3.57$ eV

GaAs: $\chi_{c2} = 4.07$ eV

Specifically, these values give electron affinity as a function of bandgap and thus composition by Equations (5.7) and (5.8), as

$$\chi_c = 4.07 - 0.85(E_{gd} - E_{g2}) + E_{gd} - E_g \qquad (5.9)$$

The values for the lattice constants required for determining interface state density as discussed in Section (4.4) are [29]

AlAs: $a_1 = 5.661\text{Å}$

GaAs: $a_2 = 5.654\text{Å}$

Surface recombination velocities at the two ends of the semiconductor crystal were chosen to be

back surface: $S = \infty$cm/sec

front surface: $S = 10^5$cm/sec

(except for one computer run discussed in Chapter 6).

The optical carrier generation rate G_e was calculated in the manner described in Section 4.5 . Figure 5.5 shows the results of the interpolation procedure described in that section for determining the absorption coefficient as a function of both composition and photon energy (or wavelength). A similar procedure was used to estimate the refractive index vs. wavelength profile for an arbitrary alloy composition at the semiconductor - SiO interface. Briefly, the refractive index curve for GaAs was written as a function of photon energy, and then shifted by the difference between the ternary alloy bandgap and the bandgap of GaAs. The resulting curve for AlAs can be compared with the original

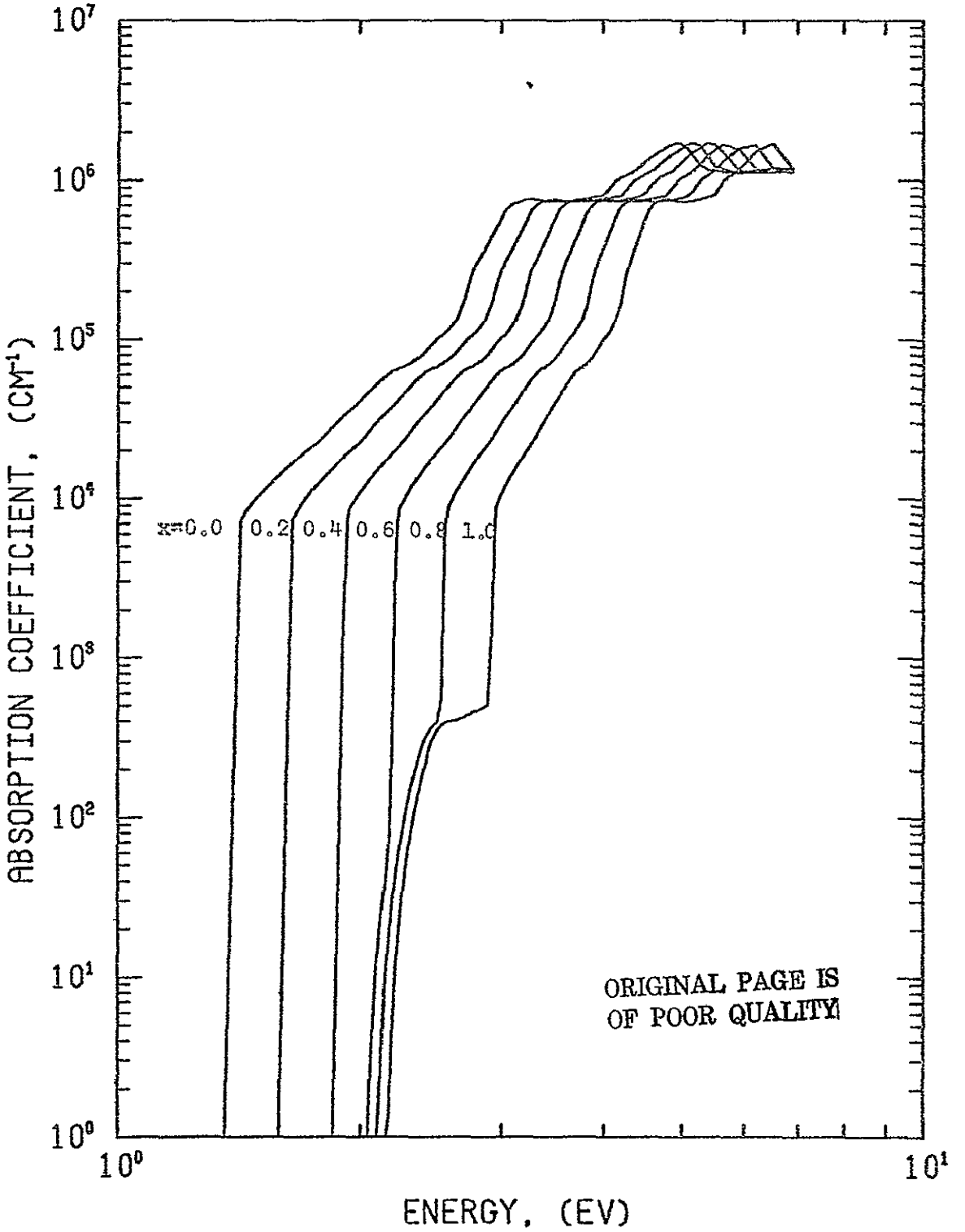

Figure 5.5 Absorption coefficient vs. energy for $Al_xGa_{1-x}As$ with six values of x, mole fraction of AlAs, interpolated from data on GaAs [51], and AlAs [2].

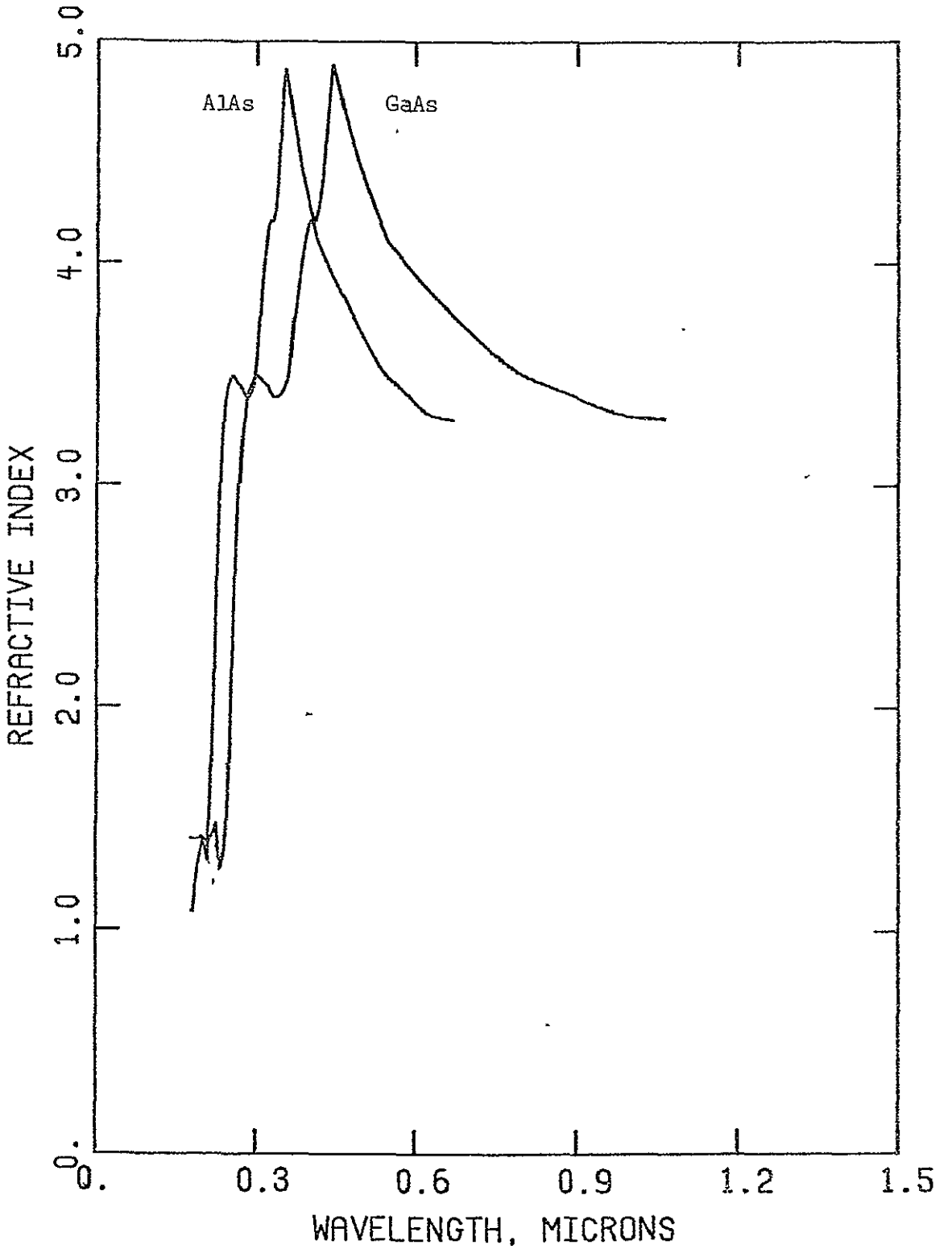

Figure 5.6 Refractive index for GaAs [37] and estimated refractive index for AlAs.

curve for GaAs in Figure 5.6. This estimation procedure can be improved when data concerning the refractive index of AlAs or $Al_xGa_{1-x}As$ becomes available.

All computer runs made as of the time of this writing have used the AMO solar irradiance data shown in Figure 2.2. By running the independent generation rate program with a range of SiO antireflection layer thicknesses, it was determined that maximum excess carrier generation occurs at a layer thickness of 0.07μM (±0.01μM) regardless of composition profile.

The results of the computer analysis of $Al_xGa_{1-x}As$ solar cells will be presented in Chapter 6.

5.3 Material Properties of $GaAs_{1-x}P_x$

A second interesting semiconductor alloy for solar cell applications is $GaAs_{1-x}P_x$ which, in many respects, resembles $Al_xGa_{1-x}As$. GaP, like AlAs is an indirect material having a bandgap considerably larger (2.262eV) than that of GaAs. Since the band structures of GaP and AlAs are similar, it is not surprising that their optical properties also resemble each other. Since GaP has a slightly larger absolute bandgap than AlAs, it might be expected that GaP would make a better window layer by absorbing a smaller fraction of the solar spectrum. However, it will be seen that the direct bandgap of GaP is considerably smaller than that of AlAs so that higher energy photons are absorbed at a greater rate than in AlAs. Given the spectral distribution of sunlight under AMO conditions the ultimate effect is greater attenuation in a GaP window than in an AlAs window of the same thickness. This fact will be shown

clearly by the profile for the generation rate near the front of the cells discussed in Chapter 6.

Probably the most serious problems inherent in $GaAs_{1-x}P_x$ solar cells are associated with the fact that the lattice mismatch between GaP and GaAs (about 4%) is considerably greater than that of AlAs and GaAs [29]. This can be expected to lead to much more severe recombination losses at any GaP-GaAs heterojunction present in such a device. However since one purpose of this research is to clarify the importance of interface recombination to solar cell performance, this relatively poor lattice match makes $GaAs_{1-x}P_x$ an interesting material for computer analysis.

Although experimental data for the properties of $GaAs_{1-x}P_x$ are not as readily available as data for $Al_xGa_{1-x}As$, enough information has been found to satisfy the requirements of the computer simulation program. In the following data, the subscript 1 refers to GaP, while the subscript 2 refers to GaAs. Unless otherwise stated, the material properties pertaining to GaAs are the same as those used in the analysis of $Al_xGa_{1-x}As$ listed in the previous section.

The two relative dielectric constants for GaP were assigned values of [43]:

$$\text{low frequency:} \quad \varepsilon_{\ell 1} = 11.1$$

$$\text{high frequency:} \quad \varepsilon_{h1} = 9.11$$

The carrier effective masses for GaP in terms of electron rest mass m_o are:

holes: $m^*_{p1} = 0.772m_o$ [44]

electrons, direct valley: $m^*_{cd1} = 0.114m_o$ [44]

indirect valley: $m^*_{ci1} = (0.34)(3)^{2/3}m_o$ [45]

Once again, all computer runs were made for a temperature of 300°K and the Shockley-Read-Hall recombination parameters were given by Equation (5.1) for all composition values. The lifetimes used in the S-R-H model were once again:

$$\tau_{no} = 5.3\text{nsec},$$

$$\tau_{po} = 8.5\text{nsec}.$$

The doping dependence of mobility for electrons in the indirect valley used an empirical equation fitted to data for electrons in GaP [38]:

$$\mu_{n1} = f_{n1}(N) = \frac{200\text{cm}^2/\text{V}\cdot\text{sec}}{[1+(1.5\text{x}10^{-18}\text{cm}^3)N]^{0.244}}, \qquad (5.10)$$

where, as before, N = total impurity density. The above equation is plotted for reference in Figure 5.7.

The values for the direct and indirect bandgaps of GaP and GaAs were taken to be

GaP: direct gap = $E_{gd1} = 2.783\text{eV}$ [46]

indirect gap = $E_{gi1} = 2.262\text{eV}$ [47]

absolute gap = $E_{g1} = E_{gi1} = 2.262\text{eV}$

GaAs: direct gap = $E_{gd2} = 1.425\text{eV}$ [46]

indirect gap = $E_{gi2} = 1.907\text{eV}$ [47]

absolute gap = $E_{g2} = E_{gd2} = 1.425\text{eV}$.

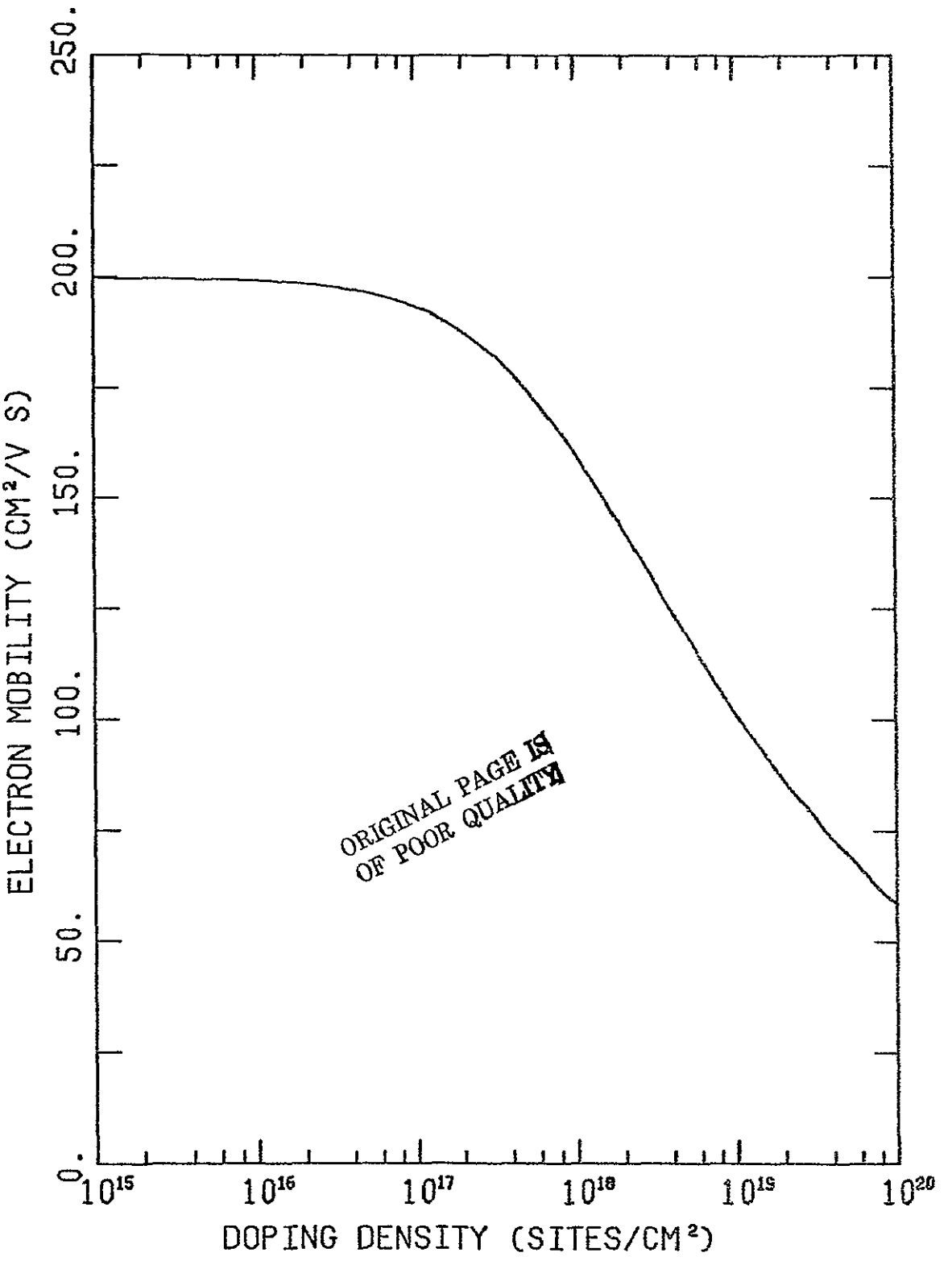

Figure 5.7 Empirical relationship between electron mobility and doping in GaP as given by Equation (5.10).

The corresponding direct and indirect gaps for $GaAs_{1-x}P_x$ were calculated by

$$E_{gd}(C) = 1.425 + 1.148C + 0.21C^2 \quad [46] \tag{5.11}$$

$$E_{gi}(C) = 1.907 + 0.144C + 0.211C^2 \quad [47]. \tag{5.12}$$

These curves are plotted in Figure 5.8 which shows that the direct-indirect transition occurs at about 48% GaP.

The parameters pertaining to electron affinity as discussed in Section 4.3.6 were:

$$K_a = 0.384$$

$$\text{GaP: } \chi_{c1} = 4.07\text{eV} \quad [35]$$

$$\text{GaAs: } \chi_{c2} = 4.07\text{eV}. \quad [35]$$

Although the electron affinities for the two binary semiconductors are virtually the same, the composition dependence of bandgap for the ternary alloy means that electron affinity cannot be taken as constant. From the discussion in Section 4.3.6 the dependence of electron affinity on bandgap can be written explicitly as

$$\chi_c = 4.07 - 0.384(E_{gd}-E_{g2}) + E_{gd}-E_g. \tag{5.13}$$

The lattice constant for GaP was taken as [29]

$$a_1 = 5.451\text{Å}.$$

Once again the surface recombination velocities were specified as:

back surface: $S = \infty$cm/sec,

front surface: $S = 10^5$cm/sec (except for one run discussed in Chapter 6).

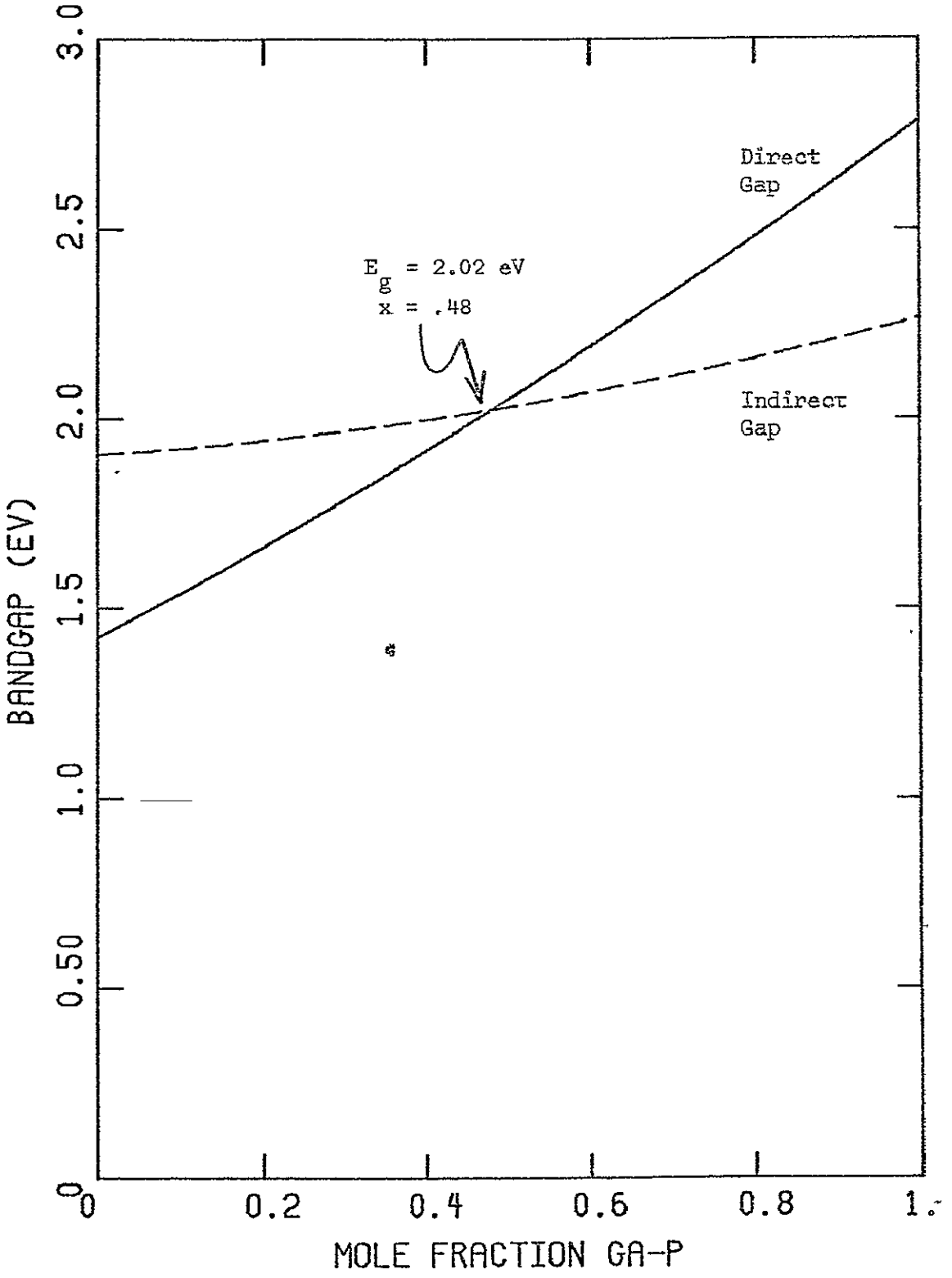

Figure 5.8 Bandgap of $GaAs_{1-x}P_x$ as a function of composition [46,47].

Finally, the optical generation rate for $GaAs_{1-x}P_x$ was determined using the same absorption coefficient and refractive index interpolation procedures used for $Al_xGa_{1-x}As$. The wavelength and composition dependence of absorption coefficient and refractive index produced by these techniques can be seen in Figures (5.9) and (5.10). Once again, AM0 solar irradiance conditions were specified for all runs and an optimum SiO antireflection layer thickness of 0.07 μM was used. The computer predictions concerning the performance of $GaAs_{1-x}P_x$ solar cells will be discussed in the next chapter.

5.4 Material Properties of $In_xGa_{1-x}As$

Among the problems considered in this research is the determination of the relationship between substrate bandgap and solar cell efficiency. Although initial computer simulations for this purpose examined the performance of cells having substrates made of either GaAs, $Al_xGa_{1-x}As$ or $GaAs_{1-x}P_x$, these materials have bandgaps greater than or equal to that of GaAs which is about 1.44 eV. In order to study the effects of smaller bandgaps, cells having substrates made of $In_xGa_{1-x}As$ were subsequently analyzed. Unlike $Al_xGa_{1-x}As$ and $GaAs_{1-x}P_x$, $In_xGa_{1-x}As$ is a direct material for all values of x. The high absorption rate resulting from these properties is well suited to a substrate, but not to a window layer. For this reason, the cells analyzed in this work having $In_xGa_{1-x}As$ substrates have used AlAs windows.

One of the most crucial parameters to be remembered during the interpretation of the computer simulation of AlAs-on-$In_xGa_{1-x}As$ solar cells is the lattice mismatch (about 7%) between InAs and both GaAs

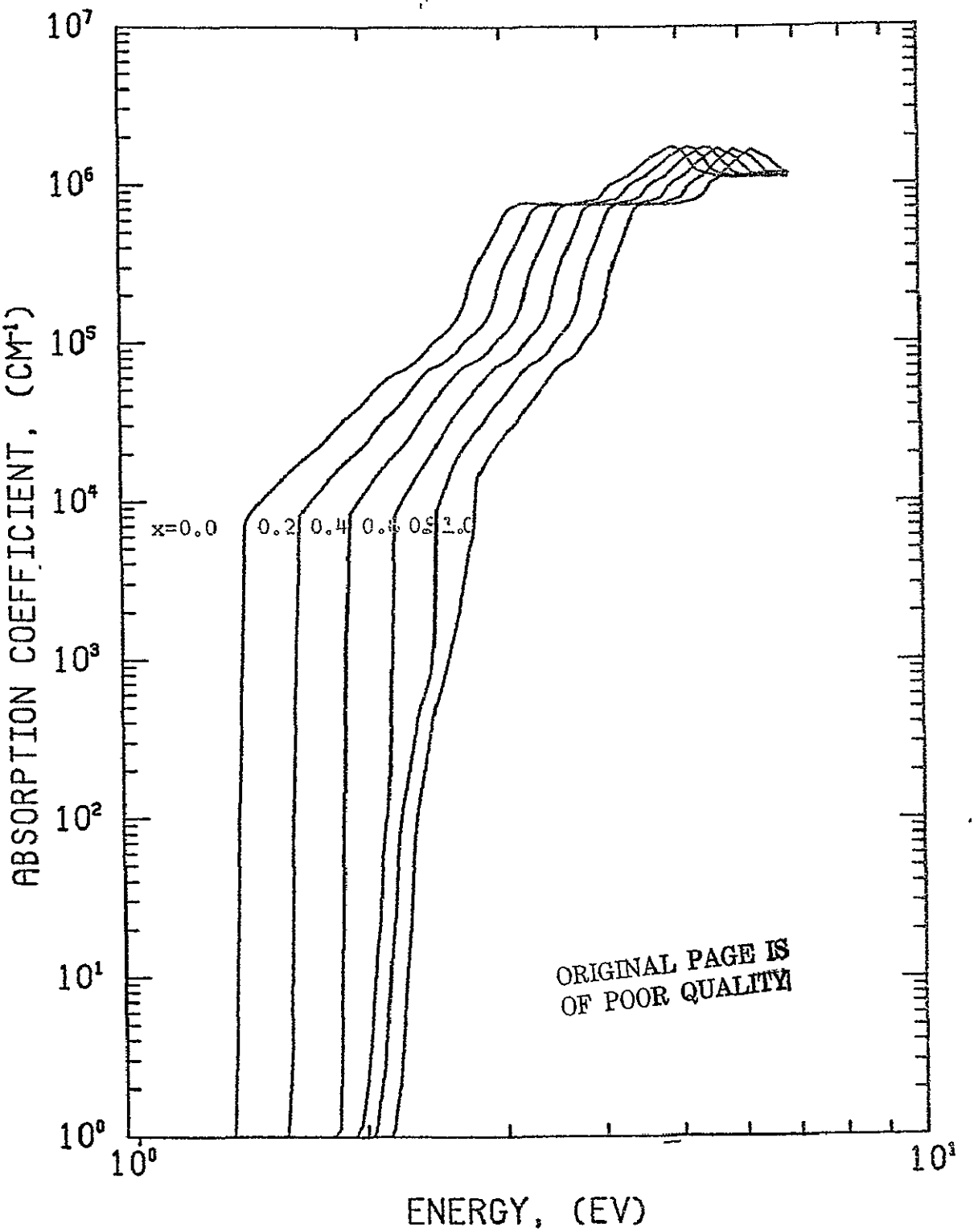

Figure 5.9 Absorption coefficient vs. energy for $GaAs_{1-x}P_x$ for six values of x, mole fraction of GaP. Interpolated from data on GaAs [51], and GaP [52,53].

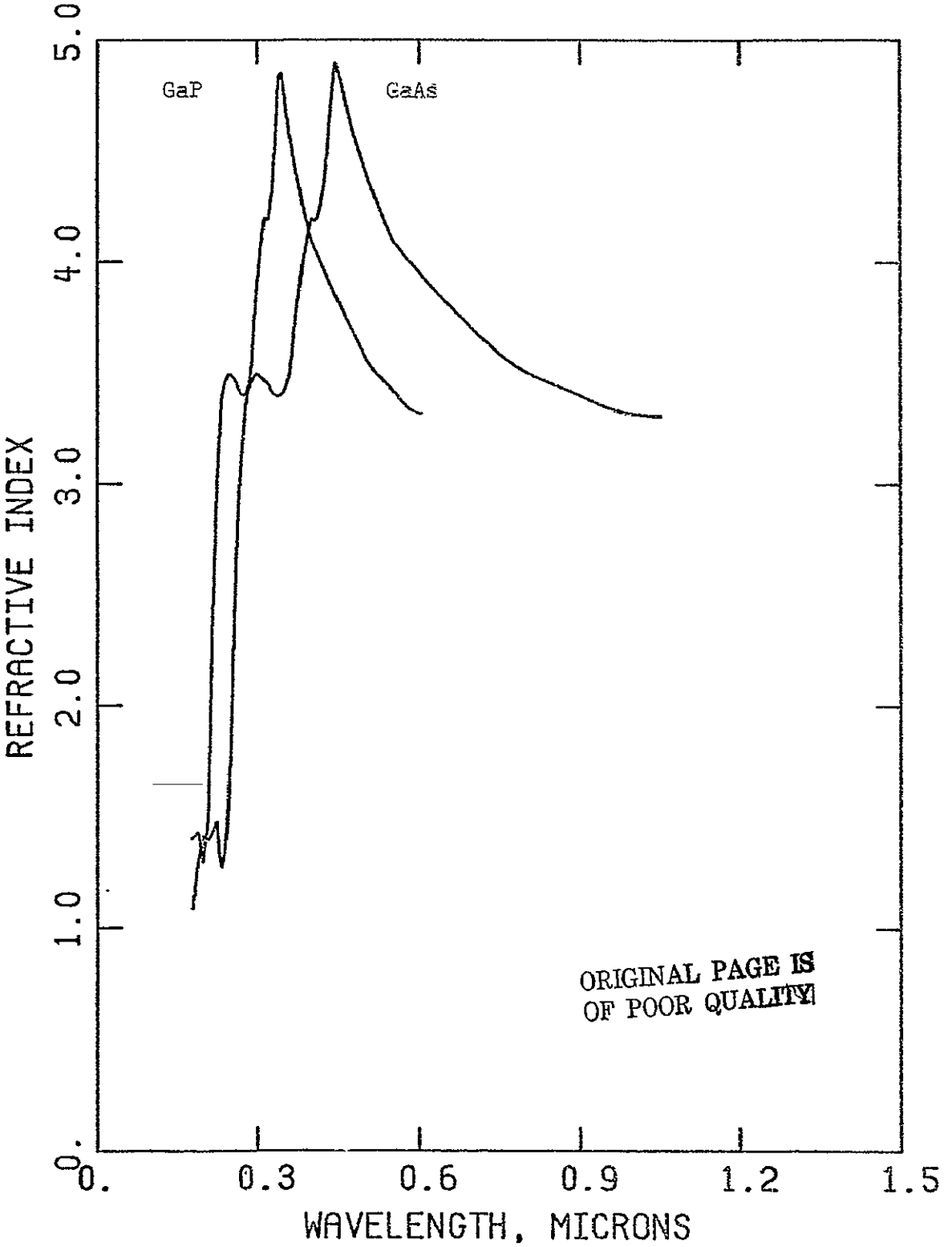

Figure 5.10 Refractive index for GaAs [87] and estimated refractive index for GaP.

and AlAs, which can be expected to produce significant recombination losses due to lattice mismatch in variable composition layers. The effects of bandgap changes and interface states introduced by alloying InAs with GaAs beneath an AlAs window will be discussed in the next chapter.

Consistent with the notation established earlier, the subscript 1 in the following data refers to InAs while the subscript 2 refers to GaAs. If not otherwise specified the parameters for GaAs are the same as those given in Section 5.2.

The two relative dielectric constants for InAs were [35]:

$$\text{low frequency:} \quad \varepsilon_{\ell 1} = 14.55,$$

$$\text{high frequency:} \quad \varepsilon_{h1} = 11.8.$$

The carrier effective masses for InAs were assigned values of:

$$\text{holes:} \quad m^*_{p1} = 0.41\, m_o \qquad [35],$$

$$\text{electrons, direct valley:} \quad m^*_{cd1} = 0.024\, m_o [35],$$

$$\text{indirect valley:} \quad m^*_{ci1} = (0.39)(3)^{2/3} m_o.$$

The effective mass for indirect valley electrons in InAs was set equal to that in GaAs for lack of further data and because $In_xGa_{1-x}As$ is entirely a direct material so that indirect valley electrons do not significnatly contribute to carrier activity. For the same reason, the doping dependence of mobility for indirect valley electrons was calculated from the empirical relationship used for such electrons in AlAs as given by Equation (5.3). As for other materials analyzed in this work, the Shockley-Read-Hall recombination parameters were given by Equation (5.1) and the lifetimes were specified as:

$$\tau_{no} = 5.3 \text{ nsec},$$

$$\tau_{po} = 8.5 \text{ nsec}.$$

The values for the bandgaps of InAs are:

$$\text{direct gap} = E_{gd1} = 0.359 \text{ eV} \quad [35],$$

$$\text{indirect gap} = E_{gi1} = 1.60 \text{ eV} \quad [7],$$

$$\text{absolute gap} = E_{g1} = E_{gd1} = 0.359 \text{ eV},$$

and the corresponding equations for the direct and indirect bandgaps of $In_xGa_{1-x}As$ are (see Figure 5.11):

$$E_{gd}(C) = 1.439 - 1.41C + 0.33C^2 \quad [7,35,41] \tag{5.14}$$

$$E_{gi}(C) = 1.87 - 0.27C \tag{5.15}$$

The parameters used to determine electron affinity as discussed in Section 4.3.6 are:

$$K_a = 0.77$$

$$\text{InAs: } \chi_{c1} = 4.90 \text{ eV } [35],$$

so that electron affinity was calculated from the bandgap as:

$$\chi_c = 4.07 - 0.384(E_{gd} - E_{g2}). \tag{5.16}$$

The lattice constant for InAs is

$$a_1 = 6.058 \text{ Å } [29].$$

Once again the optical generation rate for $In_xGa_{1-x}As$ was calculated by the same interpolation procedure discussed at the end of Section 5.2.

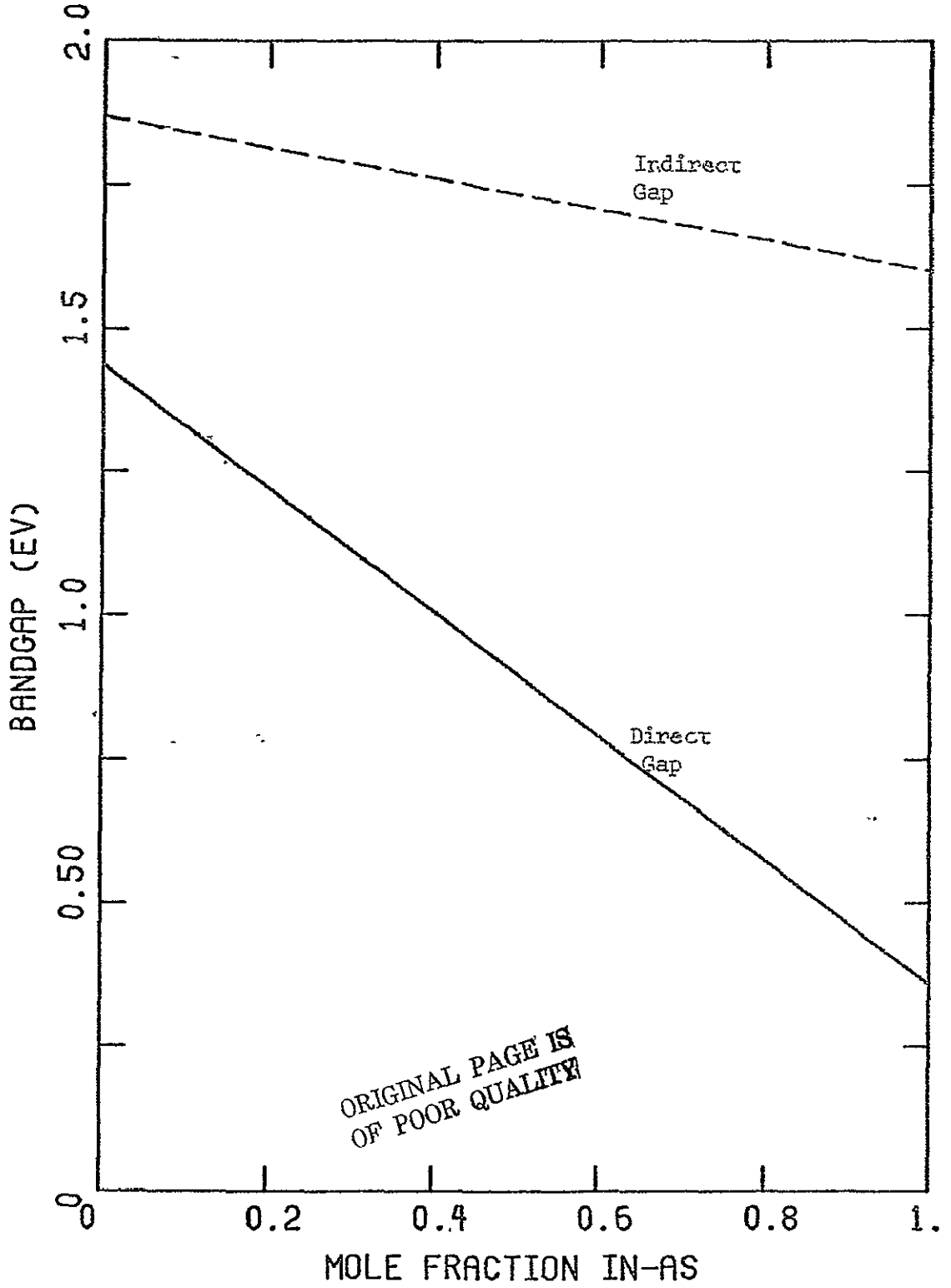

Figure 5.11 Bandgap of $In_xGa_{1-x}As$ as a function of composition.

6. COMPUTER ANALYSIS RESULTS

6.1 Introduction

The computer analysis program has been designed to allow for the specification of a wide variety of variable composition solar cell structures. Device polarity can be either n-on-p or p-on-n with either an abrupt or a Gaussian doping profile. Doping levels can be arbitrarily specified, and, if desired, a heavily doped layer can be placed at the back contact to create a high-low junction for improved carrier collection and reduced dark current (see Reference [19]). The composition profile can be arbitrarily defined by providing the position dependence of the relative concentrations of two binary semiconductors in a ternary alloy. Dark characteristics are obtained by selecting an optical generation rate of zero, and characteristics in light can be found for either AM0 or AM2 illumination conditions. Finally, an antireflection layer made of SiO can be assigned any reasonable thickness.

The simulation results discussed in this chapter include $Al_xGa_{1-x}As$, $In_xGa_{1-x}As$ and $GaAs_{1-x}P_x$ cells where the composition is either linearly graded or abruptly changed at a heterojunction and is constant in the bulk beneath the window layer. All cells analyzed up to the present time have used an 0.07 μM (near optimum) SiO antireflection layer and have been illuminated under AM0 conditions. The structure and key performance parameters for twenty-nine of the more interesting devices can be found in Figure 6.1 and Tables 6.1 and 6.2.

The first device shown in Table 6.1 is an n-on-p GaAs solar cell with no composition variation. The data obtained for this "control"

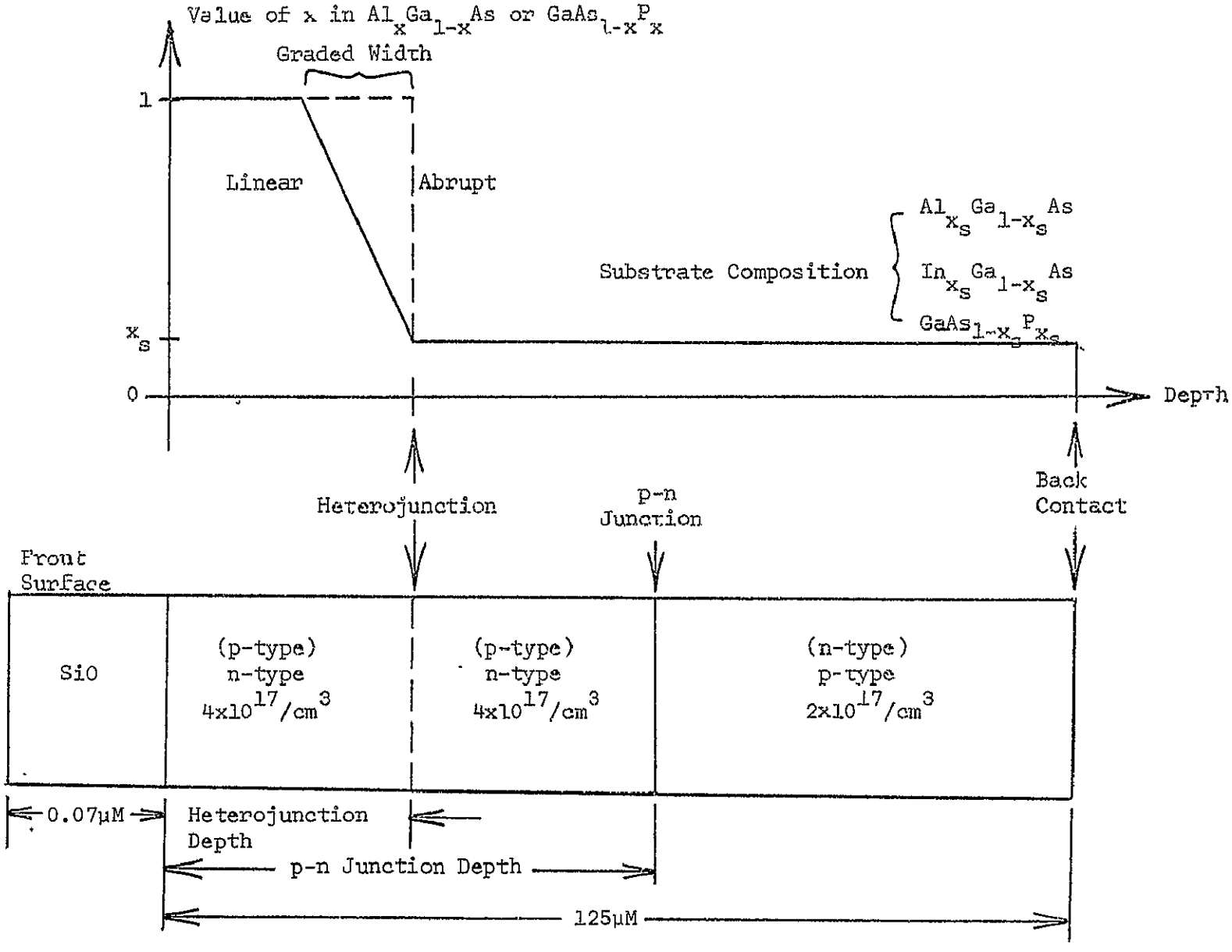

Figure 6.1 Structure common to all devices in Tables 6.1 and 6.2.

Table 6.1 Structure parameters and computer analysis results for several $(Al,In)_xGa_{1-x}As$ solar cells (see Fig. 6.1), under AMO irradiation.

Device #	Alloy	Comp. Change	Het. Depth (μM)	Mole Frac. GaAs, Bulk	p-n Depth (μM)	Polarity	S cm/sec	Inter-face States	V_{oc} (V)	J_{sc} (mA/cm^2)	Fill Factor	Peak Eff. (%)
1	GaAs	none	-	1.00	1.0	n-on-p	10^5	-	.964	17.8	.822	10.42
2	$Al_xGa_{1-x}As$	linear (to 35% AlAs)	1.0	1.00	1.0	n-on-p	10^5	No	.999	32.1	.864	20.46
3	$Al_xGa_{1-x}As$	linear	1.0	1.00	1.0	n-on-p	10^5	No	.999	32.6	.863	20.75
4	$Al_xGa_{1-x}As$	linear	1.0	1.00	1.5	n-on-p	10^5	No	.998	32.4	.863	20.60
5	$Al_xGa_{1-x}As$	abrupt	1.0	1.00	1.0	n-on-p	10^5	No	.998	31.4	.861	19.95
6	$Al_xGa_{1-x}As$	abrupt	1.0	1.00	1.0	n-on-p	10^5	Yes	.991	31.4	.862	19.85
7	$Al_xGa_{1-x}As$	abrupt	1.0	1.00	1.3	n-on-p	10^5	Yes	.998	31.8	.862	20.21
8	$Al_xGa_{1-x}As$	abrupt	0.5	1.00	0.8	n-on-p	10^5	Yes	.999	32.3	.863	20.55
9	$Al_xGa_{1-x}As$	abrupt	0.1	1.00	0.4	n-on-p	10^5	Yes	.999	32.8	.867	20.95
10	$Al_xGa_{1-x}As$	abrupt	0.1	1.00	0.4	n-on-p	10^6	Yes	.999	32.8	.863	20.86
11	$Al_xGa_{1-x}As$	abrupt	0.1	0.95	0.4	n-on-p	10^5	Yes	1.050	31.0	.868	20.83
12	$Al_xGa_{1-x}As$	abrupt	0.1	0.90	0.4	n-on-p	10^5	Yes	1.103	29.1	.873	20.62
13	$AlAs/In_xGa_{1-x}As$	abrupt	0.1	0.99	0.4	n-on-p	10^5	Yes	.986	33.3	.864	20.94
14	$AlAs/In_xGa_{1-x}As$	abrupt	0.1	0.98	0.4	n-on-p	10^5	Yes	.973	33.7	.867	20.92
15	$AlAs/In_xGa_{1-x}As$	abrupt	0.1	0.95	0.4	n-on-p	10^5	Yes	.934	34.8	.865	20.83
16	$Al_xGa_{1-x}As$	abrupt	0.1	1.00	0.1	p-on-n	10^5	Yes	1.032	29.8	.850	19.27
17	$Al_xGa_{1-x}As$	abrupt	0.1	1.00	1.4	p-on-n	10^5	Yes	1.028	32.7	.857	21.23

Table 6.2 Structure parameters and computer analysis results for several $GaAs_{1-x}P_x$ solar cells (see Fig. 6.1), under AMO irradiation.

Device #	Alloy	Comp. Change	Graded Width (Å)	Het. Depth (μM)	Mole Frac. GaAs, Bulk	p-n Depth (μM)	S cm/sec	Inter-face States	V_{oc} (V)	J_{sc} (mA/cm^2)	Fill Factor	Peak Eff. (%)
18	$GaAs_{1-x}P_x$	abrupt	-	1.0	1.00	1.0	10^5	No	.985	30.64	.862	19.24
19	$GaAs_{1-x}P_x$	abrupt	-	1.0	1.00	1.0	10^5	Yes	.831	30.64	.799	15.04
20	$GaAs_{1-x}P_x$	abrupt	-	1.0	1.00	1.04	10^5	Yes	.974	30.59	.859	18.92
21	$GaAs_{1-x}P_x$	abrupt	-	.5	1.00	.54	10^5	Yes	.975	31.48	.859	19.49
22	$GaAs_{1-x}P_x$	abrupt	-	.1	1.00	.14	10^5	Yes	.976	32.43	.859	20.10
23	$GaAs_{1-x}P_x$	abrupt	-	.1	1.00	.14	10^6	Yes	.961	32.19	.857	19.56
24	$GaAs_{1-x}P_x$	abrupt	-	.1	0.95	.14	10^5	Yes	1.007	30.28	.870	19.39
25	$GaAs_{1-x}P_x$	abrupt	-	.1	0.90	.14	10^5	Yes	1.052	28.28	.870	18.91
26	$GaAs_{1-x}P_x$	linear	50.0	.1	1.00	.14	10^5	Yes	.971	32.34	.866	20.21
27	$GaAs_{1-x}P_x$	linear	200.0	.1	1.00	.14	10^5	Yes	.981	32.49	.865	20.40
28	$GaAs_{1-x}P_x$	linear	600.0	.1	1.00	.14	10^5	Yes	.983	32.51	.864	20.43
29	$GaAs_{1-x}P_x$	linear	1000.0	.1	1.00	.14	10^5	Yes	.983	32.41	.864	20.37

cell can be used as a reference for comparison with the results of the simulation of variable composition devices. Devices 2-10 are $nAl_xGa_{1-x}As$-nGaAs-pGaAs with various p-n junction depths, window thicknesses and window composition profiles. The next five cells (11-15) have the same structure as device 9 except that the substrates are either $Al_xGa_{1-x}As$ (devices 11 and 12) or $In_xGa_{1-x}As$ (devices 13-15) rather than GaAs alone. The last two cells in Table 6.1 represent a sample of the structures analyzed to determine the possible advantages of the p-on-n polarity. Although most of the present research has dealt with abrupt heterojunction devices, three graded $Al_xGa_{1-x}As$ cells (devices 2-4) and four graded $GaAs_{1-x}P_x$ cells (devices 26-29) were simulated in order to estimate possible advantages of the built-in fields and broadened interface state distribution that accompany composition grading. As shown in the third column of Tables 6.1 and 6.2, the grading was linear and graded layers ranged in thickness from 50Å to 1 μM.

Window thicknesses between 0.1 μM and 1.0 μM were examined and numerous runs were made to determine the optimum placement of the p-n junction for several values of window thickness. Although the p-n junction depth below the heterojunction was allowed to vary between 0.0 μM and 2.0 μM, only the most significant configurations appear in the tables. In an effort to determine the relationship between peak efficiency and substrate composition, several runs were made with a fixed, non-zero mole fraction of either AlAs, InAs, or GaP in the bulk for comparison with similar structures having substrates made entirely of GaAs. The results of the four most significant of these runs appear in the tables for devices 11-15, 24, and 25.

Since the major reason for using a wide bandgap window layer is to eliminate large surface recombination losses, it was not expected that the value of surface recombination velocity S would significantly affect performance in devices having such a window and so S was generally assigned a value of 10^5cm/sec. However, in order to verify these expectations, two runs were made with a value of S = 10^6cm/sec. The resulting performance data, shown in the tables for devices 10 and 23, should be compared with devices 9 and 22, respectively, which differ from 10 and 23 only in surface recombination velocity. Finally, in order to measure the influence of interface states on performance, several cells were simulated (Devices 2-5 and 18) without allowance for interface recombination. The relationships indicated by the data in Tables 6.1 and 6.2 are discussed and illustrated in more detail in the following sections.

6.2 Interface States

One of the foremost criteria used in selecting a ternary alloy system for variable composition solar cell use is the difference in the lattice constants of the two binary constituents. As discussed in previous chapters, the closer the lattice match, the fewer the interface states at any heterojunction and the lower the density of dangling bonds in any graded layer created by spatially varying the alloy composition. The basic reason for using a wide bandgap window layer is to reduce carrier recombination losses at surface imperfections. If the interface between the wide gap window and the smaller gap substrate is characterized by a high interface recombination velocity due to severe

lattice mismatch, surface recombination losses may simply be replaced by comparable interface recombination losses.

The small lattice mismatch (about 0.14%) between AlAs and GaAs makes the $Al_xGa_{1-x}As$ system a prime candidate for heterojunction solar cell use. Interface recombination velocities on the order of 10^4cm/s have been reported [28] for abrupt AlAs-GaAs heterojunctions while reasonable values for the surface recombination velocity of GaAs solar cells generally range from 10^6cm/sec to 10^7cm/sec [31,32]. By using Equation (4.25) and taking the lattice constants of AlAs and GaAs as 5.661×10^{-8}cm and 5.654×10^{-8}cm, respectively [29], the density of dangling bonds at an AlAs-GaAs heterojunction with a [100] orientation can be estimated to be about $3.1\times10^{12}/cm^2$.

The more severe lattice mismatch (about 4%) between GaP and GaAs, on the other hand, means that the $GaAs_{1-x}P_x$ system can be expected to suffer more serious interface recombination losses than the $Al_xGa_{1-x}As$ system, especially in abrupt heterojunction structures. By calculations similar to those used for $Al_xGa_{1-x}As$, and taking the lattice constant of GaP as 5.451×10^{-8}cm, the surface density of interface states at a GaP-GaAs heterojunction should be about $9.5\times10^{13}/cm^2$, or about 30 times the density at an AlAs-GaAs heterojunction. If the capture coefficients (see Section 4.4) in $Al_xGa_{1-x}As$ and $GaAs_{1-x}P_x$ are similar, then an interface recombination velocity of about 5×10^5cm/sec can be expected at a GaP-GaAs heterojunction. Since such a value is comparable to surface recombination velocities found in GaAs cells, the prospects for building efficient $GaAs_{1-x}P_x$ solar cells would appear to be relatively poor.

However, computer analysis of such cells can be useful in several ways. First, it can aid in assessing the relative importance of interface states in controlling peak efficiency by permitting a comparison with similar analyses of cells made of alloy systems with better interface properties. Second, it can add to the body of evidence needed to determine whether the $GaAs_{1-x}P_x$ system is as poorly adapted to solar cell use as first order considerations seem to indicate. Finally, computer simulation can test the ability of such techniques as composition grading and separation of the p-n junction from the heterojunction in reducing interface recombination losses.

The effect of interface states on AlAs-GaAs heterojunction cells can be seen by comparing devices 5 and 6 which are identical except that the analysis of device 5 omitted the interface states. Clearly, the degradation of peak efficiency (19.95% vs. 19.85%) caused by interface recombination cannot be considered a major factor in controlling the performance of $Al_xGa_{1-x}As$ cells. The effect should be even less significant in graded composition cells, and in cells having the p-n junction placed slightly beneath the heterojunction. These considerations will be discussed in later sections of this chapter.

The effect of interface states on abrupt GaP-GaAs cells was, as expected, found to be much more pronounced. Device 18 represents a structure with both the heterojunction and the p-n junction placed 1 μM beneath the front surface of the crystal, but with no interface states. Device 19, on the other hand, shows the results of analyzing the same structure by including the modeling of interface recombination as discussed in Section 4.4. The reduction in peak efficiency from

19.25% to 15.04% results from the large increase in dark current caused by recombination of carriers within the depletion region. As Figure 6.2 shows, the introduction of interface states (device 19) increases dark current by more than two orders of magnitude when the heterojunction coincides with the p-n junction. As will be discussed in the next section, this increase in dark current can be significantly reduced by placement of the p-n junction slightly below the heterojunction.

The effect of an increase in dark current is a greater loss in maximum power delivered to any external load as more internal forward bias current flows for any given terminal voltage. The softening of the knee of the J-V characteristics reduces the curve factor (from 0.862 to 0.799 in devices 18 and 19, respectively). In addition, the increased dark current reduces the open circuit voltage, which can be defined as the voltage at which internal bias current equals the current collected from optically generated carriers.

It is clear that interface recombination can seriously degrade the performance of heterojunction cells made of semiconductor materials that would otherwise be well suited to solar cell use. The next two sections discuss structure modifications that can help minimize the losses associated with interface states.

6.3 Optimization of p-n Junction Placement

The determination of the best location for the p-n junction in a solar cell is not a simple problem, especially for variable composition structures. Of course the p-n junction should be placed where the built-in field around it can most effectively collect optically generated

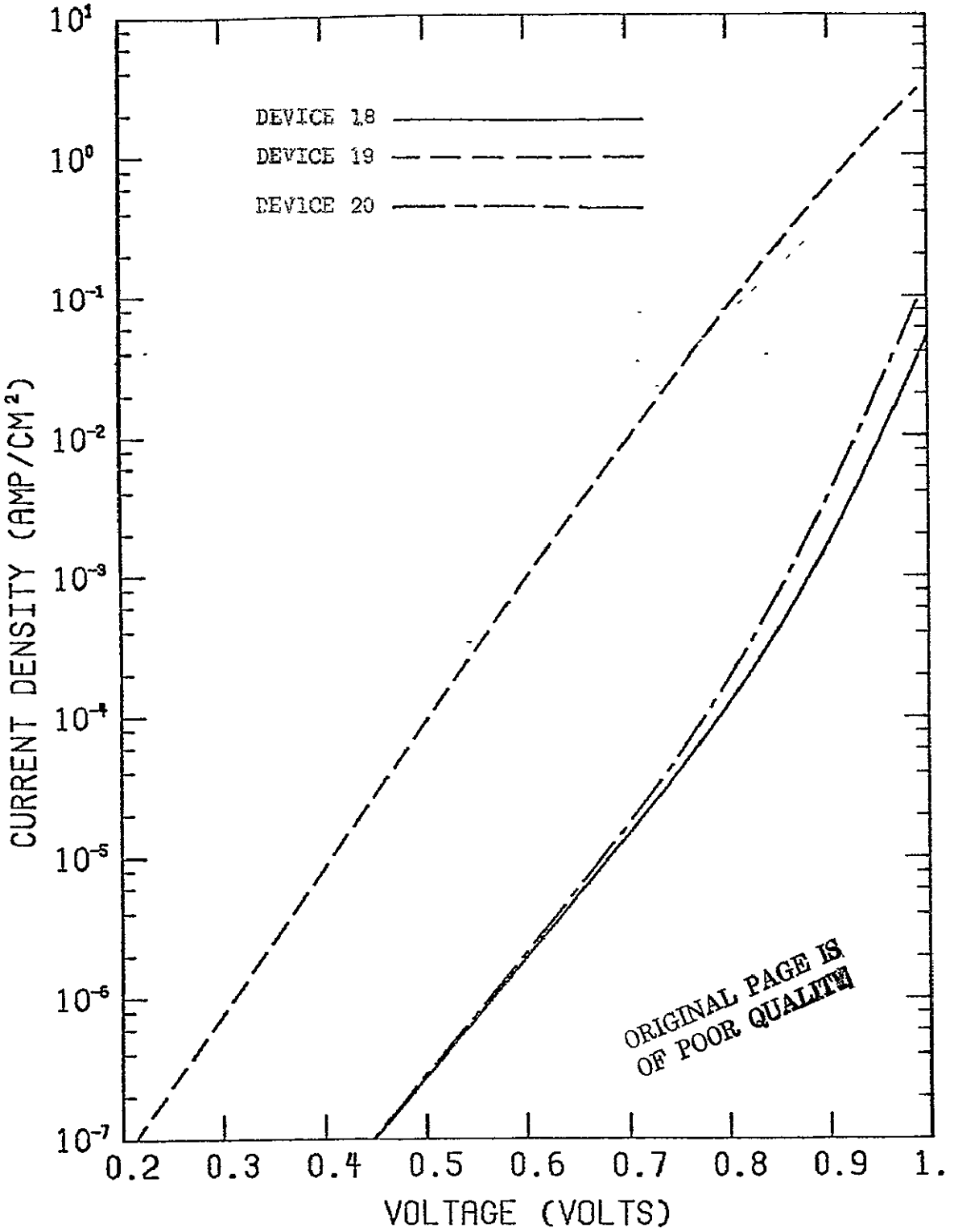

Figure 6.2 Dark current density vs. voltage for devices 18, 19, and 20 (Table 6.2) showing the effect of interface recombination and p-n junction displacement.

carriers before they recombine at the surface, at the heterojunction, or in the bulk. As mentioned earlier, a high concentration of interface states within the junction depletion region can increase dark current and significantly reduce peak efficiency.

As a first order approximation it is often assumed that all carriers generated within one diffusion length of the p-n junction are collected by the built-in field. By applying Equations (5.5) and (5.6) to the devices having an n-type layer of doping density $4 \times 10^{17}/cm^3$ on top of a p-type substrate of doping density $2 \times 10^{17}/cm^3$ (see Figure 6.1), the minority carrier diffusion lengths can be estimated at about 7 μM for electrons and about 2 μM for holes. In other words, the effective collection width around the p-n junction in n-on-p cells is approximately 2 μM toward the front surface (in n-type material) and about 7 μM into the substrate (p-type material). For cells with the opposite polarity, but the same doping concentrations (see Figure 6.1 and devices 16 and 17 in Table 6.1), the minority carrier diffusion lengths are about 2.5 μM for holes and 6 μM for electrons, so that the effective collection region extends approximately 6 μM above the p-n junction (in p-type material) and about 2.5 μM into the substrate (n-type material). Since the effective collection region above the p-n junction is about three times greater in p-on-n cells than in n-on-p cells (for the same doping levels in each layer), it can be expected that the optimum junction placement will be deeper for the former than for the latter polarity.

However, since the doping change at the junction for either polarity is abrupt, the depletion region is highly localized and is typically about 0.1 μM wide. The region of peak generation for an abrupt

heterojunction cell is also localized to the region just beneath the heterojunction. In fact, computer calculations for abrupt AlAs-on-GaAs and GaP-on-GaAs cells indicate that over 80% of the total optical carrier generation occurs in the top 1 μM of the GaAs substrate (see Figures 2.9 and 6.3). Thus it can be expected that the optimum location of the p-n junction may be much closer to the heterojunction than indicated by the diffusion lengths of minority carriers alone.

The results of computer runs made expressly to determine the best location of the p-n junction are shown in Figures 6.4, 6.5 and 6.6. The performance parameters for the seven structures that correspond to the peaks of the curves in these figures are listed in Tables 6.1 and 6.2 as devices 7,8,9,17,20,21 and 22. Figure 6.4 shows the dependence of efficiency on p-n junction depth into the GaAs substrates below an n-type AlAs window of various thicknesses. For all three values of window thickness shown, the optimum placement of the p-n junction occurred at approximately 0.3 μM beneath the abrupt heterojunction. For more shallow placements the increase in dark current due to interface states with the depletion region caused a slight drop of about 0.3 percentage points in peak efficiency. At greater depths the collection efficiency of the junction suffered from the separation of the highly localized regions of carrier generation and built-in field.

Figure 6.5 indicates, as expected from diffusion length estimates, that the best location for the p-n junction in pAlAs-pGaAs-nGaAs cells is deeper than in similar n-on-p structures. For a 0.1 μM AlAs window and the doping levels of Figure 6.1, a peak efficiency of 21.23% was obtained by placing the junction 1.3 μM below the window (device 17)

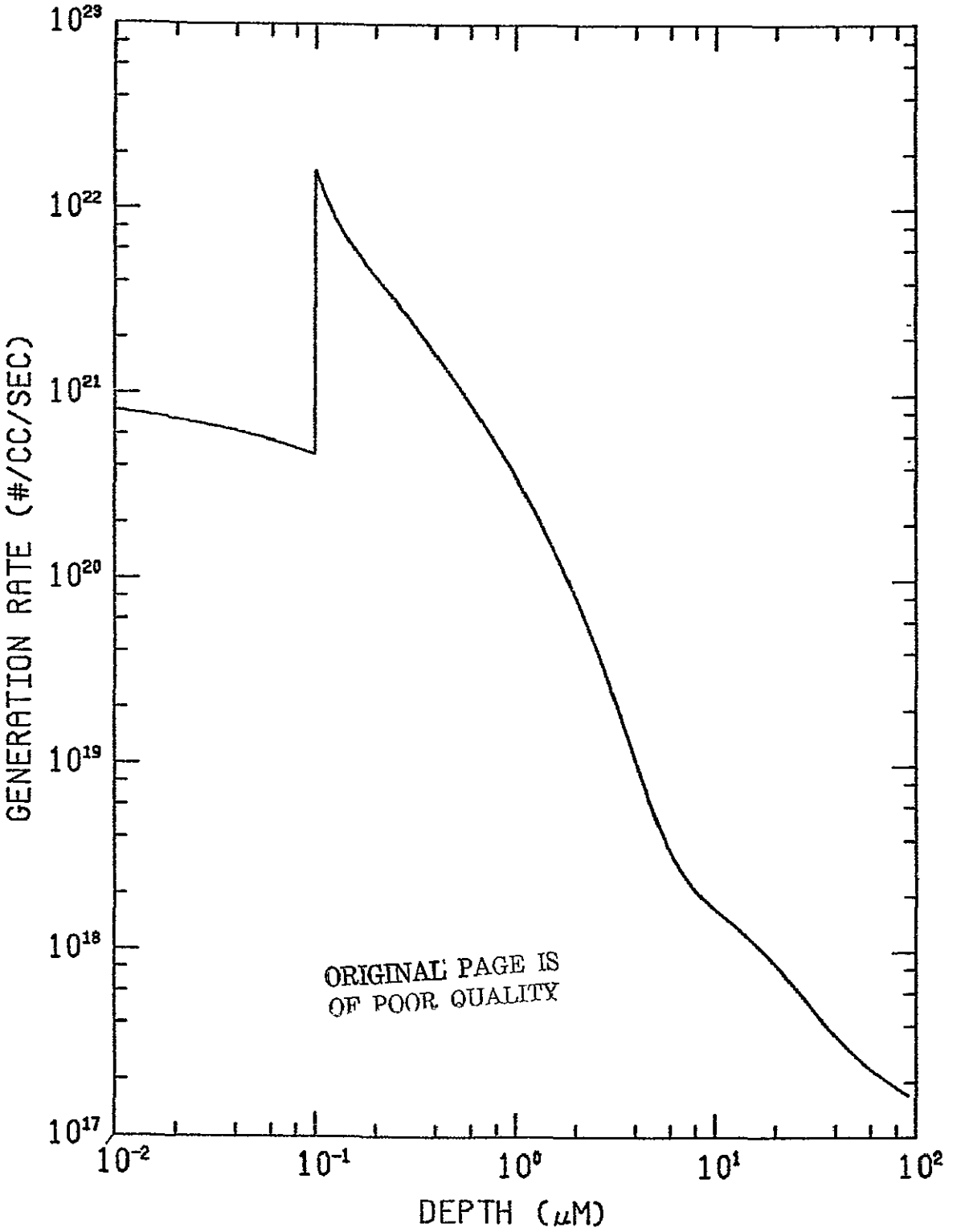

Figure 6.3 Generation rate profile for an abrupt heterojunction GaP-on-GaAs solar cell.

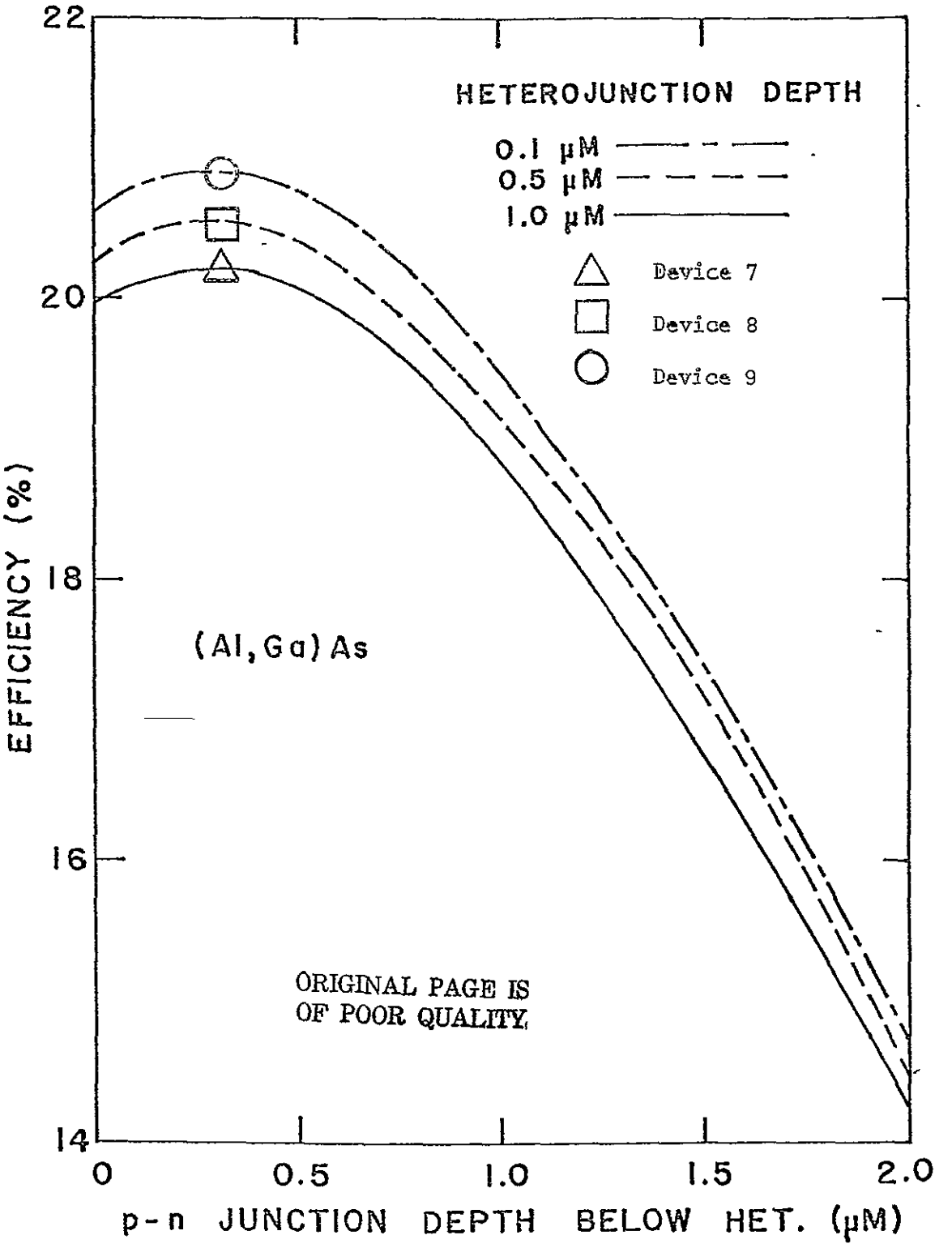

Figure 6.4 Dependence of peak efficiency on p-n junction depth below the heterojunction for abrupt nAlAs-nGaAs-pGaAs cells.

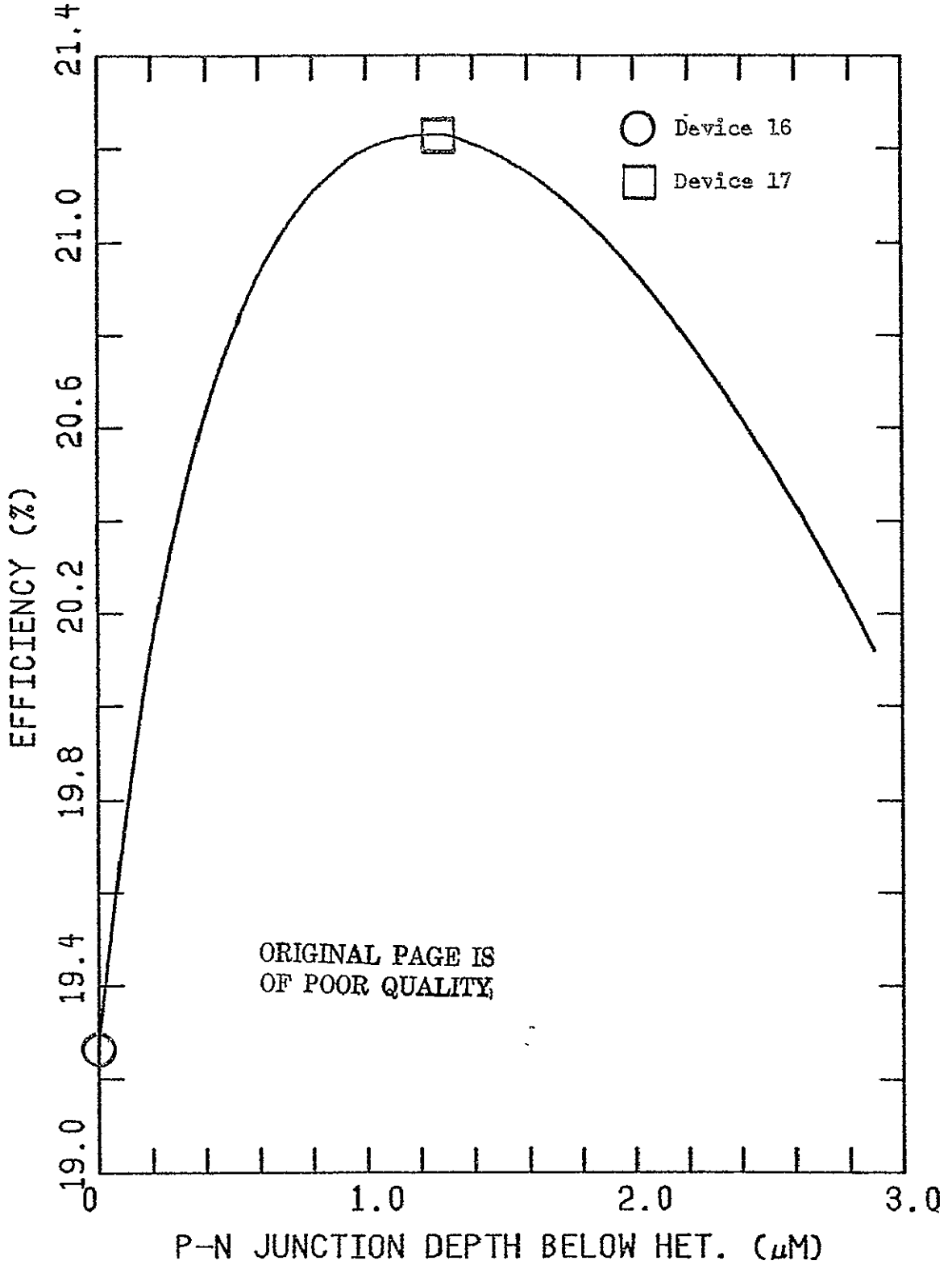

Figure 6.5 Dependence of peak efficiency on p-n junction depth below the 0.1 μM window layer for abrupt pAlAs-pGaAs-nGaAs cells.

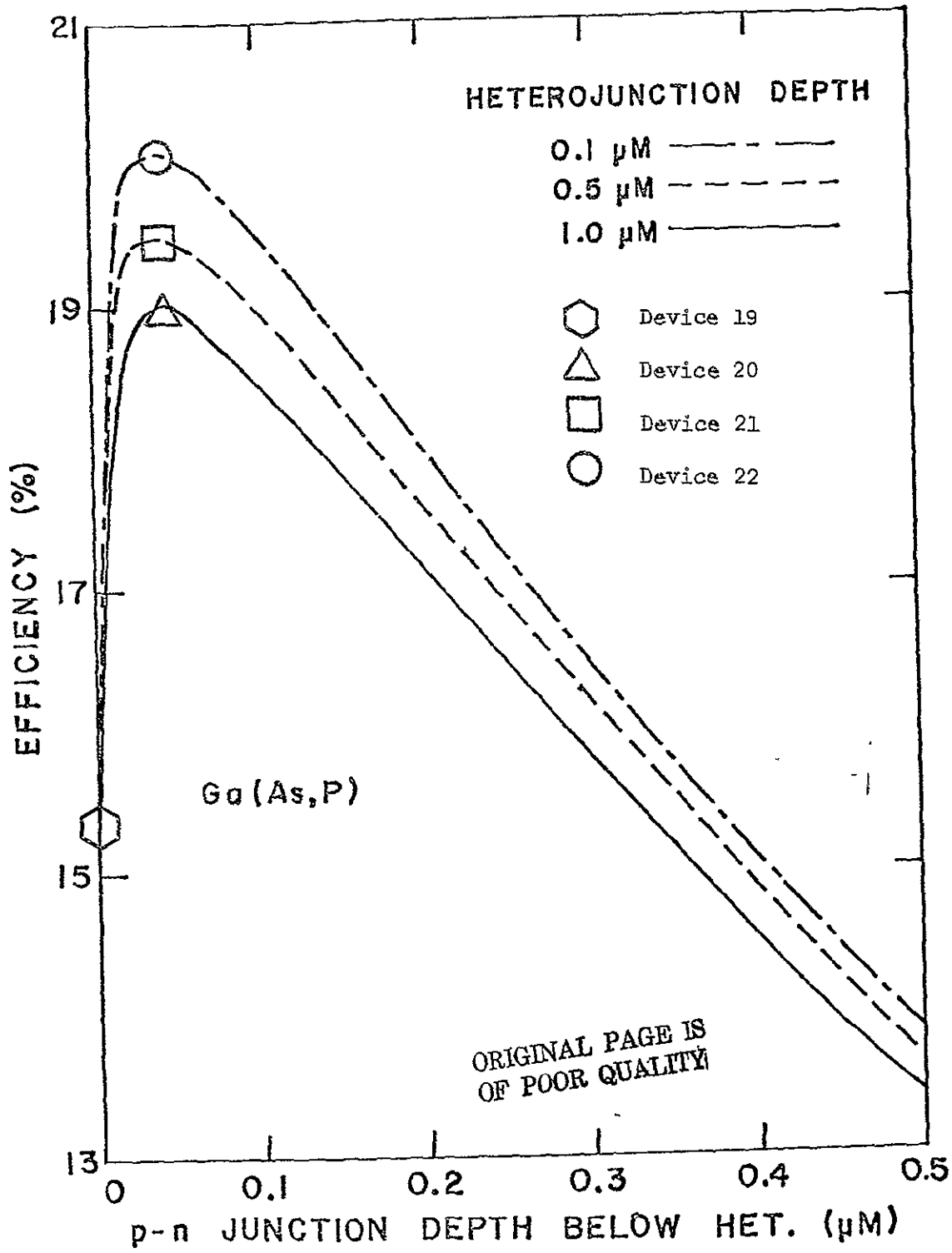

Figure 6.6 Dependence of peak efficiency on p-n junction depth below the heterojunction for abrupt nGaP-nGaAs-pGaAs cells.

compared with an efficiency of 20.95% in the corresponding n-on-p cell (device 9) with the junction optimized at a depth of 0.3 μM beneath the window. Since the open circuit voltage of device 17 is slightly greater than that of device 9 while the short circuit currents are almost equal, the higher efficiency of the p-on-n cell is due to a lower dark current rather than a higher collection efficiency. Although it appears that p-on-n solar cells may have slightly higher efficiencies than cells of the opposite polarity, the difference is so small that the choice will more likely depend on other factors such as process technology, and radiation tolerance.

The relationship found for abrupt GaP-on-GaAs n-on-p cells, shown in Figure 6.6, shows more variation than that for AlAs-on-GaAs cells. The best location for the p-n junction was found to be 0.04 μM beneath the wide bandgap window. From computer simulation data, the distance between the p-n junction and the edge of the depletion region on the n-type side was found to be close to 0.04 μM, so that maximum efficiency can be obtained by placing the heterojunction (with its high concentration of recombination centers) near the edge of the depletion region. If the p-n junction is placed closer to the window layer, peak efficiency drops rapidly until a value of only about 15% was calculated when the heterojunction and p-n junction coincide. Once again, this drop is due to an increase in dark current as shown by the dark J-V characteristics for devices 19 and 20 in Figure 6.2.

From this analysis it appears that by careful positioning of the p-n junction, GaP-on-GaAs heterojunction solar cells can be made to perform almost as efficiently as similar AlAs-on-GaAs cells in spite

of the inferior lattice match of the GaP-GaAs system. However, such accuracy naturally calls for expensive fabrication techniques. In fact, present technology would be severely strained to reproducibly make devices corresponding to the peak region of Figure 6.6. It seems more reasonable instead to investigate the possibility of controlling interface state losses by spreading the composition change over a finite distance as suggested in the next section.

6.4 Composition Grading Effects

Theoretical calculations by other workers [30,49] have indicated that built-in fields due to bandgap grading in variable composition solar cells can improve minority carrier collection efficiency by reducing the surface recombination losses. For example, Figure 6.7 shows the equilibrium band diagram for device 3 which is an n-on-p cell with a wide bandgap window, linearly graded from AlAs at the front to GaAs at the p-n junction 1 μM below the surface. According to Equation (2.8) such a composition profile should create an effective field for holes in the n-type graded layer that will sweep them away from the front surface and toward the p-n junction where they can be collected. Of course, the importance of such a process depends on the density of excess carrier generation in the window, which in turn is essentially controlled by the bandgap. For this reason, it is not immediately clear whether a constant wide bandgap window of AlAs is preferable to a graded window of $Al_xGa_{1-x}As$. In other words, it is not obvious that the built-in field is effective enough to compensate for the fact that more minority carriers are generated farther from the junction in a graded layer than in a constant wide bandgap window of AlAs.

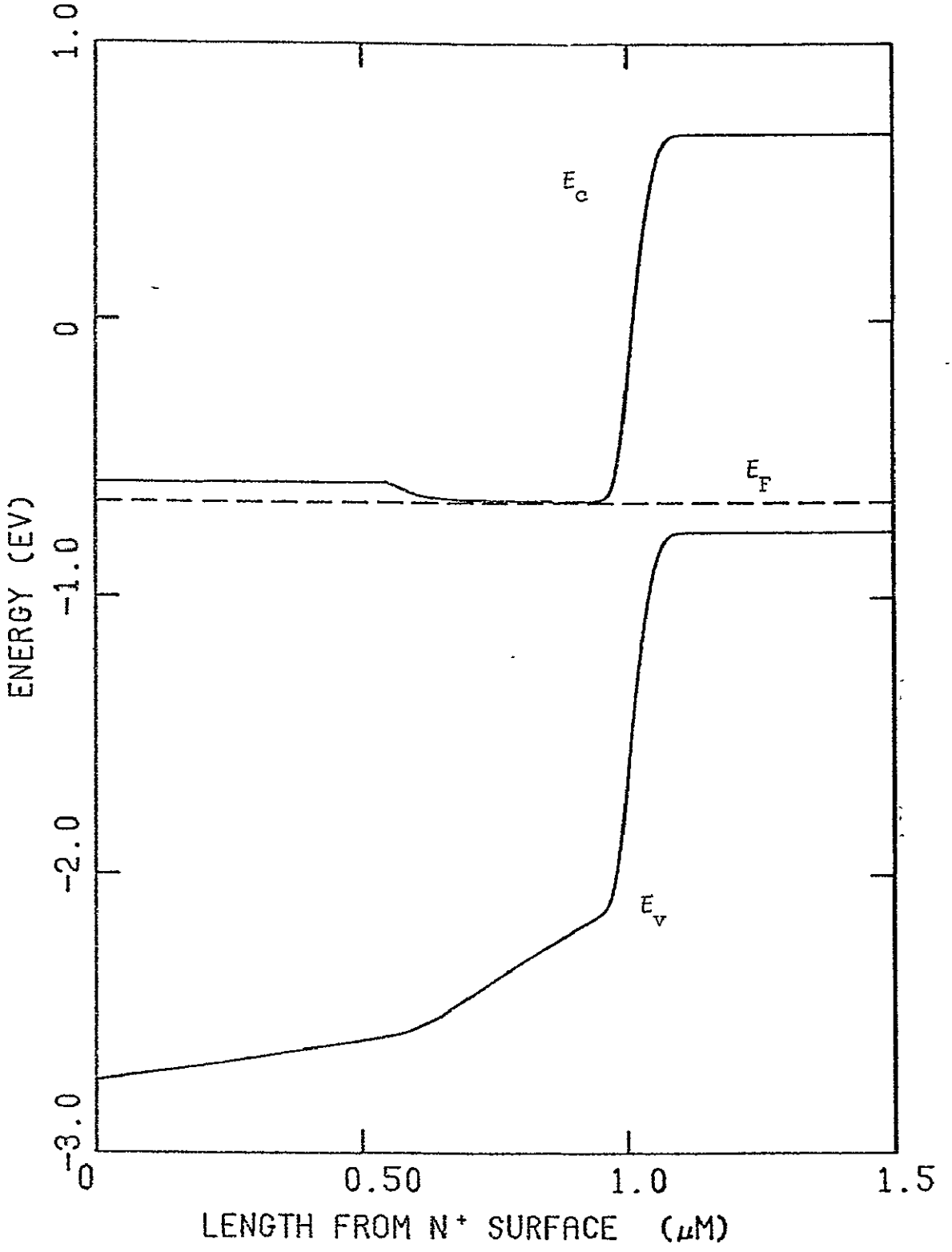

Figure 6.7 Electron energy band diagram for device 3 (Table 6.1).

By comparing devices 3 and 5, which are identical, except for the composition profile within the window, it is apparent that the gain in peak efficiency obtained by using a graded window is slightly less than 1 percentage point (20.75% vs. 19.95%). Although such an increase is not extraordinary, it is possible that significantly greater improvements can be made by examination of other, possibly nonlinear, grading profiles.

In $GaAs_{1-x}P_x$ devices, the relationship between composition grading and peak efficiency is complicated by the poor lattice match of the GaAs-GaP system. In order to determine this relationship, numerous simulations were made for n-on-p cells with the p-n junction placed at 0.14 μM beneath the surface and the window layer linearly graded over a variable width with grading terminated in GaAs at a depth of 0.1 μM (see Figure 6.1). The results of four such simulations appear in Table 6.2 for devices 26-29 and the dependence of peak efficiency on graded layer width is plotted in Figure 6.8. The initial gain in efficiency, as the graded width is increased from zero, is probably due to the widened distribution of interface states which had previously been concentrated at an abrupt heterojunction. Such a distribution increases carrier lifetime in the region of changing composition resulting in greater collection efficiency. Of course, the built-in field due to bandgap grading also improves the collection efficiency, just as it did for $Al_xGa_{1-x}As$ cells discussed earlier.

However, as the graded width is increased beyond 0.04 μM, peak efficiency falls as more carriers are generated further from the p-n junction and progressively fewer holes survive the short lifetimes

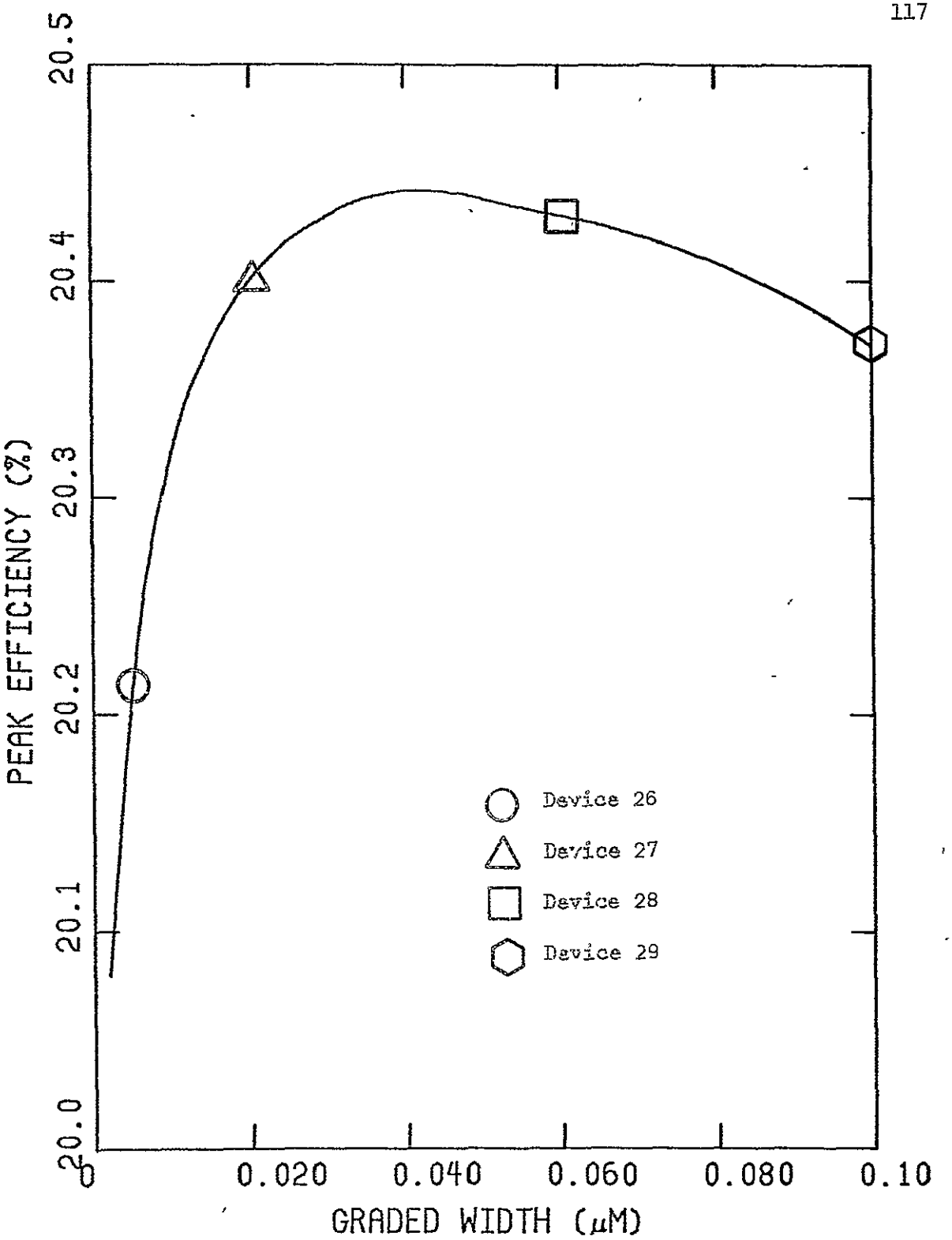

Figure 6.8 Peak efficiency vs. graded layer width in $GaAs_{1-x}P_x$ cells with 0.1μM window thickness (including graded layer). (See Figure 6.1)

that characterize the graded $GaAs_{1-x}P_x$ region. Thus, it appears that grading linearly from GaP to GaAs over about 0.04 μM can yield an improvement of about 0.4 percentage points (20.5% vs. 20.1%) in efficiency when compared with an abrupt GaP-GaAs composition profile when the p-n junction is placed at the optimum depth for an abrupt composition profile.

As discussed in the previous section, the placement of the p-n junction is very critical to the performance of $GaAs_{1-x}P_x$ solar cells. Therefore it would not be surprising to find that further gains could be obtained by optimizing the location of the p-n junction in a $GaAs_{1-x}P_x$ cell in which composition is linearly graded over about 0.04 μM. Since the graded profiles of devices 26-29 shift carrier generation slightly toward the surface, it would seem reasonable to expect the optimum p-n junction depth to be slightly closer to the surface as well. Some idea of the possible increase in efficiency associated with optimization of the p-n junction placement can be obtained from examination of Figure 6.6, which shows that a change of only 0.1 μM can result in a change of 1 percentage point in peak efficiency, even when the depletion region does not overlap the variable composition region. Once again, however, such accuracy would be difficult to achieve under the limitations of present technology.

6.5. Effect of Window Thickness on Efficiency

The use of a wide bandgap window layer affects solar cell performance in two important ways. First, it separates surface imperfections from the regions of high carrier generation rate just

beneath the window. The improved carrier collection efficiency that results from this separation is the main advantage of the window layer. Second, since no practical wide bandgap material is completely transparent to the entire solar spectrum, the absorption of some photons, essentially those toward the shorter wavelength end of the spectrum, is unavoidable. The thicker the window, the greater the absorption and the smaller the efficiency of collection of electron-hole pairs generated within the window. In other words, a trade-off exists between reduction of surface recombination losses and an increase in ordinary carrier recombination within the window layer itself.

In an effort to determine the optimum window layer thickness, several computer analysis runs were made for abrupt heterojunction AlAs-on-GaAs and GaP-on-GaAs solar cell structures. As discussed in Section 6.3, the depth of the p-n junction was varied in order to establish the best location at each of three window thicknesses: 0.1μM, 0.5μM, and 1.0μM. Figure 6.9 shows the relationship between peak efficiency and window thickness for abrupt heterojunction AlAs-on-GaAs solar cells in which the placement of the p-n junction has been optimized. This relationship is similar to that reported by Hovel and Woodall in 1973 [58] from their computer analysis of similar $Al_xGa_{1-x}As$ structures. Calculations by Hovel [54] also led to the same general conclusions. Although the computer analysis indicates that maximum efficiency occurs for window thicknesses less than 0.1μM, practical fabrication problems associated with thinner windows may outweigh any gains in efficiency that could be achieved.

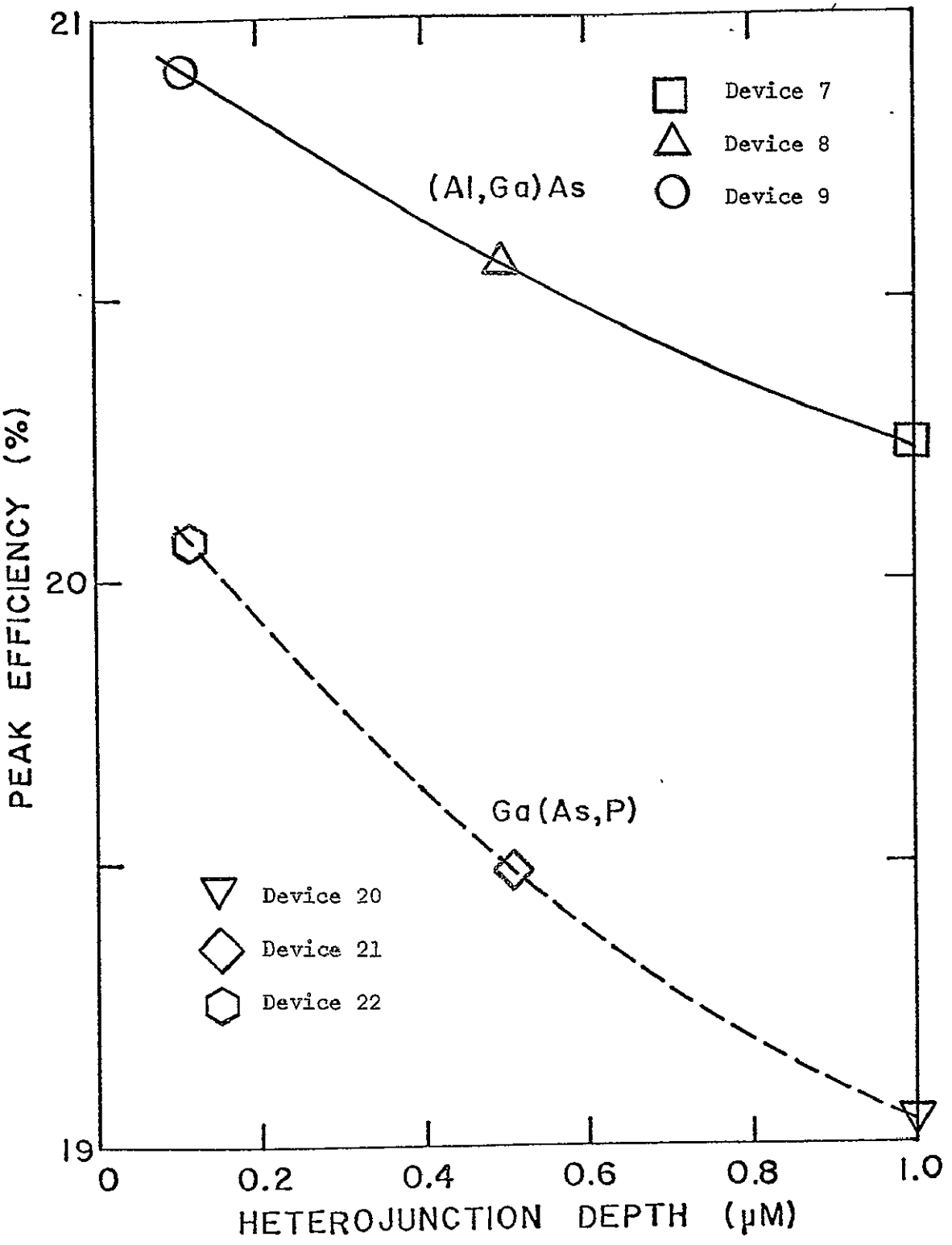

Figure 6.9 Dependence of peak efficiency on heterojunction depth for abrupt AlAs-GaAs and GaP-GaAs solar cells, with optimum placement of the p-n junction.

Because of the presence of surface states, as modeled by the surface recombination velocity S, peak efficiency can be expected to fall as the window thickness approaches zero. Since the surface recombination velocity of 10^5cm/sec specified for these computer simulations corresponds to relatively high quality surface characteristics, the results might appear to be somewhat optimistic. In order to test the effect of a higher surface recombination velocity, a computer analysis was made for both alloy systems specifying a value of 10^6cm/sec for S while using the same thin window structure used in devices 9 and 22. The results shown in Tables 6.1 and 6.2 as devices 10 and 23, indicate that such a ten-fold increase in S should reduce the peak efficiency of an AlAs-GaAs cell from 20.91% to 20.86%, and reduce the peak efficiency of a GaP-GaAs cell from 20.10% to 19.56%. These small reductions are due to a reduced carrier collection efficiency leading to slightly lower values of short circuit current. However, it is apparent that even a very thin window layer (0.1μM) effectively eliminates surface recombination as a dominant loss mechanism for reasonable values of S.

6.6 Bulk Bandgap Optimization

Although it is well known that the optical properties of GaAs are better suited to solar energy conversion than those of silicon [4,21, 23,54] (see Figure 6.10) it is not clear that GaAs is the best material available, especially when the full range of electrical and optical characteristics are examined in a complete solar cell structure under AM0 conditions. Specifically, the bandgap (1.44eV) of a GaAs substrate may be too small or too large to produce the highest peak efficiency.

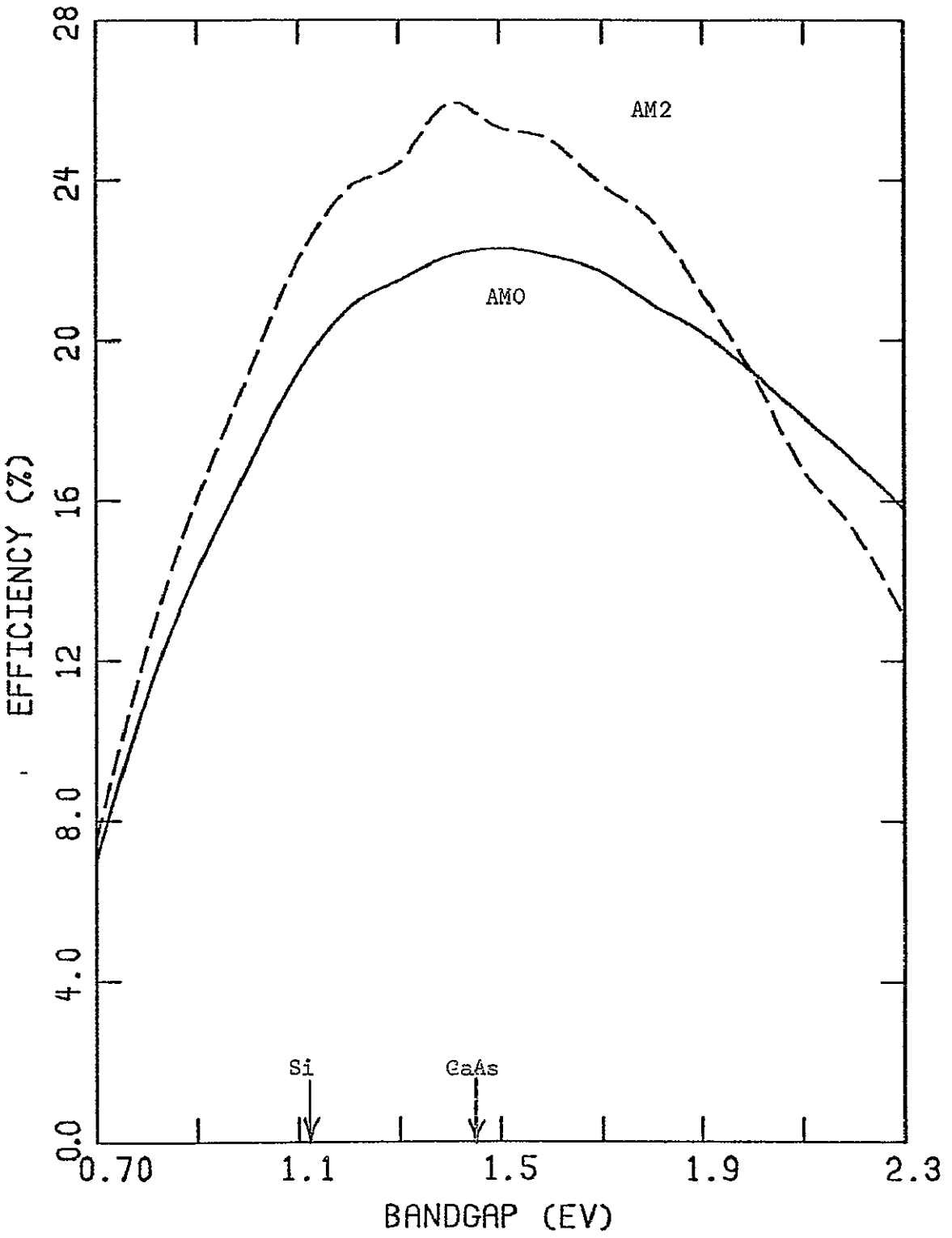

Figure 6.10 Dependence of conversion efficiency limit on bandgap for AMO and AM2 irradiance conditions [54].

In general, the wider the substrate bandgap, the higher the open circuit voltage and the smaller the dark current. But as the bandgap is widened, the substrate is made more transparent to a larger share of the solar spectrum so that fewer carriers are generated toward the front of the cell near the p-n junction, resulting in a lower short circuit current. In other words, adjustment of the substrate bandgap involves a trade-off between open circuit voltage and short circuit current.

The computer simulation of devices 9 and 11-15 in Table 6.1 and devices 22, 24 and 25 in Table 6.2 were made to determine the effect on efficiency of adjusting the composition of the substrate in abrupt heterojunction $(Al,In)_xGa_{1-x}As$ and $GaAs_{1-x}P_x$ solar cells. In cells 11 and 12, a 0.1 μM AlAs window covers an $Al_xGa_{1-x}As$ substrate of uniform composition having a larger bandgap than GaAs. A 0.1 μM AlAs window is also used in devices 13-15, but the substrate consists of $In_xGa_{1-x}As$ which has a smaller bandgap than GaAs. The peak efficiencies for these cells are plotted as the solid curve in Figure 6.11. It is seen that a GaAs substrate is superior to one made of either $Al_xGa_{1-x}As$ or $In_xGa_{1-x}As$. However, the inferiority of $In_xGa_{1-x}As$ is due to the severe lattice mismatch (about 7%) between InAs and GaAs rather than the reduction in bandgap. When the lattice constant of InAs was assigned a value equal to that of AlAs, the computer analysis predicted the performance indicated by the dashed curve segment in Figure 6.11, which peaks at a bandgap of about 1.41 eV. In other words, a substrate of $In_{.02}Ga_{.98}As$ would perform slightly better than a GaAs substrate if it were not for the poor lattice match. However, it should be noted that the p-n junction placement was optimized only for the structure of

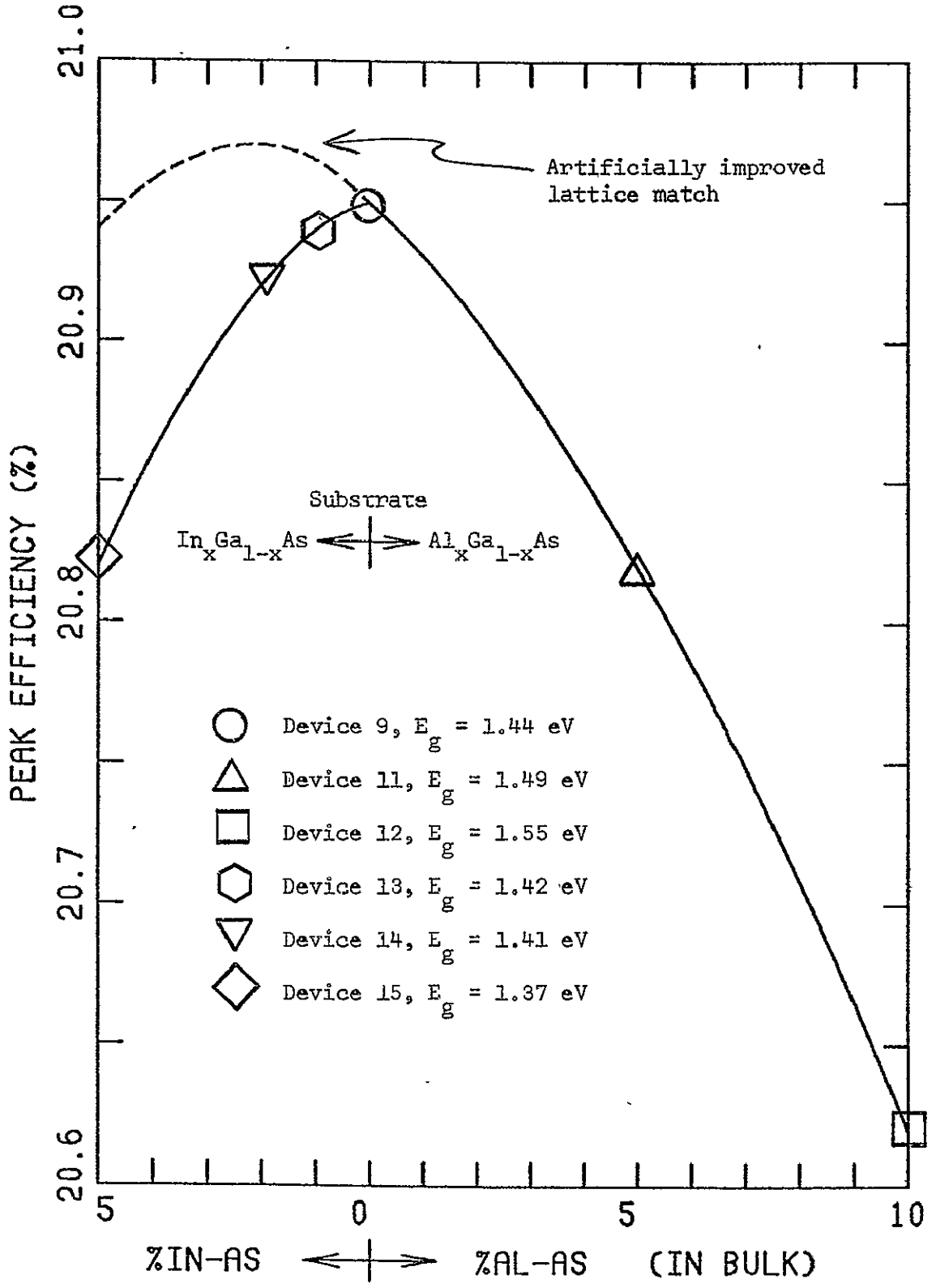

Figure 6.11 Peak efficiency vs. substrate composition in abrupt heterojunction AlAs-on-$Al_xGa_{1-x}As$ and AlAs-on-$In_xGa_{1-x}As$ cells with an 0.1μM window and a p-n junction depth of 0.4μM.

device 9 by varying the junction depth while holding other structure specifications constant. At the present time, this procedure has not been done for any structure having a percentage of AlAs or InAs in the substrate. More specifically, because the introduction of AlAs into the substrate widens the bandgap and therefore reduces the absorption coefficient for photons near the band edge, it should be expected that the best p-n junction placement should be somewhat deeper for (Al,Ga)As substrates than for a GaAs substrate. Conversely, an (In,Ga)As substrate probably calls for a shallower p-n junction. Since the generation rate distribution is very sensitive to material bandgap changes and the optimum p-n junction location in turn depends on the generation rate distribution, the trend shown in Figure 6.11 does not prove that further small gains in efficiency cannot be obtained by alloying a GaAs substrate with a small percentage of AlAs, or more likely, InAs. In any case, the potential improvement is so small that these computer simulations essentially reinforce earlier estimates that the bandgap of GaAs is near optimum for AMO conditions [54].

Similar results were obtained from the simulation of cells having GaP alloyed with GaAs in the substrate beneath a 0.1 μM GaP window. The data for devices 22, 24 and 25 indicate that when the placement of the p-n junction is optimized for an abrupt GaP-on-GaAs cell (device 22) the subsequent introduction of 5% GaP (increasing the bandgap from 1.44 eV to 1.48 eV) in the substrate reduces peak efficiency from 20.10% to 19.39%. When the GaP level is increased to 10% (E_g = 1.54 eV), the peak efficiency falls to 18.91%. Although this trend, shown in Figure 6.12, does not encourage the use of a substrate

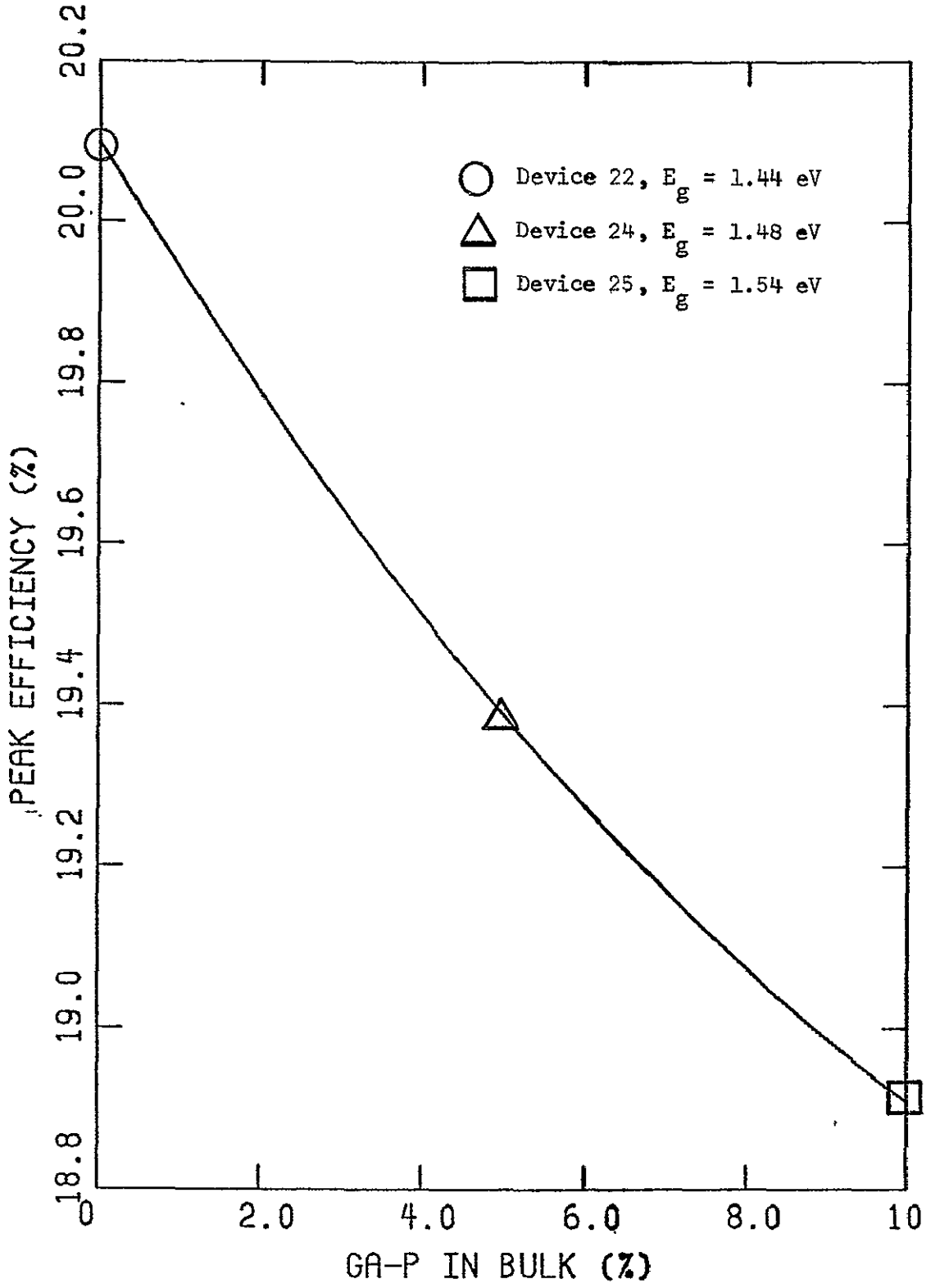

Figure 6.12 Dependence of peak efficiency on substrate composition in abrupt heterojunction GaP-$GaAs_{1-x}P_x$ cells with heterojunction depth of 0.1μM and p-n junction depth of 0.14μM.

with a bandgap wider than GaAs, it must again be remembered that the p-n junction in devices 24 and 25 may not be placed deep enough for maximum efficiency. The stronger dependence found for Ga(As,P) substrates compared with (Al,Ga)As substrates may be due to the stronger relationship between p-n junction depth and efficiency found for the GaAsP system in Section 6.3 (compare Figures 6.4 and 6.6).

If the performance of (Al,Ga)As, (In,Ga)As or Ga(As,P) substrates without optimum p-n junction placement had been found clearly superior to optimized devices with GaAs substrates, the analysis predictions for alloy substrates would have been favorable. However, in view of the results that were obtained, there seems little room for improvement of the GaAs substrate by alloying it with other materials to adjust the bandgap.

6.7 Interpretation of Analysis Results

It is important to view the preceding analysis results with consideration given to the techniques that produced them and the fabrication technology that is currently available to create the structures they call for. First of all, some of the material parameters, in particular excess carrier lifetimes, represent the characteristics of relatively high quality material. Analyses using such values may lead to slightly lower dark currents, and thus slightly higher open circuit voltages, fill factors and efficiencies than have been reported in experimental studies. Secondly, in comparing computer predictions with experimental data, it should be noted that most practical variable composition cells tested up to the present time have used less than 100%

AlAs or GaP at the surface. However, because early computer simulation data indicated that 100% AlAs or GaP at the front produced the highest efficiencies, most of the structures reported in this work specify such surface compositions. It is believed that the technical problems that discourage the use of AlAs and GaP as surface materials will soon be overcome.

The difficulty of obtaining very thin window layers (less than 0.1μM) may discourage the implementation of the optimum structures indicated in Section 6.5. However, the basic purpose of computer simulation is to permit reasonable estimation of the potential benefits of various solar cell structures so that costs can be weighed against these benefits.

Finally, sheet resistance effects, which depend on contact geometry and are not incorporated into the analysis program, may become significant when the p-n junction is placed near the surface. The performance parameters reported in this work are for a one dimensional cell uncorrected for contact coverage and surface layer sheet resistance losses because all current has been assumed to be perpendicular to the front surface. In order to avoid the prohibitive optical losses associated with continuous contact coverage, practical cells generally use finger contact geometry which requires some lateral current flow near the surface.

Although computer methods to correct simulation results for contact geometry are available [19], they were not considered necessary to the present research because the basic aim was to assess the relative influence of structure and material parameters on efficiency. Practical

contact areas typically account for a 5-10% reduction in short circuit current and efficiency while sheet resistance may reduce efficiency by about 0.5 percentage points. In other words, for a complete solar cell, the efficiency values reported in earlier sections must be reduced by about 1.5 percentage points so that a 20% cell should be considered an 18.5% cell after contacts have been included in the estimate.

7. SUMMARY AND RECOMMENDATIONS FOR FURTHER RESEARCH

7.1 Summary

The aim of the present research was to develop a computer program capable of analyzing heterojunction and graded composition solar cells and to apply that program to a number of proposed cell structures using feasible semiconductor materials. The program, now complete, accepts a wide variety of device structures and, by numerically solving a set of differential equations, is capable of simulating the behavior of solar cells made of a ternary alloy between two binary semiconductors. Up to the present time, the program has been used to analyze variable composition solar cells made of $Al_xGa_{1-x}As$, $In_xGa_{1-x}As$ and $GaAs_{1-x}P_x$. The highest efficiencies calculated for $Al_xGa_{1-x}As$ devices were 21.23% for a pAlAs-pGaAs-nGaAs cell(device 17 in Table 6.1) and 20.95% for an nAlAs-nGaAs-pGaAs cell (device 9 in Table 6.1). When the values for peak efficiency obtained from these computer simulations are adjusted for contact geometry losses (typically a reduction of about 1.5 percentage points) they are in good agreement with earlier less exact calculations [30,49,54,58]. These calculated efficiencies are somewhat higher than some values reported for experimental variable composition cells such as the 14.7% devices built by Hovel and Woodall in 1973 [12]. This is not unexpected because the material parameters used in the present computer studies characterize relatively high quality semiconductor material rather than the typical properties of most contemporary experimental cells. Also, the computer simulations reported in this work generally specified 100% AlAs or GaP at the surface,

while most experimental cells presently retain some percentage of GaAs throughout. These calculations have been intended to determine the potential performance levels of $Al_xGa_{1-x}As$, $In_xGa_{1-x}As$ and $GaAs_{1-x}P_x$ solar cells rather than explain individual experimental test results. However, the latest results available at the time of this writing include a report of an $Al_xGa_{1-x}As$ cell with a measured AMO efficiency of 18.5% including contact losses [61], which is less than a percentage point below the best efficiencies calculated for such devices in the present work.

Several relationships between device structure and performance have been indicated by the analyses made up to the present time. The effect of heterojunction interface states was examined by comparison of computer simulations with and without interface recombination. The resulting losses at abrupt AlAs-GaAs interfaces were minor. However, as expected from the severe lattice mismatch, the peak efficiency of GaP-GaAs heterojunction cells suffered far more from interface recombinations which reduced efficiency as much as 5 percentage points when the p-n junction coincided with the heterojunction. Subsequent computer simulations indicated that these losses could be largely offset by moving the p-n junction deeper so that the GaP-GaAs interface no longer occurred at the center of the depletion region. A further increase in efficiency of about 0.5 percentage points for $GaAs_{1-x}P_x$ cells was obtained by linearly grading the change from GaP to GaAs over a distance of about 0.04μM. Grading over greater widths led to significant recombination losses within the window layer. Similar, but far less pronounced effects were observed in $Al_xGa_{1-x}As$ simulations. It was

found that p-on-n $Al_xGa_{1-x}As$ cells had smaller dark currents than similar n-on-p devices, allowing them to achieve slightly higher efficiencies and open circuit voltages.

The success of wide bandgap window layers in reducing surface recombination losses was corroborated by computer simulation of devices that differed only in surface recombination velocity. An increase in S from 10^5cm/sec to 10^6cm/sec reduced the peak efficiency of AlAs-GaAs cells by less than 0.1 percentage points and that of GaP-GaAs cells by less than 0.6 percentage points. Since these results were obtained for window layers 0.1μM thick, it is apparent that even very thin windows can virtually eliminate surface recombination as a dominant performance factor.

Finally, computer simulation of devices having $Al_xGa_{1-x}As$, $In_xGa_{1-x}As$ and $GaAs_{1-x}P_x$ ($0<x\leq 0.1$) substrates indicated that significant gains in performance could not be expected from use of substrates with wider or smaller bandgaps than GaAs. However, since the placement of the p-n junction was not optimized for such structures, it would not be inconsistent with these calculations to find that small increases in peak efficiency could be obtained by careful positioning of the p-n junction, especially in the case of $Al_xGa_{1-x}As$ and $In_xGa_{1-x}As$ substrates. In addition, the complex dependence of efficiency on substrate properties means that the use of materials other than GaAs cannot be ruled out simply on the basis of computer simulation of these alloy systems.

The computer analysis program has given reasonable results for both abrupt and graded composition structures, and has been useful in estimating the potential advantages of various configurations.

The detailed data which the program produces has been helpful in assessing the relative importance of the numerous interacting phenomena that control solar cell performance.

7.2 Recommendations for Further Research

Although the computer analysis program is now essentially complete, its full potential has not yet been utilized. Its capabilities permit the examination of several design options which have not been considered in the present work. Among the options which would require virtually no modification of the program are:

1) Use of a Gaussian (or other) doping profile

2) Comparison of different doping levels

3) Further examination of p-on-n solar cells

4) Optimization of p-n junction placement for all devices analyzed

5) Application of irradiance conditions other than AM0, in particular AM2 conditions for terrestrial applications

6) Use of antireflection layers other than SiO (for example TiO_x)

7) Consideration of nonlinear composition grading to optimize the generation rate profile for improved collection efficiency

8) Analysis of devices made of other alloys such as $GaAs_{1-x}Sb_x$

9) Determine the effects of lifetimes shorter than those examined in this work, i.e. consider use of lower quality, cheaper material.

The study of several other possibilities would require some minor program modifications, but could yield useful results. Among these are:

10) Improved lifetime modeling, to relate lifetime directly to doping levels and mobilities

11) Design of a numerical step distribution within the analysis program that would relate positional step size solely to the slope of the three independent variables ψ, ϕ_n, and ϕ_p. (see Section 3.4, and References 13 and 19)

12) Performance under multi-sun and high temperature conditions such as those found in concentrator solar cell systems.

Of course, the input data concerning material parameters should continually be updated to maintain consistency with the latest available experimental figures. Finally, it is hoped that these computer studies will be followed by attempts to achieve the predicted performance levels in actual working devices. After all, computer simulation is intended to provide guidance for experimental research.

8. LIST OF REFERENCES

1. "Energy Report," IEEE Spectrum, 13, October 1976, p. 10.

2. Y. M. Yim, "Direct and Indirect Optical Energy Gaps of AlAs," Journal Applied Physics, 42, 1971, p. 2854.

3. J. Tauc, "Generation of an emf in semiconductors with nonequilibrium current carrier concentration," Review of Modern Physics, 29, 1957, p. 308.

4. M. Wolf, "Limitations and Possibilities for Improvement of Photovoltaic Solar Energy Converters, Part I: Considerations for Earth's Surface Operation," Proceeding of the IRE, 48, 1960, p. 1246.

5. P. M. Emtage, "Electrical donduction and the photovoltaic effect in semiconductors with position dependent bandgaps," Journal of Applied Physics, 33, 1962, p. 1950.

6. NASA, "Solar Electromagnetic Radiation," NASA Document NASA SP 8005.

7. M. L. Cohen and T. K. Bergstresser, "Band Structures and Pseudopotential Form Factors for Fourteen Semiconductors of the Diamond and Zincblend Structures," Physical Review, 141, 1966, p. 789.

8. A. G. Thompson and J. C. Woolley, "Energy-Gap Variation in Mixed III-V Alloys," Canadian Journal of Physics, 45, 1967, p. 255.

9. H. Kroemer, Proceedings of the IEEE, 51, 1963, p. 1782.

10. Y. Marfaing and J. Chevallier, "Photovoltaic Effects in Graded Bandgap Structures," IEEE Transactions on Electron Devices, ED-18, 1971, p. 465.

11. J. F. Womac and R. H. Rediker, "The graded-gap $Al_xGa_{1-x}As$-GaAs heterojunction," Journal of Applied Physics, 43, 1972, p. 4129.

12. H. J. Hovel and J. M. Woodall, "$Ga_{1-x}Al_xAs$-GaAs P-P-N Heterojunction Solar Cells," Journal of the Electrochemical Society, 120, 1973, p. 1246.

13. E. D. Graham and J. R. Hauser, "Computer Techniques for Accurate Solid State Device Analysis," Annual report on NSF Grant GK-13752, April 1970.

14. R. E. Bellman, "Functional equations in the theory of dynamic programming V: positivity and quasilinearity," Proceedings of the National Academy of Sciences of the United States of America, 41, 1955, p.743.

15. R. Kalaba, "On nonlinear differential equations, the maximum operation and monotone convergence," Journal of Mathematics and Mechanics, 8, 1959, p. 519.

16. R. E. Bellman and R. E. Kalaba, Quasilinearization and Nonlinear Boundary Value Problems; American Elsevier Publishing Co., Inc., New York, N. Y., 1965.

17. A. DeMari, "Accurate Numerical Steady-State and Transient One-Dimensional Solutions of Semiconductor Devices," unpublished Ph.D. Thesis, California Institute of Technology, 1967.

18. E. S. Lee, Quasilinearization and Invariant Imbedding, Academic Press, New York, N. Y., 1968.

19. P. M. Dunbar and J. R. Hauser, "A Theoretical Analysis of the Current-Voltage Characteristics of Solar Cells," annual report on NASA Grant NGR 34-002-195, August 1975.

20. M. B. Prince, "Silicon Solar Energy Converters," Journal of Applied Physics, 26, 1955, p. 534.

21. J. J. Loferski, "Theoretical considerations governing the choice of the optimum semiconductor for photovoltaic energy conversion," Journal of Applied Physics, 27, 1956, p. 777.

22. S. C. Tsaur, A. G. Milnes, R. Sahai, and D. L. Feucht, "Theoretical and experimental results for GaAs solar cells," Proceedings of the Fourth International Symposium on GaAs and Related Compounds, Conference Series No. 17, The Institute of Physics, London, England, 1972, p. 156.

23. J. J. Wysocki, and P. Rappaport, "Effect of Temperature on Photovoltaic Solar Energy Conversion," Journal of Applied Physics, 31, 1960, p. 571.

24. J. W. Harrison and J. R. Hauser, "Theoretical Calculations of Electron Mobility in Ternary III-V Compounds," Journal of Applied Physics, 47, 1976, p. 292.

25. E. M. Conwell, High Field Transport in Semiconductors, Academic Press, New York, N. Y., 1967.

26. R. Tsu, L. L. Chaing, G. A. Sai-Halasz, and L. Esaki, "Effect of Quantum States on a Photocurrent in a Superlattice," Physical Review Letters, 34, 1975, p. 1509.

27. D. B. Holt, "Misfit Dislocations in Semiconductors," Journal of Physics and Chemistry of Solids, 27, 1966, p. 1053.

28. M. Ettenberg and H. Kressel, "Interfacial recombination at (AlGa)As/GaAs heterojunction structures," Journal of Applied Physics, 47, 1976, p. 1538.

29. A. G. Milnes and D. L. Feucht, "Heterojunctions and Metal-Semiconductor Junctions, Academic Press, New York, N.Y., 1972.

30. J. A. Hutchby and R. L. Fudurich, "Theoretical analysis of $Al_xGa_{1-x}As$-GaAs graded bandgap solar cells," Journal of Applied Physics, 47, 1976, p. 3140.

31. M. Konagai and K. Takahashi, "Graded-bandgap $pGa_{1-x}Al_xAs$-nGaAs heterojunction solar cells," Journal of Applied Physics, 46, 1975, p. 3542.

32. J. Vilms and W. E. Spicer, "Quantum Efficiency and Radiative Lifetime in p-type Gallium Arsenide," Journal of Applied Physics, 36, 1964, p. 2815.

33. M. Ettenberg and C. J. Neuse, "Comparison of Zn-doped GaAs layers prepared by liquid-phase and vapor-phase techniques, including diffusion lengths and photoluminescence," Journal of Applied Physics, 46, 1975, p. 3500.

34. G. A. Acket, W. Nijman and H. 't Lam, "Electron lifetime and diffusion constant in germanium doped gallium arsenide," Journal of Applied Physics, 45, 1974, p. 3033.

35. M. Neuberger, Handbook of Electronic Materials, Vol. 2, III-V Semiconducting Compounds, IFI/Plenum Press, New York, N.Y., 1971.

36. D. L. Rode, "How much Al in the AlGaAs-GaAs Laser?" Journal of Applied Physics, 45, 1974, p. 3887.

37. J. W. Harrison, "Gallium Arsenide Technology," Vol. I, Research Triangle Institute, Technical Report AFAL-TR72-312, Vol. I, January 1973.

38. Obtained from a Monte Carlo calculation by J. R. Hauser.

39. M. R. Lorenz, R. Chicotka, G. D. Pettit, and P. J. Dean, "The fundamental absorption edge of AlAs and AlP," Solid State Communications, 8 1970, p. 693.

40. A. Onton, Extended Abstracts, International Conference of Semiconductors, 10th Cambridge, August 1970, (unpublished).

41. A. Onton, M. R. Lorenz, and J. M. Woodall, Bulletin of the American Physics Society, 16, 1971, p. 371.

42. A. A. Immorlica, Jr., and G. L. Pearson, "Velocity saturation in n-type $Al_xGa_{1-x}As$ single crystals," Applied Physics Letters, 25, 1974, p. 570.

43. S. Kocsis, "Lattice Scattering Mobility of Electrons in GaP," Physica Status Solidi A., 28, 1975, p. 133.

44. W. P. Dumke, M. R. Lorenz, and G. D. Pettit, "Enhanced Indirect Optical Absorption in AlAs and GaP," Physical Review B, 5, 1971, p. 2978.

45. K. Fletcher and P. N. Butcher, "Solution of the Boltzmann Equation in Ellipsoidal Valleys with Application to the <100> Valleys of GaAs and GaP," Journal of Physics C, 6, 1973, p. 976.

46. D. M. Roessler and Tao-Yuan Wu, "New observations on near band edge luminescence in gallium arsenide phosphide ($GaAs_{1-x}P_x$)," Applied Physics Letters, 25, 1974, p. 718.

47. M. G. Craford, R. W. Shaw, A. H. Herzog, and W. D. Groves, "Radiative recombination mechanisms in GaAsP diodes with and without nitrogen doping," Journal of Applied Physics, 43, 1972, p. 4075.

48. J. D. Wiley and M. DiDominico, Jr., "Lattice Mobility of Holes in III-V Compounds," Physical Review B, 2, 1970, p. 427.

49. J. A. Hutchby, "High Efficiency Graded Band Gap $Al_xGa_{1-x}As$-GaAs Solar Cell," Applied Physics Letters, 26, 1975, p. 457.

50. P. Moon, "Solar Radiation Curves," Journal of the Franklin Institute, 230, 1940, p. 583.

51. H. C. Casey, Jr., D. D. Sell and K. W. Wecht, "Concentration Dependence of the Absorption Coefficient for n- and p-type GaAs between 1.3 and 1.6 eV," Journal of Applied Physics, 46, 1975, p. 250.

52. B. O. Seraphin and H. E. Bennett, "Optical Constants-Gallium Phosphide," Semiconductors and Semimetals, N. Y. Academic Press, 3, 1966, p. 509.

53. M. R. Lorenz, G. D. Pettit, and R. C. Taylor, "Band Gap of Gallium Phosphide from 0° to 900°K and Light Emission from Diodes at High Temperatures," Physical Review, 171, 1968, p. 878.

54. H. J. Hovel, Semiconductors and Semimetals, Vol. 11: Solar Cells, Academic Press, N. Y., 1975.

55. R. L. Anderson, "Experiments on Ge-GaAs Heterojunctions," Solid State Electronics, 5, 1962, p. 341.

56. S. S. Perlman and D. L. Feucht, "p-n Heterojunctions," Solid State Electronics, 7, 1964, p. 911.

57. D. A. Jenny, J. J. Loferski, and P. Rappaport, "Photovoltaic Effect in GaAs p-n Junctions and Solar Energy Conversion," Physical Review, 101, 1956, p. 1208.

58. H. J. Hovel and J. M. Woodall, "Theoretical and experimental evaluations of $Ga_{1-x}Al_xAs$-GaAs solar cells," Conference Record, Tenth IEEE Photovoltaic Specialists Conference, November, 1973, p. 25.

59. J. DuBow, "From photons to kilowatts: Can solar energy deliver?," Electronics, November 11, 1976, p. 86.

60. L. Curran, "Companies look for ways to improve solar cell output," Electronics, November 11, 1976, p. 90.

61. G. H. Walker, E. J. Conway, and C. E. Buvik, "High Efficiency GaAs Solar Cells," paper presented at the High Efficiency and Radiation Damage Silicon Solar Cell Meeting at the NASA-Lewis Research Center, April 27-29, 1977.